Experimental Investigation and Computational Modelling of the Thermoforming Process of Thermoplastic Starch

by
Damian Szegda

A thesis submitted for the degree of Doctor of Philosophy

The School of Engineering and Design, Brunel University

January, 2009

Abstract

Plastic packaging waste currently forms a significant part of municipal solid waste and as such is causing increasing environmental concerns. Such packaging is largely non-biodegradable and is particularly difficult to recycle or to reuse due largely to its complex compositions. Apart from limited recycling of some easily identifiable packaging wastes that can be separated economically, such as bottles, most packaging waste ends up in landfill sites. In recent years, in an attempt to address this problem in plastic packaging, the development of packaging materials from renewable plant resources has received increasing attention and a wide range of bioplastic materials based on starch are now available. Environmentally these bioplastic materials also reduce reliance on oil resources and have the advantage that they are biodegradable and can be composted upon disposal to reduce the environmental impact.

Many food packaging containers are produced by thermoforming processes in which thin sheets are inflated under pressure into moulds to produce the required thin -wall structures. Hitherto these thin sheets have almost exclusively been made of oil-based polymers and it is for these that computational models of thermoforming processes have been developed. Recently, in the context of bioplastics, commercial thermoplastic starch sheet materials have been developed. The behaviour of such materials is influenced both by temperature and, because of the inherent hydrophilic characteristics of the materials, by moisture content. Both of these aspects affect the behaviour of bioplastic sheets during the thermoforming process.

This thesis describes experimental work and work on the computational modelling of thermoforming processes for thermoplastic starch sheets using a commercially available material. The experimental work has been carried in order to characterise the deformation behaviour of the material with regard to different temperature, moisture contents and strain rates. Thermoforming of the material was performed and samples produced were used for comparison and verification of the computational modelling of the thermoforming process.

In the first attempt to model the thermoforming process, a hyperelastic constitutive equation was established to approximate the material behaviour taking account of the combined effects of temperature and moisture content and a simple

membrane model with constrained deformation was used to model an axisymmetric case of thermoforming. Simulations with this model showed that moisture content mostly affects the pressure required to push the sheet into the mould while moisture variation during thermoforming has little effect on the final thickness distribution of the product. Considerable discrepancies were found in the thickness distribution between the predictions from the model and the experimental measurements.

Further attempts were made to take account of the elasto-plastic behaviour of the material and a more complex three-dimensional FE model was developed using ANSYS/LS-DYNA. Based on the findings in the simpler modelling work, no attempt was made to incorporate the moisture content effect on material behaviour but the material parameters for the elasto-plastic constitutive equation were obtained from high speed tensile tests so that moisture variation during thermoforming could be minimised and neglected. The predictions from this model have led to significant improvements in prediction of the thickness distribution which has become much closer to the experimental measurements in comparison with the hyperelastic model.

This work provides some important insights into thermoforming of thermoplastic starch materials: a) Deformation behaviour of such materials depends strongly on the moisture content and the temperature, both of which affect behaviour during thermoforming processes, including the preheating stage; b) moisture variation during the thermoforming process has a significant effect on the pressure required for the deformation. This also leads to variation of moisture content distribution in the final product, which in turn affects the material properties such as ductility or impact strength at different positions in the thermoformed structure; c) thermoforming of thermoplastic starch materials can be simulated more accurately by an elasto-plastic model and the LS-DYNA algorithm in comparison with a hyperelastic membrane model.

This work has provided useful information on thermoforming of thermoplastic starch materials with particular reference to the design of thermoforming tools and to the careful control of processing conditions including preheating. It has also laid a solid foundation for future work on how the moisture variation impacts on the formation of defects such as incomplete forming due to material hardening and fracture due to loss of ductility.

Table of Contents

List of Tables

List of Figures

Notation and abbreviations

In general capital bold upper case letters were used to denote tensors and matrices and bold lower case letters were used to denote vectors. Another notation convention was adopted to use the same letter to denote a vector, or a tensor and their elements with the only difference that non-bold letters were used to denote the elements. So for example the entries of matrix $\mathbf{A}$ were denoted as A_{ij}, and the components of vector $\mathbf{x}$ were denoted by x_i. The list below summarizes some of the basic symbols used in this work followed also by a list of abbreviations.

A list of notations used in this work

Symbol	Explanation
$\mathbf{X}$	point coordinates in reference (undeformed) configuration
$\mathbf{x}$	point coordinates in current (deformed) configuration
$\mathbf{F}$	the deformation gradient tensor
$\mathbf{C}$	the right Cauchy-Green deformation tensor
$\mathbf{B}$	the left Cauchy-Green deformation tensor
$\mathbf{R, Q}$	the rotational tensors
$\mathbf{U}$	a symmetric positive definite in the polar decomposition $\mathbf{F = RU}$ of $\mathbf{F}$
$\mathbf{V}$	a symmetric positive definite in the polar decomposition $\mathbf{F = VR}$ of $\mathbf{F}$
$\mathbf{L}$	the velocity gradient tensor, as in $\dot{\mathbf{F}} = \mathbf{LF}$
$\mathbf{D}$	rate of deformation tensor, as in $\mathbf{D} = \frac{1}{2}\left(\mathbf{L} + \mathbf{L}^T\right)$
$\dot{\mathbf{x}}$	the velocity vector
T	temperature, °C
t	time, sec
$\mathbf{u}$	the displacement vector, as in $\mathbf{X} \rightarrow \mathbf{x} = \mathbf{X} + \mathbf{u}$
$\mathbf{u}_h$	the finite element solution approximating $\mathbf{u}$
ε	total strain
ε_s	shrinkage strain
$\lambda_i^2, i = 1, 2, 3$	the eigenvalues of $\mathbf{C}$ and $\mathbf{B}$

Symbol	Explanation
λ_s	shrinkage stretch, as in $\lambda = \lambda_s \lambda_{mech}$
λ_{mech}	mechanical stretch (see above)
$d\lambda$	the plastic multiplier
$v_i, i = 1, 2, 3$	the eigenvectors of $\mathbf{C}$ and $\mathbf{U}$
$v_i^*, i = 1, 2, 3$	the eigenvectors of $\mathbf{B}$ and $\mathbf{V}$
$\boldsymbol{\sigma}$	the Cauchy stress tensor
$\boldsymbol{\sigma}'$	deviatoric stress tensor
$\overset{\nabla}{\boldsymbol{\sigma}}$	the Jaumann stress rate tensor
σ_e	effective or von Mises stress
σ_y	the yield stress
$\boldsymbol{\Pi}$	the nominal stress tensor
$\boldsymbol{\Pi}^T$	the first Piola stress tensor
$\mathbf{S}$	the second Piola-Kirchoff stress tensor
v	volume in current configuration
V	volume in reference configuration
$e_i, i = 1, 2, 3$	the standard base vectors
$\mathbf{n}$	the unit normal with respect to the current configuration
P	the magnitude of the applied pressure
p	the hydrostatic pressure in the constitutive relation for incompressible materials
$\dot{p}$	effective plastic strain rate
ρ	Density
W	the strain energy function
C	concentration
MC	moisture content
E	Young's modulus
h_0	initial thickness of a sheet
$\mathbf{I}$	the identity matrix
div	divergence, e.g. $\text{div}\mathbf{F} = \nabla \cdot \mathbf{F} = \dfrac{\partial F_1}{\partial x_1} + \dfrac{\partial F_2}{\partial x_2} + \dfrac{\partial F_3}{\partial x_3}$
:	double-dot product operation (i.e. $A : B := tr\left(A^T B\right)$)

Symbol	Explanation
superscript e	stands for elastic in denoting the elastic part of elasto-plastic quantity
superscript p	stands for plastic in denoting the plastic part of elasto-plastic quantity

A list of abbreviations used in this work

Abbreviation	Explanation
DSC	differential scanning calorimetry
HIPS	high impact polystyrene
PCL	polycaprolactone
PET	polyethylene terephthalate
PHA	polyhydroxyalkanoates
PHB	polyhydroxybutyrate
PLA	polylactic acid
PVC	polyvinyl chloride
TPS	thermoplastic starch

Acknowledgements

I wish to express my gratitude to my supervisors, Professor Jim Song and Professor John Whiteman for their continued encouragement and invaluable suggestions during this work. I also would like to express my appreciation to Dr. Michael Warby for help with programming, development of the FORTRAN simulation and numerous suggestions on this thesis.

Furthermore, I wish to acknowledge the Food Link Programme (Grant CSA 6439/FT1505), Department of Environment, Food and Rural Affairs, UK, for their financial support.

I am indebted to Pregis UK for technical assistance with the thermoforming of the Plantic® R1 material. Particularly, I wish to thank Bill Colquhoun from Pregis UK, who has enabled the thermoforming trials and provided support with the experiments. I also wish to thank to Plantic® UK for providing their material.

Sincere thanks are extended to Dr. Helen Copeland and Dr. Kun Qi for help in understanding starch and processing of thermoplastic starch materials. Thanks are also extended to Dr. Yunxin Gao for inspiring the idea of investigation of moisture content effects.

Finally, I would like to express my special thanks to my family for their love and never-ending support. I am forever indebted to my wife for her patience and understanding. Special appreciation goes to my mother for her invaluable support and encouragement. To her I dedicate this thesis.

Chapter 1. Introduction

1.1 Background of the project

In everyday life almost all consumer goods purchased come with packaging. The current global packaging industry is worth approximately $600 billion per annum and has maintained a high growth rate at approximately 12% annually (Klingbeil, 2002). A wide range of materials is used in packaging applications including metals, glass, paper-based materials, plastics, or combinations of these as composites. Over 67 million tones of packaging waste were generated in the EU in 2002, comprising about one third of municipal solid waste. Whilst significant improvements have been achieved in recycling or reuse of metals, glass and pulp-based packaging (Northwood & Oakley-Hill, 1999), relatively little success has been achieved in reducing the amount of plastic packaging waste going to landfills. Packaging is the single largest user of plastics, (Web1), which consist of a large number of different types, each of which may contain different processing additives such as fillers, colorants and plasticisers. They may also be coated with or made into a multilayer composite of different polymers to enhance performance. The difficulties in collecting, sorting, transporting, cleaning and re-processing post-use plastic packaging materials often render attempts of recycling non-economical. In recent years a wide range of bioplastic packaging materials have been developed from renewable plant resources in an attempt to reduce the reliance on oil-based polymers and to facilitate composting of used packaging. Among these materials, (Web2) those based on starch are the current front runners. Such materials fall largely into the following categories:

- Thermoplastic starch (TPS) materials such as Plantic™, (Web1), Potatopac™, (Web2) and Greenfill™, (Web3), consist of starch modified by thermal/mechanical destructurisation of the native structure and the addition of plasticising additives to enhance mechanical properties (Arvanitoyannis & Biliaderis, 1998; Baumberger et al., 1997).
- Complex of starch and biodegradable plastic materials such as Mater-Bi™, (Web4), Bioska™, (Web5), and Bioplast™, (Web6), are starch compounded or grafted with mostly synthetic biodegradable plastics. These include

polylactide, polyhydroxybutyrate or polyhydroyalkanoates, (Petersen et al., 2001), polylcaprolactone, (Av´erous et al., 2001; Matzinos et al., 2002), aliphatic polyester, (Ratto et al., 1999), and polyester-urethane, (Seidenstucker & Fritz, 1998).

- Bioplastics chemically derived from starch. NatureWorks[TM] Polylactide, (Web7), for instance, is produced by fermentation of starch to produce lactic acid followed by polymerization.

Cost, performance and processability are among the major challenges for bioplastic to compete with oil-based plastic packaging. Despite the currently higher costs compared with the traditional plastic counterparts, many bioplastics have found increasing applications in packaging (Web8), and it is expected that bioplastics will be increasingly more cost-competitive with the increase in production scale and increase in oil price. Significant technological development has been achieved to produce bioplastic packaging with comparable functionalities to those of traditional plastics (Widdecke et al., 2007/2008).

Thermoforming is the most common process for production of packaging containers from sheet materials and has been used successfully for many of the bioplastics (e.g. (Web1; Web4; Web8)). For thermoplastic starch, the high starch concentration (normally at more than 70%) gives rise to certain difficulties in controlling materials behaviour during thermoforming. This arises from the fact that starchy materials are inherently hydrophilic and moisture content within the materials influences their thermoformability. Water is a plasticizer in starch and thus is normally used to reduce viscosity of the starch melt during sheet extrusion. When the starch material is dried, a certain amount of moisture is retained in the sheet materials and equilibrated with the humidity of the storage environment. This can range from typically 5–15 wt% depending on the material formulation and relative humidity in the storage. When the starch material is heated during thermoforming, the moisture level will reduce with time and will result in a change of the material behaviour in addition to the change due to temperature variation. Loss of moisture results in an increase in the glass transition temperature of the material (Av´erous et al., 2001), which in turn gives rise to high flow stress and lower elongation limit. Thus, both temperature and moisture content need to be taken into account when an attempt is made to model the thermoforming process of such materials.

1.2 Project aims

The aims of this project are:

1. To characterise mechanical properties of a typical thermoplastic starch using a commercially available material Plantic$^{®}$ R1. This involves both tensile tests at different temperatures with specimens equilibrated at different humidity levels and measurements of volume shrinkage of the material due to moisture loss.
2. To establish a constitutive equation taking account of the effect of such moisture content and temperature on flow behaviour of the material.
3. To simulate computationally the thermoforming process of the material so as to predict its flow behaviour during a forming process, taking into account the effect of moisture loss.
4. To perform experimental thermoforming trials with the material and produce samples suitable for verification of the computational model.

1.3 Approaches

The specimens were equilibrated with predetermined humidity levels controlled by the use of saturated salt solutions so as to achieve different moisture contents. For the purpose of determination of behaviour of the material under different moisture contents and temperatures uniaxial tensile tests were conducted both at room temperature and at elevated temperatures using a temperature chamber; an infrared heater was used in order to reduce heating time so as to minimise moisture loss from the specimens. The stress-strain curves were obtained for different moisture contents, temperatures and strain rates.

Based on the experimental results a hyperelastic constitutive equation was established. The equation incorporated combined effects from moisture content and temperature. A finite element code was written in FORTRAN and applied to simulate the thermoforming process. Effects of moisture loss on flow behaviour of

the sheet and its shrinkage were investigated with this model. The resultant thickness distribution was compared with that of an experimentally thermoformed structure.

Thermoforming trials were carried out with the material in order to produce samples suitable for thickness measurements and verification of computational models. To simplify the geometry an axisymmetric shaped mould was chosen. The thickness distribution of the thermoformed structures was measured and averaged from three measurements.

The model was then improved by taking account of plastic flow of the material choosing an elasto-plastic material model with isotropic hardening so as to reduce the significant discrepancy in the measured and predicted thickness distribution by the hyperelastic model. The parameters for the constitutive equation were obtained from fitting to the experimental curve obtained at a high cross-head speed at the temperature of thermoforming process so as to minimise the effect of moisture and thus being able to neglect moisture loss and volume shrinkage of the material. The effect of this approximation was assessed by comparing with results from a case where the stress-strain curve was obtained at a lower cross-head speed and thus higher moisture loss. To overcome the difficulties experienced with convergence using an implicit ANSYS code the computational model discretised using three-dimensional solid elements was solved using LS-DYNA explicit solver. The model was also used to investigate the effect of contact friction with walls of the die.

Chapter 2. Literature review

This chapter first gives a brief review of starch-based bioplastics. The usual processing techniques for plastics, including extrusion and thermoforming process, are then described. These processes are also applicable to thermoplastic starch materials. As finite element modelling has become an increasingly important tool to simulate the thermoforming process in order to assist mould design and process control research works in this area are reviewed. This leads to the identification of the need for this work.

2.1 Introduction to starch-based biodegradable plastics

According to ASTM standard D-5488-84d a "biodegradable" material is:

"capable of undergoing decomposition into carbon dioxide, methane, water, inorganic compounds, or biomass in which the predominant mechanism is the enzymatic action of microorganisms, that can be measured by standardized test, in a specified period of time, reflecting available disposal condition."

Based on this a range of plastics can be classified as biodegradable plastics or biopolymers. It should be noted that a rate of biodegradation which satisfies the biodegradation standard is not only dependent on raw material but also on chemical structure, thickness and geometry of the final products, as shown in Table 2.1 (Nolan-ITU, 2002).

Table 2.1. Maximum thickness of registered biodegradable compostable plastics to satisfy biodegradation standard (Stevens, 2003).

Producer	Type	Register number	Maxim. biodegrad. thickness (μm)
Biotec	Bioplast GF 120/13	7W0001	160
Bayer	BAK 1095	7W0002	2000
Mitsui Chemicals Europe GmbH	Lacea	7W0004	250
Monsanto Europe S. A.	Biopol D311GN	7W0006	1000
BASF	Ecoflex	7W0011	120
Novamont S. p. A.	Mater-Bi ZIO1U	7W0012	1200
Cargill Dow Polymers LLC	EcoPla 1	7W0014	1650

Biodegradable plastics can be based on natural or synthetic biopolymers (see Table 2.2). Natural biopolymers are based primarily on renewable resources, such as starch and cellulose, while many synthetic biopolymers which posses certain degrees of inherent biodegradability are petroleum based and thus produced from non-renewable resources.

Table 2.2. Key composition of selected commercial biodegradable resins (Stevens, 2003).

Category	Polymer	Trade Name
Biosynthetic	Poly(β-hydroxy butyrate-co-β-hydroxy valerate)	Biopol (Monsanto)
	Poly(lactide)	EcoPla, NatureWork (Cargill Dow) Lacea (Mitsui Chemicals)
	Pullulan	Pullulan (Hayashihara)
Chemosynthetic	Poly(butylene succinate)	Bionolle 1000 (Showa Highpolymer)
	Poly(butylene succinate adipate)	Bionolle 3000 (Showa Highpolymer)
	Poly(butylene succinate terephthalate)	Biomax (DuPont)
	Copolyester	Ecoflex (BASF)
	Copolyester	Eastar Bio (Eastman Chemicals)
	Polycaprolactone	Tone (Union Carbide)
	Poly(vinyl alcohol)	Airvol (Air Products and Chemicals)
	Poly(ester amide)	BAK (Bayer)
Natural polymer-based	Cellulose acetate	EnviroPlastic-Z (Planet Polymer)
	Starch-based polycaprolactone	Bioplast (Biotec)
	Starch-based plastic	Mater-Bi (Novamont)

2.1.1 Starch

Native starch exists in granular form and is a complex carbohydrate, which at ambient temperature is insoluble in water. It can be found in many plants, as a storage molecule inside leaf chloroplasts, seeds and tubers. Humans consume starch contained in various foods providing 70–80% of calories consumed worldwide. In addition to being used for its nutritional value, starch is used to alter the properties of many foods, e.g. for gelling or thickening. Starch and products derived from starch are also important in the paper and textile industries. Recently starch based materials have emerged as promising alternatives to synthetic polymers because starch is a renewable and biodegradable (Chiou et al., 2005) resource.

Depending upon its botanical source starch consists of different levels of two polysaccharides: amylose and amylopectin. The behaviour of these types and their blends in now presented.

Amylose

Amylose is essentially a linear polymer composed of an α-1,4-linked D-glucopyranose (ring form of D-glucose) (Figure 2.1) and a small amount of α-1,6-branch linkages. The α-1,4-linkages promote formation of a helix structure. Amylose can be made of several thousands glucose units, and depending on the botanical source it has a degree of polymerization (DP) of about 1,500-6,000. Molecular weights of amylose are in the range of 10^5 to 10^6 g·mol^{-1} (Galliard, 1987).
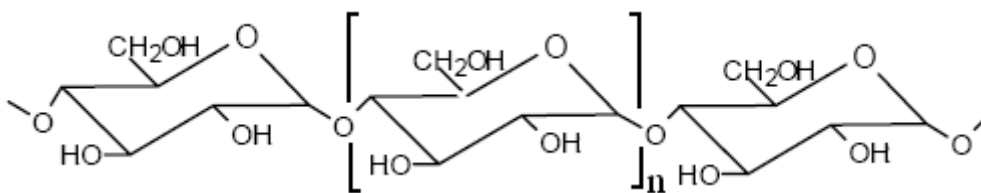
Figure 2.1. Chemical structure of amylose (Stevens, 2003).

Amylopectin

Amylopectin is a branched polymer composed of α-1,4-linked D-glucopyranose connected by α-1,6-linked branch points (Figure 2.2). Branching occurs every 20 to 25 glucose units. Amylopectin is one of the largest, in terms of the degree of polymerisation, biopolymers known with typical molecular weights being in the region of 10^8 g·mol^{-1} (Parker & Ring, 2001). The degree of polymerization of amylopectin is in the range of 300,000 to 3,000,000.
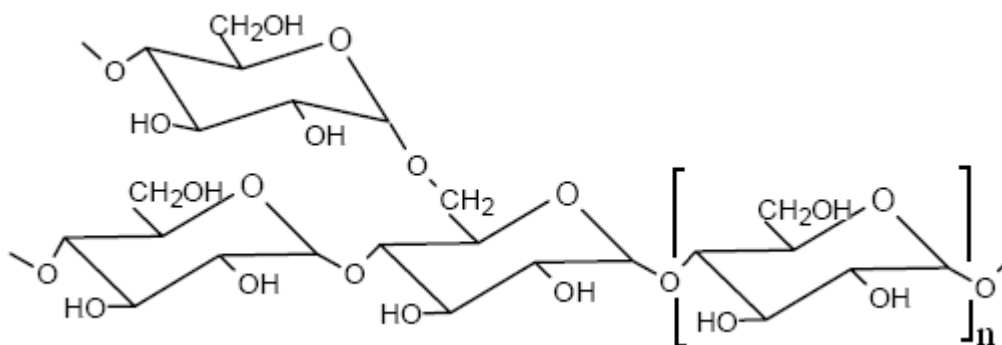
Figure 2.2. Structure of amylopectin (Stevens, 2003).

Starch granules

Amylose and amylopectin occur naturally in the form of semicrystalline starch granules, with crystallinities, depending on moisture content, in the region of 30%. A number of crystalline forms are known, but the most common ones are A and B type. The A type consists of starch double helices packed into monoclinic arrays and can be found in cereal starches. The B type can be found in tubers and is a more highly hydrated and open structure, consisting of double helices packed in a hexagonal array (Parker & Ring, 1995). A mixture of both crystallinities has been distinguished as type C, commonly found in legumes. The size and shape of starch granules differ and depends on their botanical source. Diameter of granules generally range from less than 1 μm to more than 100 μm. Granules can be regular (e.g. spherical, ovoid or angular) or quite irregular in shape. Starch granules contain small amounts of proteins, lipids and ash, as well up to 12% moisture at ambient temperature and humidity.

Gelatinisation and melting

When a starch granule is heated in the presence of water, its native crystalline structure is disrupted and it swells irreversibly to many times its original size. This process is called gelatinization. Gelatinisation gives rise not only to swelling, but also to loss of original crystallinity and solubilisation in water. The temperature at which starch begins to undergo these changes is referred to as the gelatinisation temperature. Because not all the granules of a given starch begin to gelatinise at exactly the same temperature, the gelatinisation temperature is more appropriately defined as a relatively narrow temperature range rather than one specific temperature. These temperature ranges also vary depending on the source of the starch.

The melting temperature of starch depends highly on water content, as well on its crystalline structure; the lower the water content, the higher the melting temperature. For low water content starch the melting temperature is experimentally inaccessible due to thermal degradation, and it can only be predicted for dry A-type starch to be in the range from about 220 to 270°C (Parker & Ring, 1995). Thus,

starch on its own cannot be used in the packaging industry and has to be blended with other polymers, which have plasticising capabilities, e.g. sorbitol and glycerol.

Retrogradation

Retrogradation takes place when gelatinised starch is cooling. During this process starch chains begin to re-associate and form crystalline structures. The molecules of different starches re-crystallise differently, i.e. amylose molecules have greater tendency to re-associate than amylopectin and form polymer aggregates relatively fast. However, amylose re-crystallisation is irreversible, while amylopectin re-crystallises reversibly, and after long enough time the extent of crystallinity of amylopectin becomes comparable to that found in native starch granules, i.e. in the region of 30% (Parker & Ring, 1995). The re-crystallisation of amylopectin is often referred to as physical aging of starch. As the retrogradation process occurs, the starch paste becomes increasingly opaque and rubbery displaying a tendency to release water.

Re-crystallisation of amylopectin can contribute to the life time of the products made of starch-based bioplastics being relatively short, and thus, many commercial bioplastics are composed of high amylose starch, reducing the effect of retrogradation.

Glass transition behaviour and plasticizers

When the cooling rate is sufficiently high to avoid crystallization, starch granules take an amorphous form. This phenomenon is referred to as the rubber glass transition and is characterised by a glass transition temperature T_g. It can be experimentally determined by for example differential scanning calorimetry (DSC) methods, where a change in heat capacity during glass transition is observed.

The glass transition temperature of dry starch is experimentally inaccessible due to thermal degradation. However, the addition of water to starch granules highly depresses the glass transition temperature meaning that water acts as a strong plasticizer to starch. At 20% w/w water, the T_g reaches room temperature (Chinachoti & Vodovotz, 2000). Although T_g reduces with addition of water, in terms of tensile strength, strain-at-brake and toughness, water has been shown to

have anti-plasticization capabilities below about 9% w/w level (Chang et al., 2000). Because water is volatile and small changes in its content can lead to large changes in mechanical behaviour, other non-volatile plasticizers, e.g. glycerol and sorbitol have been employed to produce more stable plasticisation effects on starch (Parker & Ring, 2001).

2.1.2 Starch-based biopolymers

Biopolymers are polymers produced by living organisms, e.g. starch, proteins and DNA. Starch-based biopolymers are made from non-food crops and thus are renewable, unlike oil-based polymers. Growth of plants absorbs CO_2, which is released when biopolymers degrade, thus a carbon neutral cycle can be completed. This helps reduce CO_2 emissions and the reliance on oil.

Starch-based materials contain typically more than 40% starch by weight (Stevens, 2003). The starch is generally used in its gelatinized or destructured state i.e. its crystallinity has been destroyed to obtain a thermoplastic melt. Starch content needs to exceed 60% before significant increase in biodegradability occurs (Nolan-ITU, 2002). As the starch content is increased, the polymer composites become more biodegradable and leave fewer residues. Biodegradation of starch based polymers is a result of enzymatic attack at the glucosidic linkages between the sugar groups leading to a reduction in chain length and splitting off of sugar units (monosaccharides, disaccharides and oligosaccharides) that are readily utilized in biochemical pathways (Nolan-ITU, 2002).

Biodegradable starch based polymers can be distinguished between thermoplastic starch and starch blends with other polymers.

Thermoplastic starch

Thermoplastic starch plastics (TPS) have gelatinized starch (usually amylose) content greater than 70% and with the use of specific plasticizing agents (e.g. glycerol, sorbitol) thermoplastic materials can be produced with good mechanical performance properties and inherent biodegradability (Nolan-ITU, 2002). Examples of commercially available thermoplastic starch materials are Potatopak[TM]

manufactured by Potatopak Limited (Web11), Plastarch[TM] Material manufactured by PSM North America/Teinnovations (Web12) and Plantic[TM] manufactured by Plantic Technologies Limited (Web10). Plastarch[TM] and Plantic[TM] are produced from non-genetically modified corn starch and Potatopak[TM], as its name suggests, is made from potato starch. For the purpose of this project the Plantic® R1 was chosen, which is supplied in the form of thermoformable sheets, as a representative of this group of materials. The Plantic® R1 is a material that has found many applications in the food packaging industry and its broader description is given in the next chapter.

Such high starch content TPS are highly hydrophilic. Their properties change drastically with moisture content variation within the materials and on direct contact with water they can readily disintegrate. This feature limits the materials to packaging in relatively dry environments such as packaging of the dry foods and confectioneries. However the restrictions can be overcome through blending with other biopolymers, nanoclay inclusion, as described below or surface crosslinking.

Starch blends with other biopolymers

In order to meet performance requirements for different applications starch is often blended with synthetic biopolymers with inherent biodegradability, e.g. aliphatic polyester, PBS/PBSA polyester or polyvinyl alcohol (see Table 2.2) and these materials are often referred as starch complexes. Usually starch content in such bioplastics is less than 60%, and inclusion of starch give rise to enhanced biodegradability by enzymatic attack from microorganisms (e.g. fungi and bacteria). This weakens the polymer chain structure, increases the surface to volume ratio and allows the biopolymer to disintegrate into small fragments to assist further biodegradation.

Examples of starch complexes with other synthetic biopolymers are Mater-Bi[TM] (Web4), Bioska[TM] (Web5) and Bioplast[TM] (Web13). Synthetic biopolymers used in starch complexes include polylactide (PLA), polyhydroxybutyrate (PHB) or polyhydroxyalkanoates (PHA) (Petersen et al., 2001), polycaprolactone (PCL) (Av´erous et al., 2001); (Matzinos et al., 2002), aliphatic polyester, (Ratto et al., 1999), and polyester-urethane (Seidenstucker & Fritz, 1998). These biopolymers biodegrade at slower rate than starch and therefore starch complexes with such biopolymers tend to biodegrade at relatively lower rates.

Starch-clay nanocomposites

Nanoclay enhanced material is not considered in this project and the following description of starch-clay nanocomposites is given as a further review of improvements in starch-based materials.

Nanoclay naturally forms stacks of plate-like structures with thickness of individual platelet of ~1nm. The width of each platelet is over 200 times its thickness and thus results in very high aspect ratio. Nanoclays are naturally hydrophilic and thus do not mix and/or disperse easily within most polymer matrices. Moreover, the stacks of clay platelets are held tightly together by electrostatic forces and chemical modifications (Web14) and/or intensive mechanical shearing are commonly employed to weaken the bonding so as to disperse the individual platelets. Depending on the states of dispersion of nanoclay in polymers, it can be *intercalated*, where the layered structure remains although space between layers may be increased by absorption of polymer molecules (see Figure 2.3), *exfoliated*, where the ordered layered structure is lost and individual platelets are dispersed (see Figure 2.4), or in an intermediate state between the two.

Figure 2.3. Intercalated nanoclay (Web14).   Figure 2.4. Exfoliated nanoclay (Web14).

Addition of nanoclays to starch formulations is often employed to improve properties of starch-based biopolymers. With only a few percent (by weight) of clay, starch nanocomposites can exhibit significant improvements in mechanical, thermal and gas barrier properties compared with pure starch (Park et al., 2003). The

influence of the inclusion of nanoclay on the mechanical properties of the material is shown in Table 2.3 and on water vapor barrier properties in Figure 2.5. The presented data indicate that inclusion of about 5% nanoclay is optimum amount for improving these properties. The effectiveness of property enhancement by nanoclays depends on the strength of interaction, e.g. hydrophilicity and compatibility with the thermoplastic starch and the chosen nanoclay (Park et al., 2003). It should be noted that the quality of dispersion of the nanoclay also plays a major role. Highly dispersed nanoclay composites have much enhanced properties compared with those of poorly dispersed composites.

The most commonly used nanoclay in the starch-clay nano-composites is montmorillonite (MMT), a member of the smectite family. The thickness of the single layer montmorillonite is around 1 nm (Web14).

Table 2.3. Tensile properties of TPS/clay nanocomposites with various amounts of nanoclays: Cloisite Na^+ and Claoisite 30B (Park et al., 2003).

Blend composition	Property	
	Tensile strength (MPa)	Elongation at break (%)
TPS 97.5/Na^+ 2.5 wt%	2.79	48.9
TPS 95/Na^+ 5.0 wt%	3.32	57.2
TPS 90/Na^+ 10.0 wt%	3.20	52.0
TPS 97.5/30B 2.5 wt%	2.75	45.7
TPS 95/30B 5.0 wt%	2.80	44.5
TPS 90/30B 10.0 wt%	3.00	45.7
TPS 100 wt%	2.61	47.0
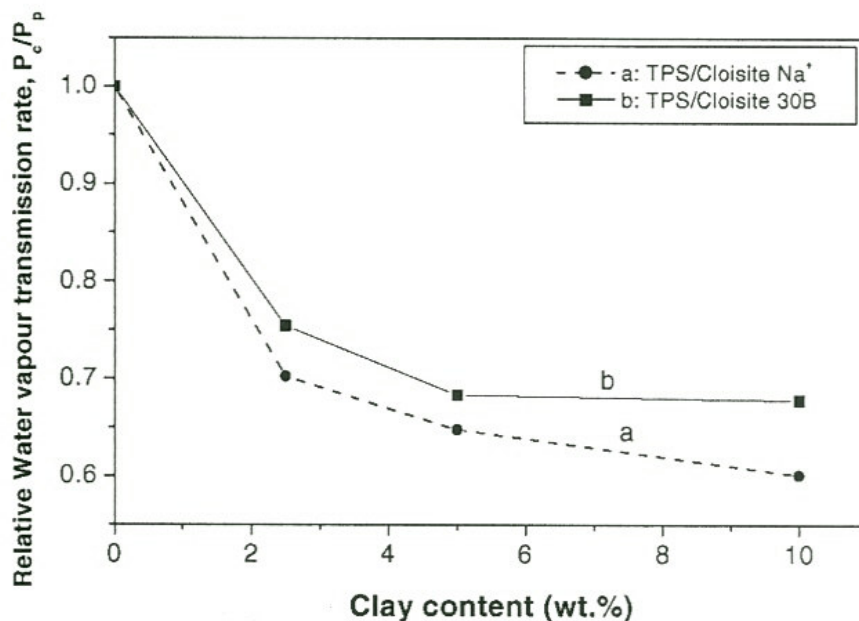
Figure 2.5. Effect of nanoclays (Cloisite Na$^+$ and Cloisite 30B) contents on the relative water vapour transmission rate of TPS/Cloisite Na$^+$ and 30B nanocomponents at 24°C.

2.1.3 Biopolymers derived from starch

Biopolymers may also be commercially derived from starch. One such commercially available biopolymer is polylactic acid (PLA). There are several manufacturers of PLA in the world, with NatureWorks LLC, a subsidiary of Cargill Corporation in the USA being the largest producer (Web15). Other manufacturers include

- Toyota in Japan (Web16);
- Hycail and PURAC Biomaterials in the Netherlands (Web17) and
- Galactic in Belgium (Web18).

In one method of production of PLA starch is first processed into dextrose. Using fermentation, dextrose is then turned into lactic acid and converted by condensation into lactide followed by polymerisation of lactide into PLA as shown in Figure 2.6.
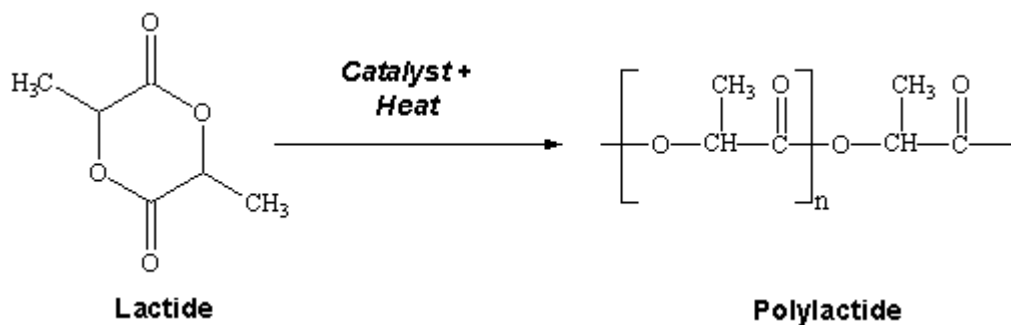
Figure 2.6. Polymerisation of lactide into PLA (Web9).

Mechanical and physical properties of PLA

PLA has a glass transition temperature of between 55 and 65° C and a density of 1250 kg·m^{-3}. It has good transparency comparable to that of polystyrene and PET. The high tensile strength of PLA (50-140 MPa) in comparison with e.g. PET (55-75 MPa) means that the gauge can be reduced, thus minimizing both weight and cost. PLA does have some disadvantages that must be taken into account when processing this material. Due to the low glass transition temperature PLA products suffer from low thermal stability of size and shape. Although not immediately visible, PLA tends to have a yellow tinge and a slight milkiness. During the manufacture of films, PLA has a strong tendency to adhere to the rollers, and its brittleness means that cutting and punching are also critical factors (Schanzer et al., 2005).

Disposal properties of PLA

PLA is designed to fit a broad range of waste management systems. Traditional polymers are either recycled, incinerated or sent to landfill, whereas PLA offers opportunities for the post-use products to be biodegradable by composting and anaerobic digestion in addition to traditional waste managements mentioned above (Davies, 2006). PLA is biodegraded in an initial step by means of hydrolytic decomposition, whereby the polymer is degraded into monomers. These are then decomposed biologically by microorganisms. The decomposition process greatly depends on the environmental conditions. In commercial composting facilities,

where high temperature of about 70°C can be maintained, complete decomposition can be achieved within between 30 and 50 days (Schanzer et al., 2005).

2.2 Introduction to sheet extrusion and thermoforming

2.2.1 Sheet extrusion

The sheet extrusion process is widely used for making thermoplastic into sheet form for subsequent processing such as calendaring, coating, lamination and thermoforming. It may also involve mixing additive fillers and pigments into polymers for property modifications. Extruders fitted with slit dies and a down-stream calendar are normally employed for sheet extrusion. Depending on the application, different types of extruders can be selected. The common features to all extruders are that they consist of a single or twin screw within barrels, which can be heated or cooled to obtain a desired temperature profile; feeding ports for feedstock or additive input and a die fitted at exit for profiling the extrudate (Schenkel, 1966a).

In such plastic extruders the raw material is conveyed from the feed port to the die. On the way it is heated to the required plastification temperature both by external heating elements in the barrels and by internal shearing of the materials. It is further mixed and finally extruded from the die by the pressure which is generated by the screws (Schenke, 1966a). The materials flow from right to left in a typical schematic representation of a single screw extruder shown in Figure 2.7.
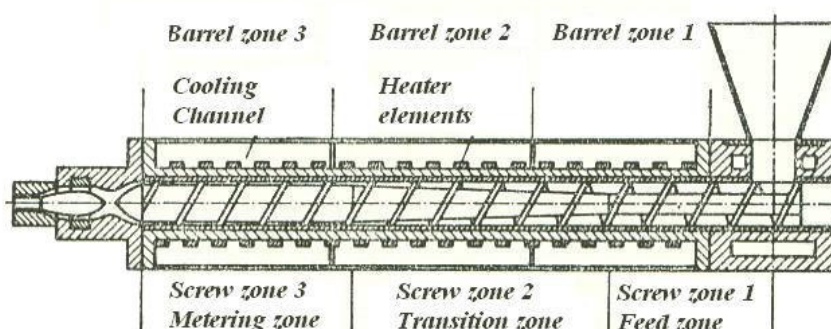
Figure 2.7. Extruder zones (Schenkel, 1966b).

Three individual zones in the single-screw extruder can be distinguished (Schenkel, 1966c), namely:

- The feed zone, which is expected to take in the solid raw material and additives compress, pre-heat and convey the materials forward.

- The transition zone, where the transition of the material from solid to a thermoplastic takes place.

- The discharge or metering zone, which takes the plastified or molten material from the transition zone in order to homogenise it and extrude it from the die under necessary pressure and at a constant throughput.

Flat sheet extrusion is based on the principle of shaping a melt that has been plasticized and homogenized in an extruder, into a sheet, cooling and stabilizing the sheet by means of calendaring. The sheet is trimmed to a desired width and wound up in roles (Figure 2.8). Depending on sheet thickness and application, a distinction is made normally between "thin film" of typically 10 to 50 μm thickness, e.g. for wrapping or lidding applications, and "thin sheet" of typically 100 to 400 μm thickness or "thick sheet" of typically 0.2 to 2.5 mm thickness for e.g. thermoforming applications. Multilayer sheet can also be made by feeding different materials using additional extruders through the adaptor (b) seen in Figure 2.8.
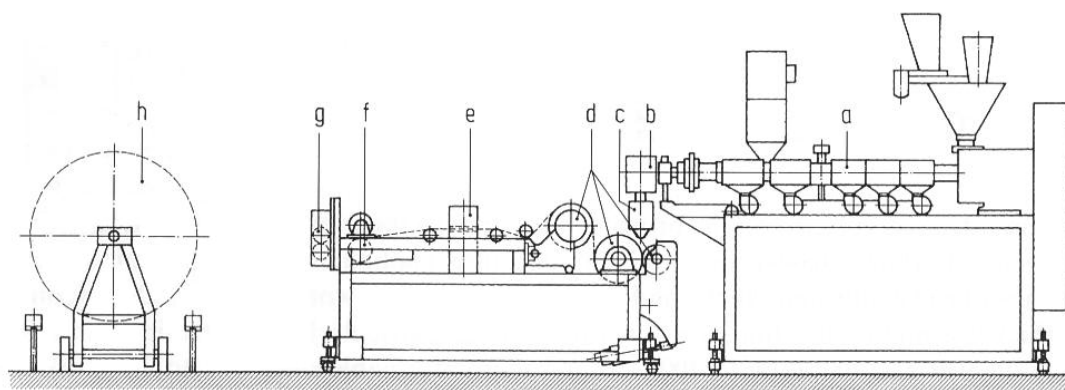
Figure 2.8. Line for production of sheet/film (Schenkel, 1966d). (a) extruder; (b) adaptor; (c) die; (d) cooling rolls; (e) thickener; (f) take-off unit; (g) edge trimmer; (h) winding station

The sheet/film is either wound in rolls after being trimmed to finished dimensions for separate processing, or undergoes direct in-line conversion in a process such as uniaxial or biaxial stretching, or thermoforming (Schenkel, 1966d).

2.2.2 Thermoforming process

Thermoforming is a manufacturing process in which heated thermoplastic sheet is inflated under positive pressure or vacuum into final shape in the form of a thin-shell object defined by a mould. This process can be described in the following steps:

- Clamping;
- Heating;
- Inflation (free or into/onto a mould);
- Cooling and
- Trimming.

In modern thermoforming deformation of the sheet is obtained by application of pressure. Either vacuum or air pressure is used to produce the differential pressure needed to force the sheet into or onto the mould. The former technique is normally referred to as vacuum forming and the latter pressure forming. In pressure forming positive air pressure is applied to push the sheet into the corners of the mould and air trapped between the mould and the sheet is evacuated through outlet holes in the mould (see (a), Figure 2.9). In vacuum forming a vacuum is created by withdrawing the air between the clamped sheet and the mould so that the ambient air pushes the sheet into the mould (see (b), Figure 2.9).

(a) pressure or
(b) ambient air

Clamps

Heated sheet

Mould

(a) evacuation or
(b) vacuum
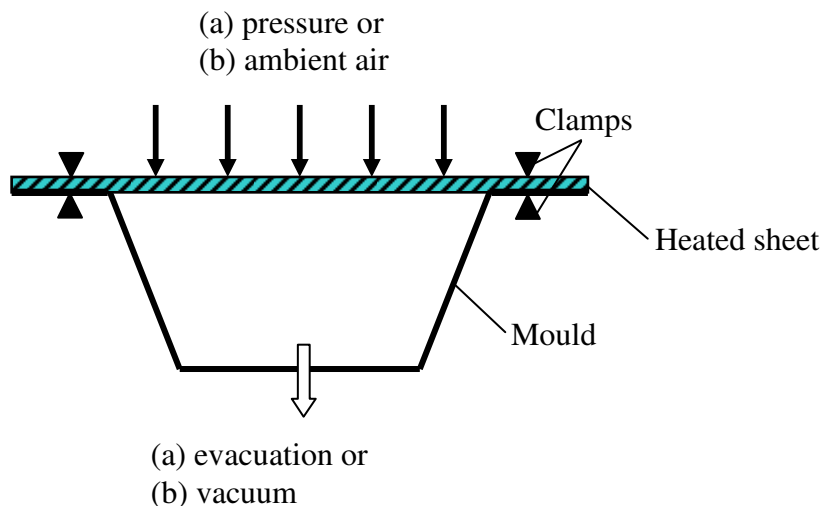
Figure 2.9. Schematic representation of pressure and vacuum forming.

Other variations of thermoforming methods include free blowing, billow drape forming and matched die moulding.

In free blowing the heated sheet is clamped and stretched by application of air into a free-form shape, as a "bubble" (see Figure 2.10). A photocell can be employed to sense the degree of inflation of the bubble so as to control the air pressure. Since the inflating air is slightly cooler than the sheet, the sheet cools and stabilizes in the free-form shape. Clearly free blowing can only generate simple shaped objects, such as semi-spherical structures. Further modifications are possible to overcome this problem as described in billow drape forming.

Lamp   Sheet   Photoelectric Eye
Bubble
Clamp
Mold
Inflating Air
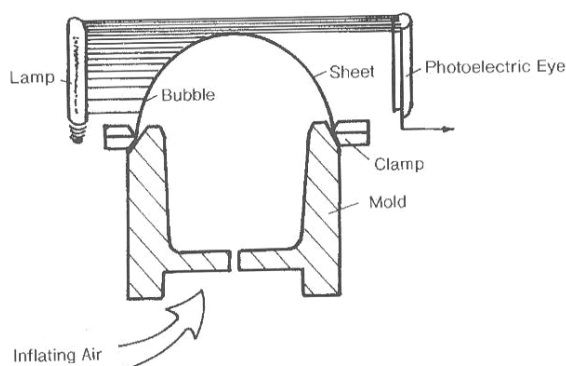
Figure 2.10. Schematic representation of free blowing (Throne, 1996).

In billow drape forming the first step is to inflate the heated sheet to a controlled height with internal air pressure (see Figure 2.11a). The mould is then pressed into the top of the prestretched sheet (Throne, 1996). The air pressure is maintained to push the sheet onto the mould surface to assist forming and additional vacuum can be applied to enhance the forming as shown in Figure 2.11b.

(a)   (b)
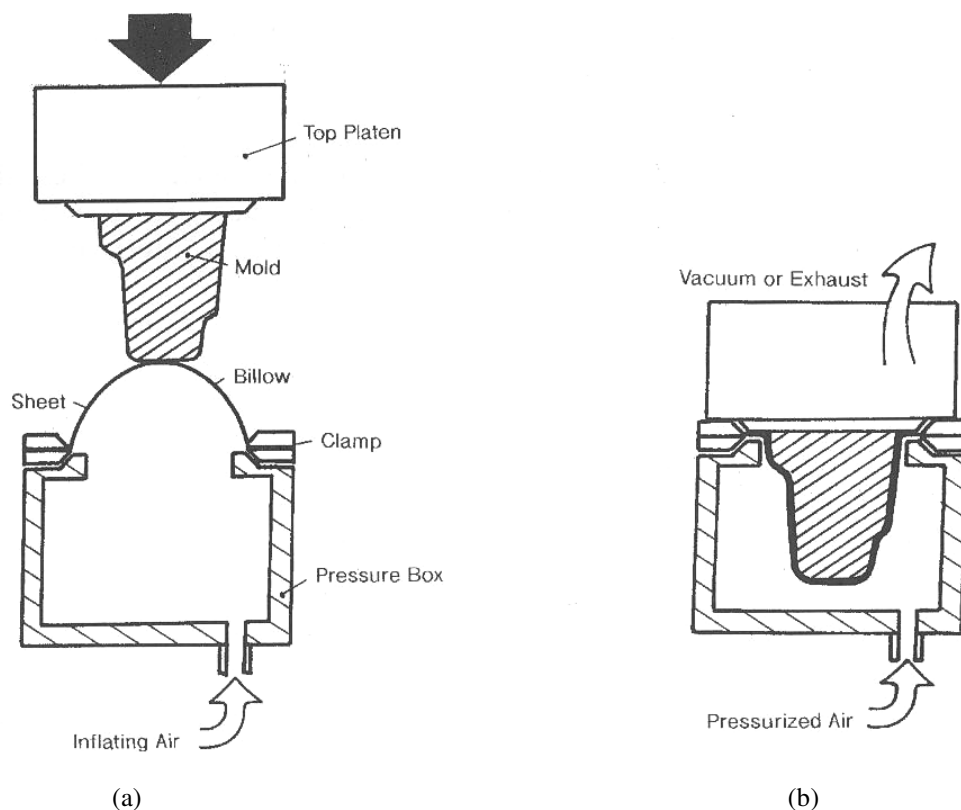
Figure 2.11. Billow drape forming, assisted by (a) applied air pressure and (b) both air pressure and vacuum to shape the sheet against the mould surface (Throne, 1996).

In matched die forming the heated sheet is clamped and positioned between two mould halves (see Figure 2.12). As the mould halves close, a vacuum may be also generated by withdrawing the air through holes in the mould to assist forming.
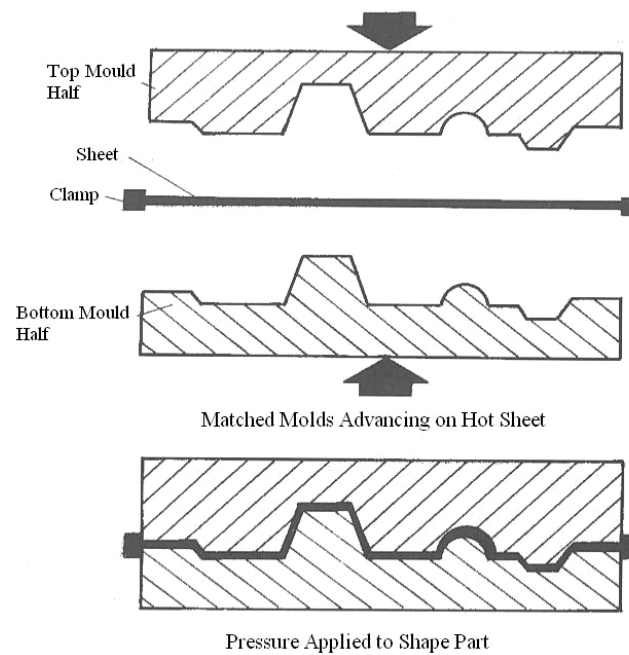
Figure 2.12. Schematic representation of matched die forming (Throne, 1996).

Generally speaking a uniform thickness distribution is a desirable characteristics in thin-sheet objects but this is difficult to achieve in the thermoforming techniques described so far. This is due to sticking of the sheet on contact with the mould which prevents further stretching of the whole sheet. As a result the final thermoformed structure tends to have thick walls in the places where the sheet touched the mould first and thin walls where it touched last. Prestretching of the sheet before forming helps achieving more even distribution of walls thickness, thus use of a plug can improve the wall thickness distribution. The first step in multi-step forming is usually a form of sheet stretching, such as plug assist or billowing. The prestretched sheet is then pressed against the mould surface.
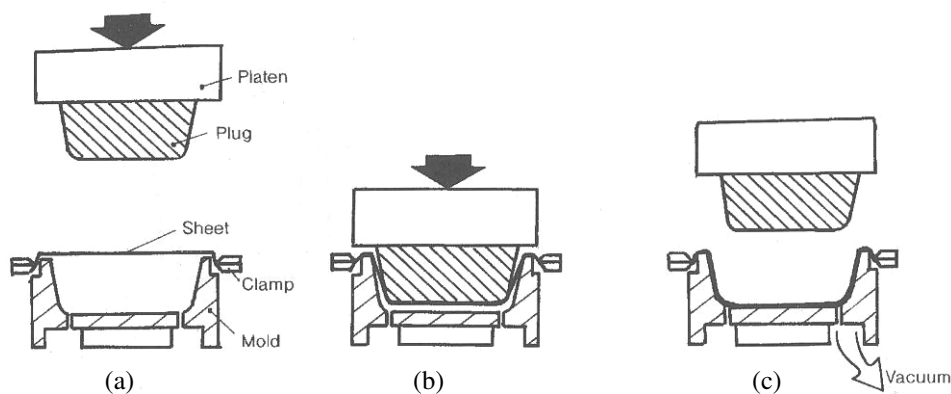
Figure 2.13. Schematic representation of plug-assisted vacuum forming in stages (Throne, 1996).

a) The plug forms contact with the central area of the sheet and pushes the sheet into the mould;

b) The plug reaches its desired position;

c) Withdraw of the plug and application of vacuum to complete the thermoforming.

The most common form of plug assisted thermoforming is plug assisted vacuum forming as shown in Figure 2.13. The sheet is prestretched by pressing the plug into it and forcing the sheet towards the bottom of the female mould cavity. Vacuum is then applied to pull the sheet against the mould surface (Throne, 1996). The use of a plug results in thicker sheet at the bottom and thinner sheet at the walls in comparison with thickness distribution resulting from traditional thermoforming. This can be explained by the fact that the central part of the sheet is stuck to the plug and the remaining part is being stretched while the plug is moving into the mould.

This thesis is restricted to computational modelling of traditional pressure driven thermoforming processes.

2.3 Modelling of thermoforming process

Numerical modeling of these thermoforming processes is performed primarily to understand the influencing factors such as material behavior during the forming process, temperature and rate of forming so as to assist with design of tooling and control of the thermoforming process. It helps reduce the amount of experimental work, modification of tooling and the number of thermoforming trials so as to cut costs. Work on the computational modelling of thermoforming of polymer sheets was undertaken at General Electric Corporation, in the 1980s/90s,

(deLorenzi & Nied, 1987; Nied et al., 1990; deLorenzi et al., 1991; Taylor et al., 1992; deLorenzi & Nied, 1999). In these works membrane models with elastic constitutive equations and discretisations based on finite element techniques were used. Warby, Whiteman and co-workers have also used elastic models with some extensions to include elasto-plastic and viscoelastic effects, whilst maintaining the membrane model in most cases, (Warby & Whiteman, 1988; Warby et al., 2003; Jiang et al., 2003; Karamanou, 2004; Karamanou et al., 2005). Simulation of thermoforming using a viscoelastic constitutive equation to capture the strain-rate dependence of plastic materials was also reported by Sala (2002). The above models produced convincing predictions of wall thicknesses and in all cases it was assumed that the temperature was constant throughout the forming process. Most of the published literature regarding this topic focused on modeling of oil-based polymers, there is lack of published work regarding modeling of biopolymers, particularly the starch-based biopolymers.

2.4 Roadmap of the thesis

This section gives a layout of the experimental and computational work:

- Chapter three contains the experimental work which was necessary to characterise the material behaviour in the context of temperature and moisture effects. The thermoforming trials needed to produce samples used for measurements of thickness are also included in this chapter;

- This is followed, in chapter four, by a description of a simple axisymmetric finite element model using hyperelastic constitutive equation, which takes into account the effects of temperature and moisture content on material behaviour. Effect of moisture content on material shrinkage and thermoforming pressure and final thickness distribution were modeled in details and comparison was made between the predictions from the hyperelastic model and the experimental measurements;

- Then, a more complex three-dimensional model with elasto-plastic constitutive equation is introduced in chapter fife. The model was built in ANSYS and solved using the dynamic explicit solver of LS-DYNA. A comparison of computational

prediction of thickness distribution between the two models and experimental measurements is provided;

- And finally the last chapter provides conclusion of the work and suggestions for future work.

Chapter 3. Experimental work

Experimental work necessary to characterise the material and understand its behaviour during thermoforming process is described in this chapter. In the first section description is given to the thermoplastic starch material used in this work. It is followed by methods of preparation and conditioning prior to testing and the description of tensile testing of the sample materials. Thermoforming trials carried out in Pregis and characterisations of the thermoformed trays are described and followed by measurements of diffusivity of water in the material, shrinkage and density changes associated with moisture loss.

3.1 The material - Plantic® R1

3.1.1 General features of the Plantic® R1 material

For the purpose of understanding of material behaviour, so as to establish suitable constitutive equations and moulding trials to evaluate the modelling results, Plantic® R1 thermoplastic starch material in the form of a sheet was obtained from Plantic Technologies Ltd (UK). The material is certified by EN 13432:2000 standard to be fully biodegradable and compostable. Its primary feedstock is a naturally high amylose starch (more than 70% amylose), derived from corn which has been hybridised over a number of generations. When starch is heated, the crystalline structure is disrupted and upon cooling, it recrystallises due to retrogradation. To prevent this, the high amylose starch has undergone a chemical modification process called hydroxypropylation prior to the sheet manufacturing (Web10). This process retards retrogradation and effectively plasticises the starch. The modified starch is then mixed with other polymeric and non-polymeric ingredients, plasticisers and processing aids known only to the manufacturer. It is called that Plantic® R1 has the following key features (Web10):

- The primary raw material source is renewable and sustainable;
- The ingredients are not genetically modified;
- It is certified Home Compostable to European Standards (EN 13432:2000);

- It is certified Biodegradable to European Standards (EN 13432:2000);

- It is certified for disposal in waste water to European Standards;

- It is suitable for food contact applications;

- It is inherently anti-static and oil resistant;

- It is sealable, printable and laser etchable.

Selected mechanical and physical properties of the material are presented in Table 3.1.

Table 3.1. Mechanical and physical properties of Plantic® R1 (Web10).

Property	Test Method	Value	Units
Density	ASTM D792	1.35 – 1.45	g/cm^3
Vicat Softening Temperature	ASTM D1525	130 – 135	˚C
Glass Transition Temperature, Tg	ASTM E1356	40 – 45	˚C
Nominal thickness	-	250	µm
Water Activity	PTM 03	0.5 – 0.65	-
Modulus of Elasticity (MD)	ASTM D882	2200 – 2400	MPa
Tensile Strength (MD)	ASTM D882	42 – 46	MPa
Strain at Break (MD)	ASTM D882	20 – 36	%
Tear Resistance (MD)	ASTM D1922	3.5 – 5.5	N
Linear Mould Shrinkage	ASTM D955	0.01	mm/mm
Coefficient of Friction, static	ASTM D1894	0.215	-
Coefficient of Friction, dynamic	ASTM D1894	0.17	-
Moisture vapour transmission rate[*]	ASTM E9600	140	g/m^2/24hrs
Oxygen transmission rate[*]	ASTM D1434	<0.01	cc/m^2/24hrs
Haze	ASTM D1003	15 – 20	%
60˚ Specular Gloss	ASTM D2457	80 – 85	%
Optical Transparency	ASTM D1003	89 – 93	%

* at 38˚C and 75% relative humidity

3.1.2 Manufacture of Plantic® R1

Plantic® R1 is extruded into sheet using industry standard equipment. The raw materials are conveyed to a feeder above an extruder. The extruder heats the starch and additions to form a melt. The extruded melt is then cast using a standard sheet extrusion die, optimised for Plantic® R1 flow characteristics onto a series of heated rollers, fed through a non-contact gauging system for control of thickness, and then into a dryer system to bring the moisture down to the required level. The sheet is then trimmed, slit as required, and wound onto rolls. The produced sheet is suitable for manufacture of trays using thermoforming process. Forming of Plantic® R1 trays takes place on standard pressure forming machines or vacuum/pressure forming machines with modified heating systems to ensure that the heating step does not dry the sheet (Web10).

Independent of the material used, the sheet and tray manufacture process produces up to 30% waste as standard, depending upon the tray dimensions and shape. Similar to all plastic regrind processes, there is some degradation in the material every time it is reprocessed. The use of reground Plantic® R1 has been qualified to two passes at 50% max usage, and is currently used in the process at 30% (Web10).
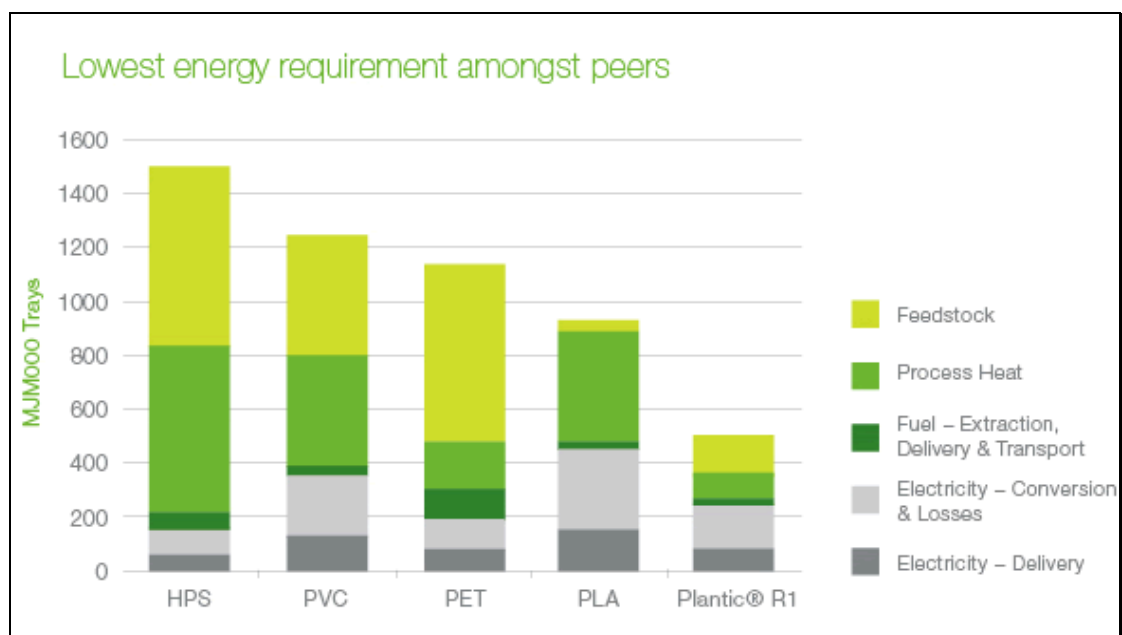
Figure 3.1. Comparison of the overall energy requirement from the life-cycle assessment of the Plantic® R1(Web10).

3.1.3 Environmental advantages of Plantic® R1

Plantic® R1 is made from renewable resources (corn starch) and helps reduce CO_2 emissions. It is fully biodegradable and certified home compostable eliminating the need for industrial composting facilities. In comparison to petrochemical-based polymers PET, PVC, high impact polystyrene (HIPS) and bio-based polymer polylactic acid (PLA), Plantic® R1 has the lowest impact in resource depletion, cumulative energy demand, acidification and waste to landfill (Web10), as shown in Figure 3.1.

3.2 Sample preparation and conditioning

Plantic® R1 sheet was, cut according to the British standard "BS 2782-3 - method 320C", into dumb-bell specimens and grouped into six batches. Each batch was conditioned for weeks in desiccators with constant humidity level achieved by using saturated salt solutions. The salt solutions used, the relative humidity level achieved (Carotenuto & Dell'lsola, 1996) and the resulting moisture content in the material after conditioning are given in Table 3.2. Moisture content in the material was measured with Mettler Toledo HR73 Halogen Moisture Analyzer. This involved drying a small sample (typically 1g) at a temperature of 150°C for 60min and monitoring the weight loss. The moisture content tabulated was then taken as the average of three measurements.

Table 3.2. Salt solution, relative humidity and equilibrium moisture contents in the conditioned samples (Carotenuto & Dell'lsola, 1996).

Salt solution	Potassium chloride	Sodium chloride	Sodium bromide	Potassium carbonate	Potassium acetate	Lithium chloride
Relative humidity, %	85.11±0.29	75.47±0.14	59.14±0.44	43.16±0.33	23.11±0.25	11.31±0.31
Moisture content, %	15.52	13.92	11.91	10.33	8.09	5.78

3.3 Tensile tests for characterisation of flow behaviour of the material

Tensile tests were carried out according to BS EN ISO 527-1:1996 (Plastics-Determination of tensile properties). In order to measure properties of Plantic$^{®}$ R1, tensile tests were conducted at different temperatures using samples conditioned at different moisture contents. Room temperature tests were performed on a Hounsfield H10KT Material Testing Machine fitted with a Tinius Olsen 100S extensometer in a room conditioned to 23°C and 50% relative humidity. An Instron Model 4206 Universal Materials Testing Machine retrofitted by Zwick and fitted with a temperature chamber was employed for the tests. As the temperature range prohibited the use of the extensometer, tensile strain was calculated based on the crosshead displacement and gauge length of the samples. To minimise the moisture loss during heating, a 1000W high response infrared heater was fitted in the temperature chamber close to the sample. The temperature of the sample was monitored by a thermocouple attached to the bottom part of the sample using a silver-based compound and an adhesive tape. To control the temperature of the sample the power of the infrared heater was lowered when the sample reached desired temperature and moved away to a distance that allowed maintaining the temperature within ±2°C accuracy. It was observed that use of excessive high heating rate could result in foaming of the specimens as shown in Figure 3.2c. Foaming occurs when specimens are heated at high heating rate to temperature ranging from ~95°C to 105°C.
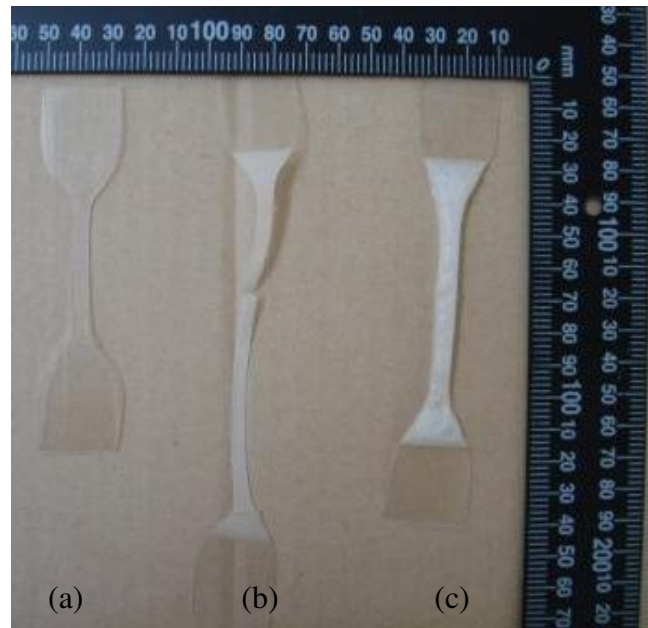
Figure 3.2. Tensile specimens before and after testing. a) Sample before test. b) Sample after test. c) Foamed sample due to excessive heating rate and temperature.

The results from tensile tests were averaged from data of 5 samples (according to the standard) and the engineering stress and strain produced by the equipment were recalculated for true stress and true strain. The engineering stress in this case corresponds to the entry Π_{11} of the nominal stress $\mathbf{\Pi} = (\Pi_{ij})$, where $\mathbf{\Pi} = \mathbf{F^{-1}\sigma}$ for an incompressible material. Thus, the engineering stress can be recalculated to true stress using equation (3.1).

$$\sigma_{11} = (1 + \varepsilon_E)\Pi_{11} \tag{3.1}$$

The engineering strain was recalculated to true strain using equation (3.2).

$$\varepsilon_T = \ln(1 + \varepsilon_E) \tag{3.2}$$

A range of uniaxial tensile tests were carried out with the Plantic® R1 material. Figure 3.3 and Figure 3.4 present stress-strain results at room temperature where change in moisture content in specimens is negligible during a test.

The effect of moisture content can be observed from Figure 3.3. Increase in moisture reduces modulus in the elastic region and overall stress level at a given strain and results in a greater elongation at break. This effect is related to moisture plasticisation and decrease of the glass transition temperature with increase of the moisture content.

Figure 3.4 shows the effect of the rate of deformation with the top curve corresponding to the highest cross-head speed and the bottom curve to slowest speed. The figure shows that there is a relatively low dependence on the rate of deformation in comparison to that on the moisture content. This has led to the conclusion that the modelling of the material behaviour may be simplified by neglecting viscoelastic properties of the Plantic® R1 material so as to focus on the effect of moisture content and temperature.
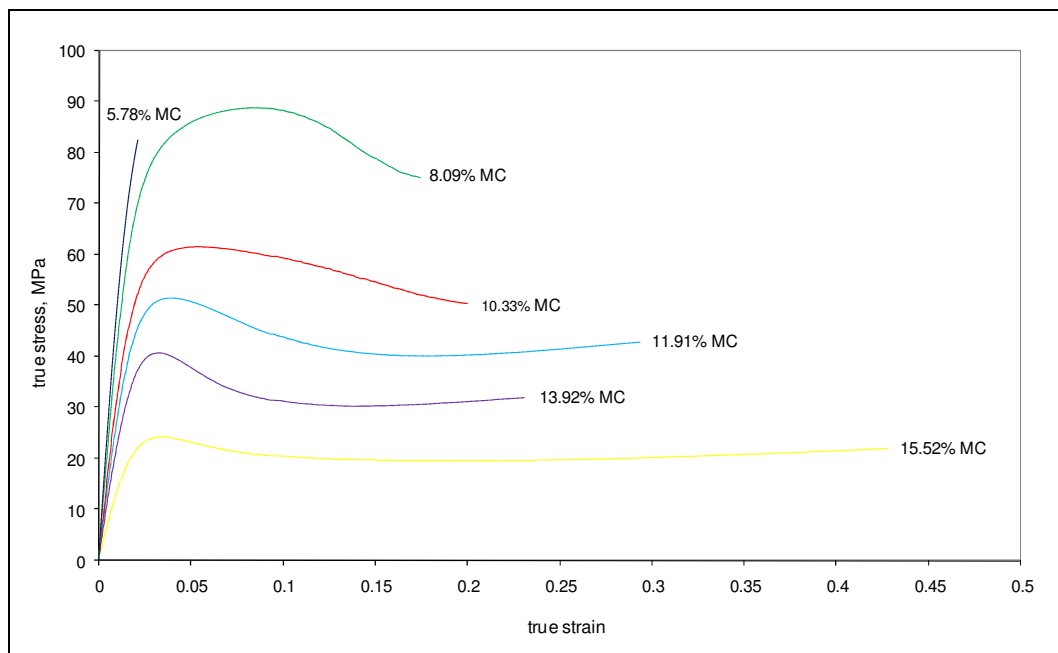
Figure 3.3. Tensile test results for the Plantic® R1 material equilibrated at different moisture contents. Test conditions: temperature = 23°C, cross-head speed = 200mm/min.
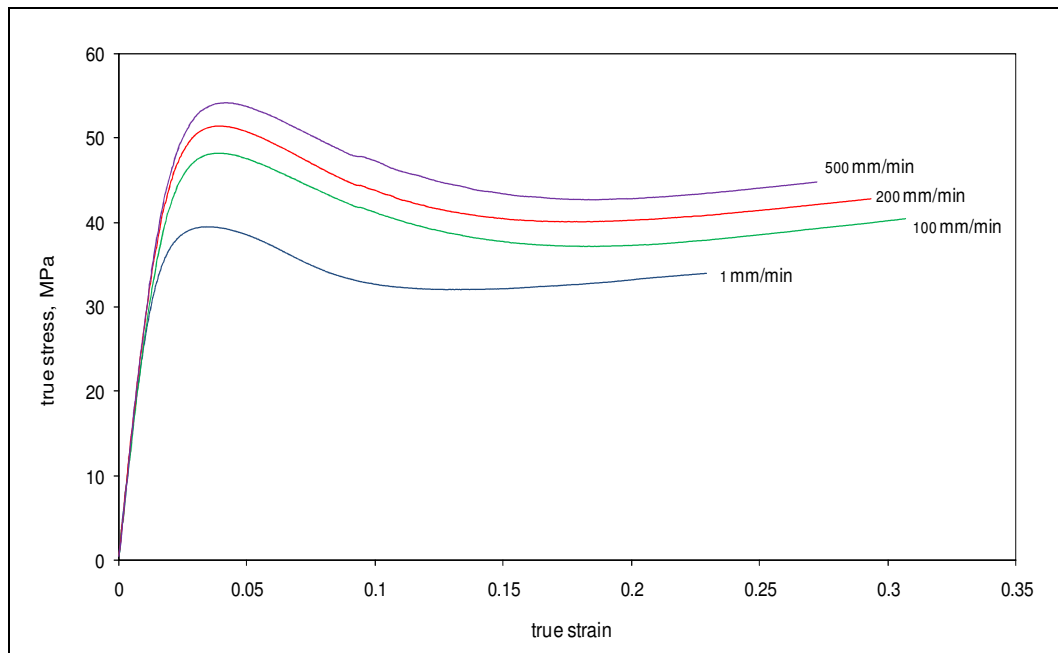
Figure 3.4. Tensile test results for the Plantic® R1 material equilibrated at 11.91% moisture content. Test conditions: temperature = 23°C at different cross-head speeds.

Results presented in Figure 3.5 support such opinion. The tests were carried out at an elevated temperature of 85°C where moisture loss becomes more significant than at room temperature. One would still expect that, with increase in cross-head speed, the stress level would increase based on the observations in Figure 3.4. However, cross-head speed also effects the duration of the tests and hence the amount of moisture loss. With increase in the cross-head speed the duration of a test is shortened and the moisture loss from the sample is relatively lower than for samples tested at lower cross-head speeds. Clearly the effects of moisture content dominate the material behaviour and give rise to the reversed order of the stress levels. Finally, the effect of increasing temperature on material softening can be observed from Figure 3.6. The material behaviour in terms of the stress–strain relationship is thus dominated by the moisture content of the samples and processing temperature.
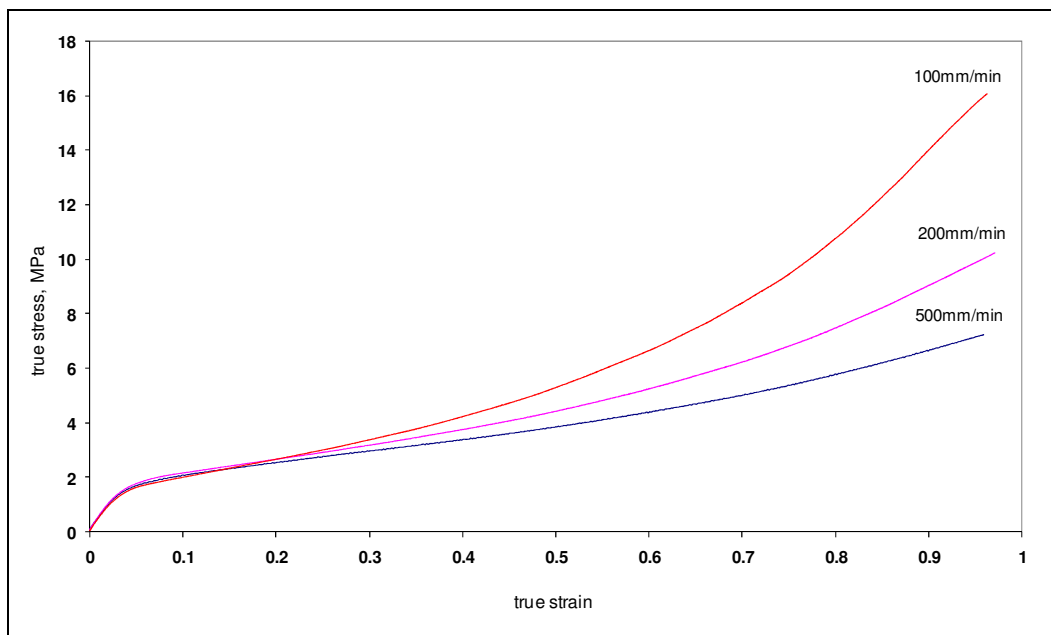
Figure 3.5. Tensile test results for the Plantic® R1 material equilibrated at initial 11.91% moisture content. Test conditions: temperature = 85°C at different cross-head speeds.
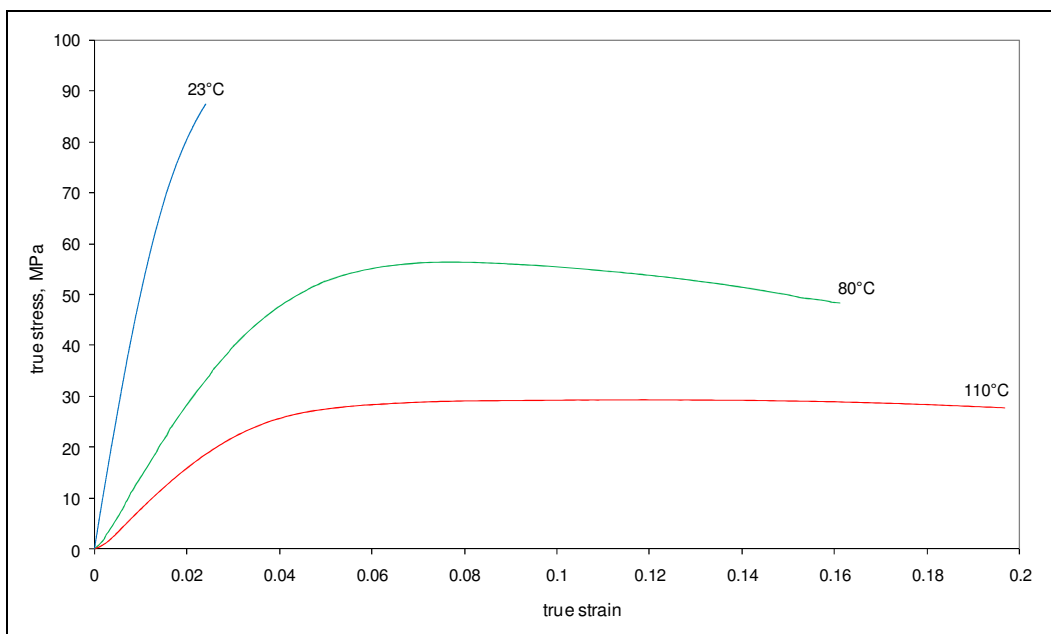
Figure 3.6. Tensile test results for the Plantic® R1 material equilibrated at 5.78% moisture content. Test conditions: cross-head speed = 200mm/min at different temperatures.

3.4 Thermoforming trials and measurements of formed trays

3.4.1 Thermoforming trials

Thermoforming trails were conducted in order to produce sample trays for evaluation of the computational results. The trials were performed in Pactiv (UK) Ltd, one of the major food packaging manufacturers in the UK. An industrial positive pressure thermoformer was employed for the trials. The heating chamber of the machine consisted of two heating plates located at the top and bottom so that a sheet material was heated from both sides. A mould as detailed in Figure 3.7 was fitted into the forming chamber equipped with a pressure box. A sheet of Plantic$^{®}$ R1 material with 500 μm nominal thickness was clamped in a frame trolley and inserted into to the heating chamber preheated to maximum temperature of 500°C. This temperature was chosen to achieve maximum heating rate so as to minimise moisture loss as loss of moisture decreases ductility and results in brittleness, which may additionally prevent thermoforming. Heating time thus became the only factor for controlling the sheet temperature. After a number of trials under the specified setup, a heating time of 4.5 sec was found satisfactory to give a sheet temperature of 85°C recommended by the supplier. The sheet temperature was measured with a thermocouple attached to the sheet with a thermal conductive compound for good contact. Heating procedure described here was clearly dependent on thickness of the sheet and appropriate heating temperature and duration should be identified for sheet other than 0.5 mm thick.

The sheet was then moved to the forming chamber as soon as it reached the desired temperature where it was stretched, with application of compressed air, into the mould held at room temperature. Figure 3.8 shows successfully thermoformed trays.

It was not possible to record the forming pressure because the machine was not equipped with a pressure gauge. The pressure affects mainly rate of deformation. Although it has been shown that the material flow behaviour is relatively insensitive to strain rate, a slow forming process by using a low pressure may result in high moisture loss and the effect will be assessed in later chapters.
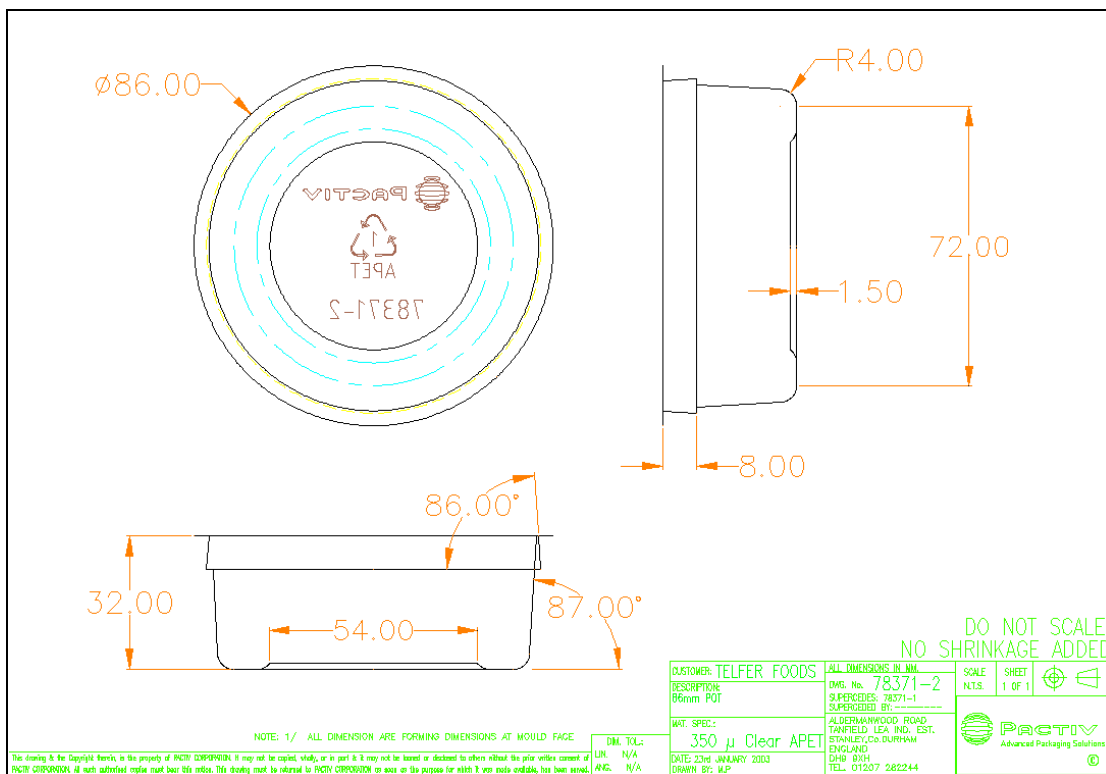
Figure 3.7. Dimensions of the mould used in this work.
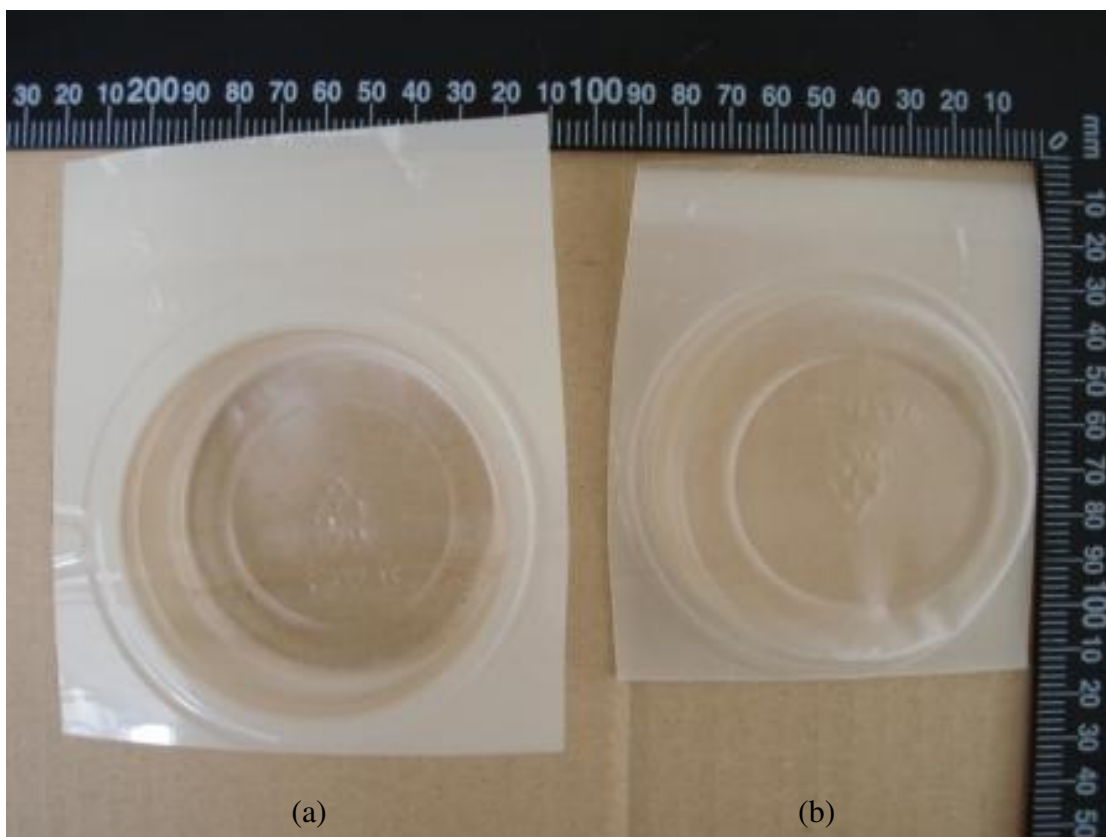
Figure 3.8. An example of successfully thermoformed tray. a) Viewed from top. b) Viewed from bottom.

3.4.2 Measurement of the formed trays

From thermoforming trials a satisfactory collection of trays was produced for measurements of wall-thickness distribution. Since the trays are axisymmetric, it was sufficient to measure their thickness along their radius. Selected trays were cut through their centre with a sharp scalpel and their thickness was measured with a digital calliper, as presented in Table 3.3. The measurements were performed at points indicated using the following division of the trays: from its centre the bottom flat part was divided by a constant interval of 5 mm, then a smaller intervals of 2 mm was used for the sunken corner step. The wall was also divided by an interval of 2 mm but the division was made along the wall and converted into radial positions. The averaged wall-thickness distribution from three measurements is presented in the Figure 3.9. The minimum thickness at the corner of the trays was 0.047 mm.

Table 3.3. Thickness measurements of thermoformed trays.

Radius, mm	Sample 1	Sample 2	Sample 3	Average thickness, mm
0.0	0.17	0.13	0.15	0.150
5.0	0.14	0.16	0.13	0.143
10.0	0.12	0.17	0.14	0.143
15.0	0.12	0.12	0.12	0.120
20.0	0.11	0.27	0.09	0.100
25.0	0.11	0.19	0.07	0.090
27.0	0.05	0.08	0.04	0.057
29.0	0.04	0.05	0.06	0.050
31.0	0.04	0.04	0.06	0.047
33.0	0.04	0.05	0.07	0.053
35.0	0.02	0.06	0.06	0.047
37.0	0.03	0.06	0.05	0.047
37.1	0.05	0.06	0.05	0.053
37.3	0.07	0.08	0.07	0.073
37.4	0.09	0.1	0.1	0.097
37.5	0.09	0.11	0.13	0.110
37.6	0.13	0.13	0.15	0.137
37.8	0.14	0.16	0.17	0.157
37.9	0.18	0.18	0.2	0.187
38.0	0.2	0.2	0.22	0.207
38.1	0.22	0.23	0.24	0.230
38.3	0.23	0.25	0.27	0.250
38.4	0.27	0.27	0.3	0.285
38.5	0.28	0.28	0.31	0.290
38.6	0.32	0.29	0.33	0.313

38.7	0.37	0.32	0.36	0.350
38.9	0.42	0.35	0.39	0.387
39.0	0.46	0.44	0.42	0.440
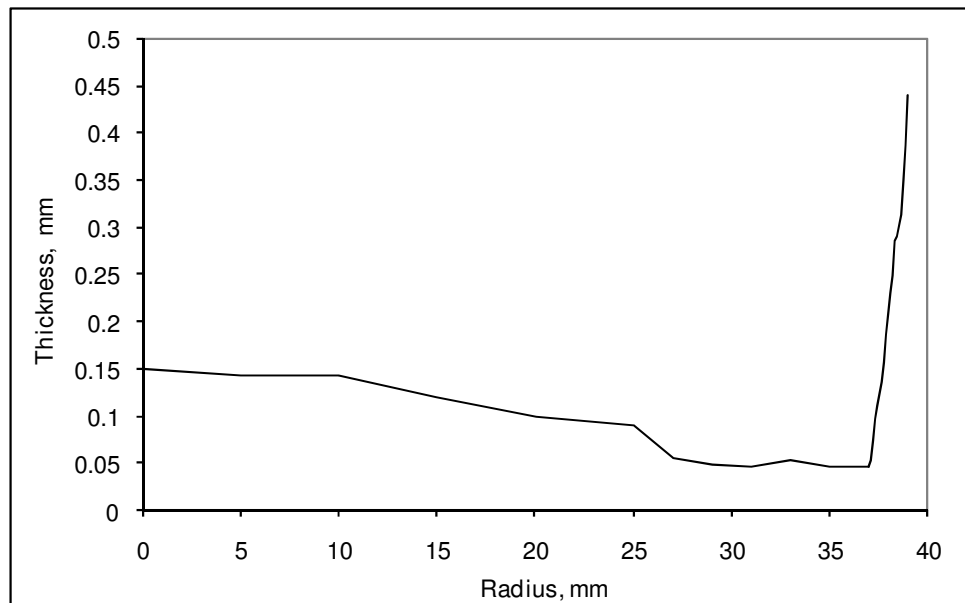
Figure 3.9. Averaged wall-thickness distribution of thermoformed trays.

3.5 Measurement of moisture loss and derivation of the diffusion coefficient

Moisture loss during tensile tests including both the heating and testing stage was measured. Table 3.4 presents the measurements for two crosshead speeds of 100 and 200mm/min respectively. As identical infrared heating was used to minimise moisture loss during heating stage, the moisture loss during heating stage can be assumed equal and hence the difference in overall moisture loss has resulted from different duration of the tensile tests.

Table 3.4. Moisture loss during tensile tests at two crosshead speeds.

Sample ID	Weight before test, g	Weight after test, g	Weight loss, g	Moisture content before test, %	Moisture content after test, %	Moisture loss,%[*]
Crosshead speed 100mm/min						
A1	1.36	1.34	0.02	11.91	10.60	11.00
A2	1.25	1.23	0.02	11.91	10.48	12.01
A3	1.26	1.25	0.01	11.91	11.21	5.88
Mean	*1.27*	*1.26*	*0.02*	*11.91*	*10.79*	*9.40*
Crosshead speed 200mm/min						
B1	1.20	1.19	0.01	11.91	11.17	6.21
B2	1.33	1.33	0.01	11.91	11.24	5.63
B3	1.26	1.25	0.01	11.91	11.21	5.88
Mean	*1.26*	*1.26*	*0.01*	*11.91*	*11.21*	*5.88*

* calculated from the weight loss

Although it was not possible to record the history of moisture loss, the overall moisture loss after the tests is known from the above measurements. The moisture loss presented in Table 3.4 may seem to be small but from Figure 3.5, the effect on stress-strain behaviour of the material can be significant.

As properties of the Plantic® R1 are moisture dependent, it is important to quantify moisture content and its loss during thermoforming process by taking into account of moisture loss by diffusion at the process temperature. Diffusion of water in carbohydrate polymers such as starch has been described for instance by Tromp et al. (1997) and Parker & Ring (1995). Diffusion process in starch-based materials is a complex phenomenon and according to Russo et al. (2007) diffusion in high-amylose TPS-blends, like the Plantic® R1 is temperature and relative humidity dependent. The diffusion is faster at higher temperatures and high relative humidity. Russo reports that diffusion coefficient D, in starch-based materials is exponentially dependent on concentration C, and it is of the form in equation (3.3).

$$D = D_0 e^{A(C/C_0)} \tag{3.3}$$

where D_0, A are constants and C, C_0 are concentrations in dimensions of [g/m^3], at a point in the material and at the surface respectively. In the case of concentration dependent diffusion the one dimensional Fickian diffusion equation is given by equation (3.4) (Crank, 1975a).

$$\frac{\partial C}{\partial t} = \frac{\partial}{\partial x}\left(D \frac{\partial C}{\partial x} \right) \tag{3.4}$$

A thorough investigation of water diffusion process in the Plantic® R1 is beyond the scope of this work and the diffusion coefficient was assumed to be constant, i.e. concentration independent.

Furthermore moisture loss or gain during tensile tests at room temperature and humidity (~50% relative humidity) was omitted as it is considered to be negligible in the scale of tests.

The focus is then to derive the equation for water diffusion governing moisture loss during thermoforming process at a temperature of 85°C. A method for determination of diffusion constants from desorption measurements described by Tromp et al. (1997) was used here. It involves drying the material at temperature of 85°C and measuring its weight loss. The temperature corresponds to the temperature of thermoforming process and high temperature tensile tests. Moisture loss during drying process was recorded at 2-minutes intervals and the drying curve is presented in the Figure 3.10. The same equipment as for the determination of moisture content was used as described in section 3.2.
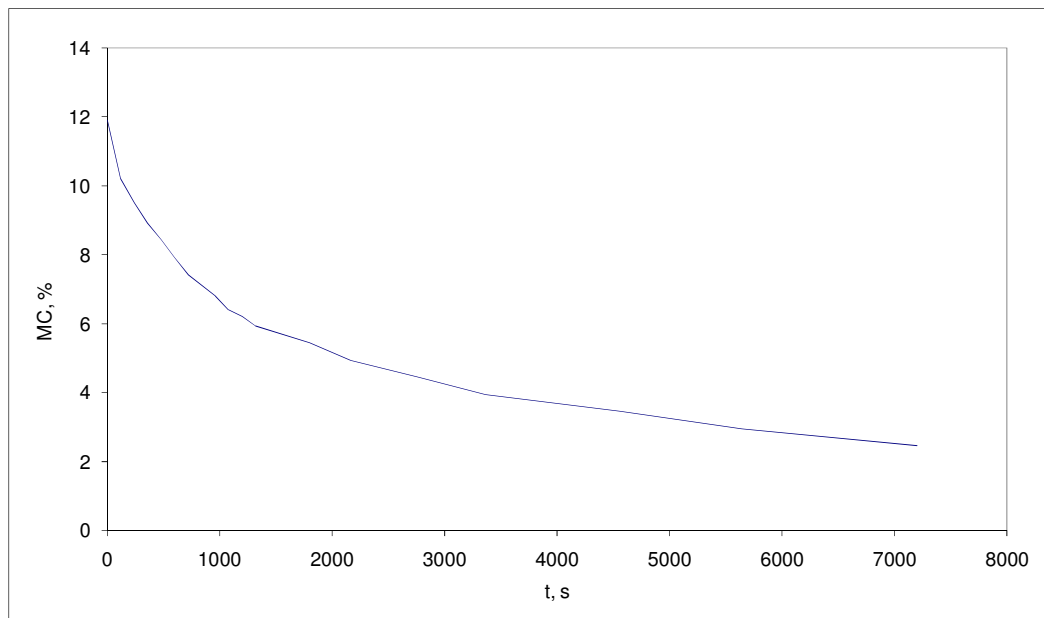
Figure 3.10. Loss of moisture content as a function of time of drying in Plantic® R1 with 11.91% initial moisture content. Drying temperature = 85°C. Sample size: 50x50x0.5mm.

The material shape for thermoforming process was a flat sheet and for tensile tests the sheet was cut into dumbbells as shown in Figure 3.2a. For simplification, the diffusion through the edges of the specimens was neglected and equation of diffusion in a plain sheet was chosen for the description of moisture loss during both thermoforming and tensile tests.

For a plain sheet occupying region $-l \leq x \leq l$ with uniform initial distribution of concentration the equation for moisture content at time t is given by equation (3.5) (Crank, 1975b; Tromp et al., 1997):

$$\frac{MC_t}{MC_0} = 1 - 2\left(\frac{Dt}{l^2}\right)^{\frac{1}{2}} \left\{ \pi^{-\frac{1}{2}} + 2\sum_{n=1}^{\infty} (-1)^n \, ierfc \, \frac{nl}{\sqrt{Dt}} \right\} \qquad (3.5)$$

where MC_0 is the initial moisture content, MC_t the moisture content at time t, and l is the sheet thickness. The diffusion constant D can be obtained by fitting equation (3.5) to the experimental data. Figure 3.11 presents the experimental curve of the moisture content decay, the blue line, as function of square root of time and the good fitting with equation (3.5), the red line, up to a time of 1225 seconds. This time scale is justified as thermoforming and tensile tests including heating time are normally completed in less than a minute. The calculated value of diffusion constant amounts to $\overline{D} = 7.5682e^{-12} \, \text{m}^2/\text{s}$.
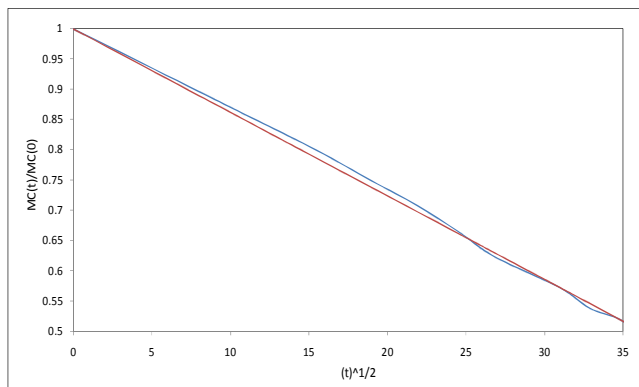
Figure 3.11. Curve fitting of the experimental moisture content decay (blue line) to the prediction from equation (3.5) to obtain diffusion constant for the Plantic® R1 at 85°C.

3.6 Shrinkage and density measurements

3.6.1 Measurement of shrinkage due to moisture loss

The shrinkage measurements were performed in two different ways. Volume shrinkage of samples upon drying was measured. Five 20cm×20cm×0.05cm samples of Plantic® R1 with 11.91% initial moisture content were dried for 24 hours in a vacuum oven at temperature of 120°C and their dimensional changes were measured. The experiments showed that Plantic® R1 shrinks in all dimensions during drying at similar level as shown in Figure 3.5.

Table 3.5. Measurements of volume shrinkage due to moisture loss.

Sample ID	Volume before test, cm^3	Volume after test, cm^3	Thickness shrinkage, %	First edge shrinkage, %	Second edge shrinkage, %	Volume shrinkage, %[*]
1	20.23	17.47	-8.38%	-2.65%	-3.27%	-13.65%
2	20.38	18.04	-5.37%	-3.55%	-2.89%	-11.46%
3	20.55	18.59	-3.37%	-3.32%	-3.04%	-9.55%
4	20.28	18.33	-3.25%	-3.33%	-3.13%	-9.64%
5	20.47	18.45	-3.74%	-3.23%	-3.20%	-9.91%
Mean	**20.38**	**18.17**	**-4.82%**	**-3.22%**	**-3.11%**	**-10.84%**

* calculated from volume measurements

Linear shrinkage measurement recording the change of one linear dimension as a function of time was also conducted to derive the relationship between shrinkage and moisture content. This was performed with use of TA Instruments DMA Q-800. A sample of the Plantic® R1 sheet was clamped inside a furnace chamber and allowed to freely extend or shrink. The chamber was then heated at a rate of 200°C/min to 85°C and held at this temperature. The change in length of the sample with time was recorded as strain by the instrument. As shown in Figure 3.12, the strain in the first ~30 sec (during heating to 85°C) was resulted from a combination of shrinkage due to moisture loss and the thermal expansion due the temperature increase which clearly dominated over the former during heating period. In the period that temperature was held constant at 85 °C, the linear shrinkage was solely attributable to the moisture loss.
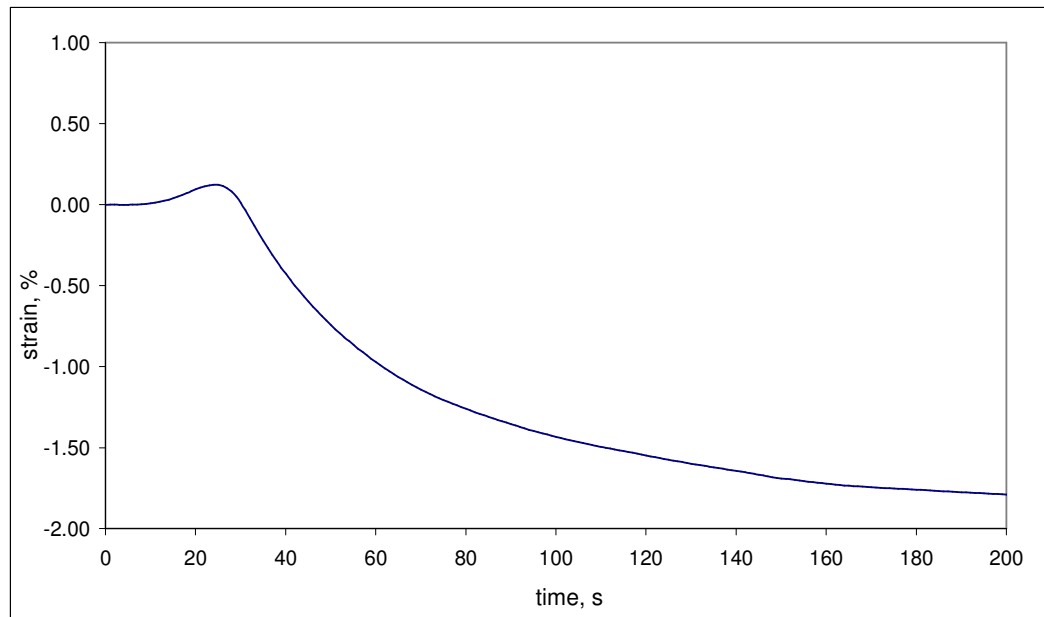
Figure 3.12. Linear shrinkage of the Plantic® R1 (with initial moisture content of 11.91%) with time when heated and held at 85°C.

Data in Figure 3.12, excluding the initial heating stage, were presented against moisture loss in Figure 3.13. The moisture loss was estimated from equation (3.5), as described in section 3.5, using the diffusivity D obtained before.
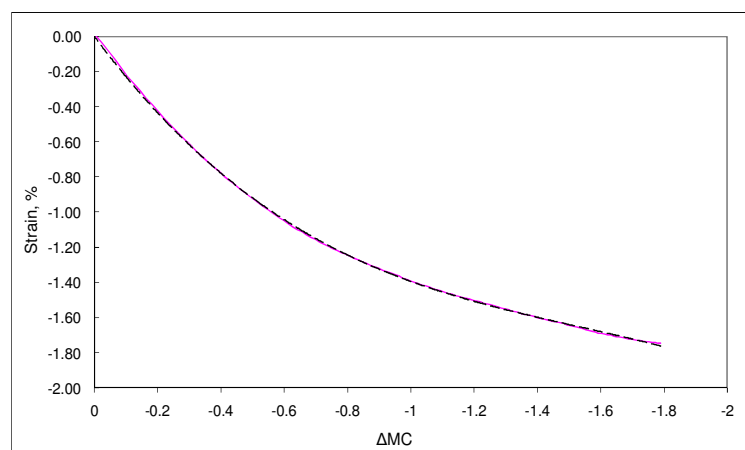
Figure 3.13. Shrinkage strain as function of moisture loss (red line) and quadratic fitting (the dotted black line).

Figure 3.13 gives an approximate relation between shrinkage strain and moisture loss which will be used in later chapters to model the effect of shrinkage on stress and thickness distribution. An equation relating shrinkage strain and moisture loss was obtained by fitting the strain-moisture loss curve with 2nd order polynomial and is given by

$$\varepsilon_{sh} = 1.3212(\Delta MC)^2 + 2.4268(\Delta MC) \tag{3.6}$$

where $(\Delta MC) = MC_t - MC_0$. The polynomial fitting is shown in Figure 3.13 as the black dashed line.

3.6.2 Measurements of density

Density measurements were performed according to BS EN ISO 1183-1:2004 Plastics - Methods for determining the density of non-cellular plastics. Method A - Immersion method for plastics in void-free form was used here. Because Plantic® R1 is water-soluble oil instead of water was used as the immersion liquid. The density was determined for samples conditioned according to section 3.2. The results of measurements are presented in Figure 3.14.
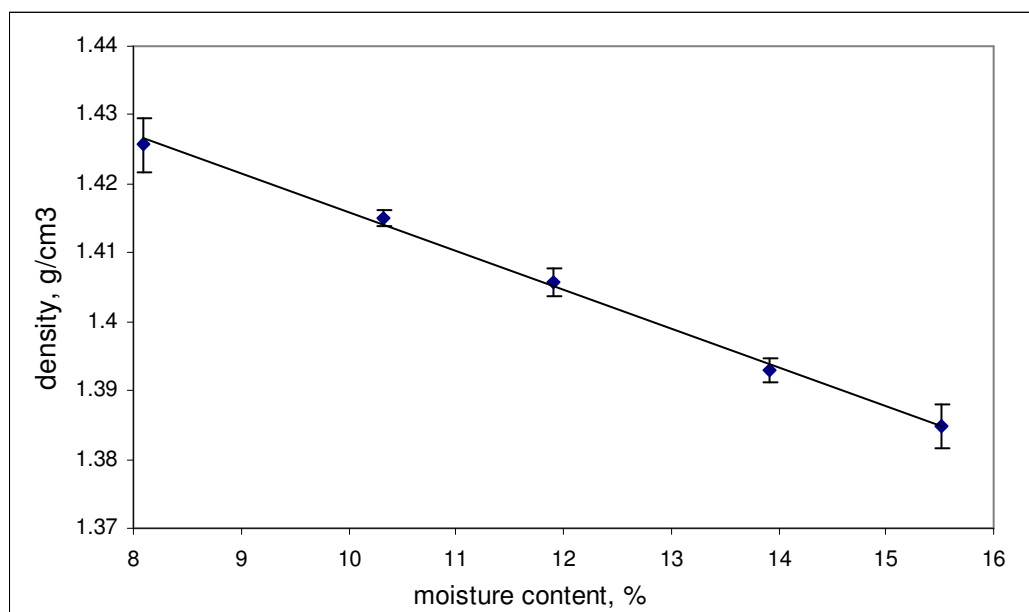
Figure 3.14. Density of Plantic® R1 against moisture content.

3.7 Summary

Experimental work carried out on Plantic$^{®}$ R1 was presented in this chapter. Results of tensile tests shown that the material flow behaviour depends strongly on moisture content, what is exhibited by shift in stress level for specimens with different moisture content. The stress-strain curves shift from elasto-plastic-like behaviour for high moisture content to elastic-like for specimens with low moisture content. Shrinkage due to moisture loss and diffusion coefficient were also investigated. Measurements of shrinkage showed that the material shrinks uniformly in all 3 principal directions. From thermoforming trials samples were produced and thickness of their walls was measured which will later be used for verification of computational models. In general the work presented in this chapter sets a background needed for computational models that are presented in later chapters.

Chapter 4. Hyperelastic model

In the first section of this chapter some basic quantities from continuum mechanic are introduced. They are needed to describe the equations of motion, the pressure loading and hyperelastic constitutive equations in general. It is also convenient to include here quantities which describe the rate of deformation which are needed in the next chapter when an elasto-plastic constitutive model is described and used.

In the second section of this chapter an axisymmetric membrane model is described. This model was chosen to simulate the sheet deformation during the thermoforming process. Hyperelastic constitutive models and in particular a modification of an Ogden form which takes account of moisture content and temperature are also described. This is followed by a description of the computational model and a comparison of the computational and experimental results. Discussion of the results is presented in the last subsection.

4.1 Background of continuum mechanics

Much of the material presented here can be found in (Ogden, 1997a; Spencer, 1980a; Akin, 1994; Atkin & Fox, 1980a; Drozdov, 1996; Dunne & Petrinic, 2005a)

4.1.1 Motion and deformation

We are concerned here with a motion and deformation of a continuous body $\mathcal{B}$ assembled from particles, which in some configuration correspond to region $\mathcal{R}$ of Euclidean point space ε. At reference time $t_0 = 0$ each particle of the body $\mathcal{B}$ corresponds to a point of a region $\mathcal{R}_o$. This is the reference configuration of the body $\mathcal{B}$. Let O be a fixed origin of a rectangular coordinate system in ε and $\mathbf{X}$ be a position vector, relative to O, of a point $\mathcal{P}_o$ in the region $\mathcal{R}_o$, as shown in the Figure 4.1. Next we let the body $\mathcal{B}$ move from the region $\mathcal{R}_o$ to some new region $\mathcal{R}$, where at time t the position of its particles is described by a new position vector $\mathbf{x}$. This is the current

configuration, at time t, of the body. The motion of the body $\mathcal{B}$ can be described by specifying the dependence of positions $\mathbf{x}$ of the particles at time t on their positions $\mathbf{X}$ at time t_0, such that

$$\mathbf{x} = \mathbf{x}(\mathbf{X}, t) \quad \forall\, \mathbf{X} \in R_0 \quad \forall\, \mathbf{x} \in R \tag{4.1}$$

or in component form

$$x_i = x_i(X_R, t) \quad (i, R = 1, 2, 3). \tag{4.2}$$

The coordinates X_R of the particles of $\mathcal{B}$ are retained throughout the deformation and therefore are used as "labels" identifying each particle. However the coordinates x_i designate points of space and in general are occupied by different particles at different times t during the deformation. The coordinates X_R are termed material or Lagrangian coordinates and x_i are called spatial or Eulerian coordinates.
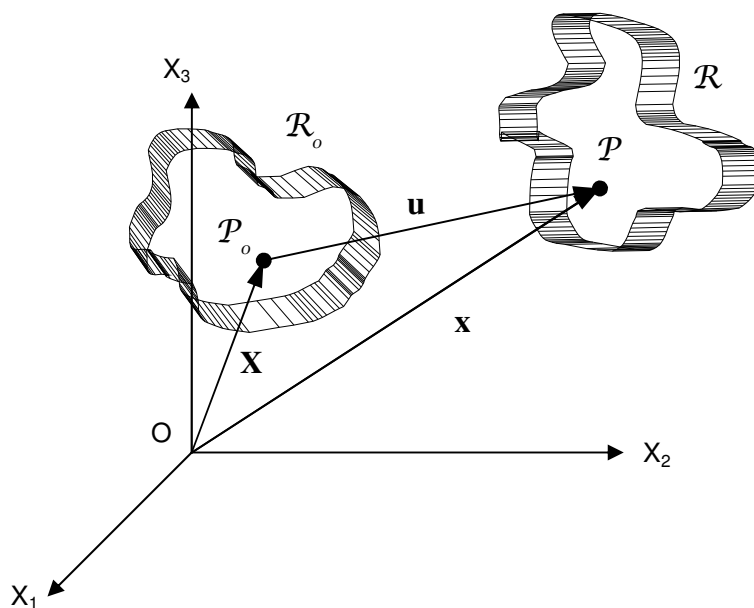
Figure 4.1. Reference and current configuration of particles of a body $\mathcal{B}$

The displacement vector $\mathbf{u}$ in material description is as follows

$$\mathbf{u}(\mathbf{X}, t) = \mathbf{x}(\mathbf{X}, t) - \mathbf{X} \tag{4.3}$$

and in spatial description

$$\mathbf{u}(\mathbf{x},t) = \mathbf{x} - \mathbf{X}(\mathbf{x},t).\tag{4.4}$$

Motion where distances between particles of the body are preserved is called rigid body motion. In contrast, a motion causing change of shape of the body is called deformation.

Deformation of line element

We are concerned here with deformation of material line element (material fibre) d$\mathbf{X}$, which is a vector at the point $\mathbf{X}$ in the reference configuration of the body $\mathcal{B}$. Then at time t the point $\mathbf{X}$ moves to $\mathbf{x}$ and d$\mathbf{X}$ transforms to d$\mathbf{x}$. The components of the deformed material line element d$\mathbf{x}$ are given by

$$dx_i = \frac{\partial x_i(\mathbf{X},t)}{\partial X_R} dX_R\tag{4.5}$$

The quantities $\partial x_i / \partial X_R$ are components of the deformation gradient tensor $\mathbf{F}$, given by

$$F_{iR} = \frac{\partial x_i}{\partial X_R}\tag{4.6}$$

The deformation gradient tensor is non-singular tensor since for every deformation $\det \mathbf{F} \neq 0$. Deformation where $\det \mathbf{F} = 0$ is physically unrealistic, as there would be at least one material fibre whose length is reduced to zero after deformation (Ogden, 1997b). The relation between deformation gradient tensor and displacement gradients is given by

$$F_{iR} = \frac{\partial u_i}{\partial X_R} + \delta_{iR}\tag{4.7}$$

or in matrix notation

$$\mathbf{F} = \nabla\mathbf{u} + \mathbf{I}\tag{4.8}$$

Deformation of surface and volume element

Suppose that three non-coplanar line elements d$\mathbf{X}_1$, d$\mathbf{X}_2$, d$\mathbf{X}_3$ at point $\mathbf{X}$ in reference configuration deform to d$\mathbf{x}_1$, d$\mathbf{x}_2$, d$\mathbf{x}_3$, so that

$$d\mathbf{x}_i = \mathbf{F}d\mathbf{X}_i\tag{4.9}$$

Then surface element $d\mathbf{S} = d\mathbf{X}_1 \times d\mathbf{X}_2$ and volume element $dV = (d\mathbf{X}_1 \times d\mathbf{X}_2) \cdot d\mathbf{X}_3$ deform respectively to $d\mathbf{s} = d\mathbf{x}_1 \times d\mathbf{x}_2$ and $dv = (d\mathbf{x}_1 \times d\mathbf{x}_2) \cdot d\mathbf{x}_3$ as follows

$$d\mathbf{s} = (\det \mathbf{F}) \mathbf{F}^{-T} d\mathbf{S} \tag{4.10}$$

and

$$dv = (\det \mathbf{F}) dV \tag{4.11}$$

The volume dV of a parallelepiped defined by $d\mathbf{X}_i$, i=1,2,3 has to be positive and therefore it follows from (4.11) that $\det \mathbf{F} > 0$. Moreover for incompressible materials we have that

$$\frac{dv}{dV} = (\det \mathbf{F}) = 1 \tag{4.12}$$

4.1.2 Measures of deformation

A measure of deformation should have the property that it does not change when no deformation takes place; therefore it must be unchanged in a rigid body motion. The deformation gradient tensor does not have this property since for rigid-body rotation we have that

$$\mathbf{F} = \mathbf{R}(t) \tag{4.13}$$

where $\mathbf{R}(t)$ is a proper orthogonal tensor. Therefore, other measures of deformation have been introduced. First consider the right Cauchy-Green deformation tensor given by

$$\mathbf{C} = \mathbf{F}^T \mathbf{F} \tag{4.14}$$

Clearly, it has the required property for a measure of deformation, since for the rigid-body motion given by (4.13) we have that $\mathbf{C} = \mathbf{R}^T \mathbf{R} = \mathbf{I}$. Hence it retains a constant value throughout a rigid-body motion. The components C_{RS} of $\mathbf{C}$ are given by

$$C_{RS} = F_{iR} F_{iS} = \frac{\partial x_i}{\partial X_R} \frac{\partial x_i}{\partial X_S} \tag{4.15}$$

Here, and in other equations in this chapter, the usual tensor convention of summation is used and implied over any index which is repeated. From (4.15) it is obvious that $C_{RS} = C_{SR}$, so that $\mathbf{C}$ is a symmetric tensor.

Second important measure of deformation is the left Cauchy-Green deformation tensor defined by

$$\mathbf{B} = \mathbf{FF}^T,\tag{4.16}$$

or in component form

$$B_{ij} = \frac{\partial x_i}{\partial X_R}\frac{\partial x_j}{\partial X_R}\tag{4.17}$$

In order to see the significance of these measures of deformation we define $\mathbf{v}^*$ and $\mathbf{v}$ to be unit vectors in the direction of $d\mathbf{X}$ and $d\mathbf{x}$ respectively.
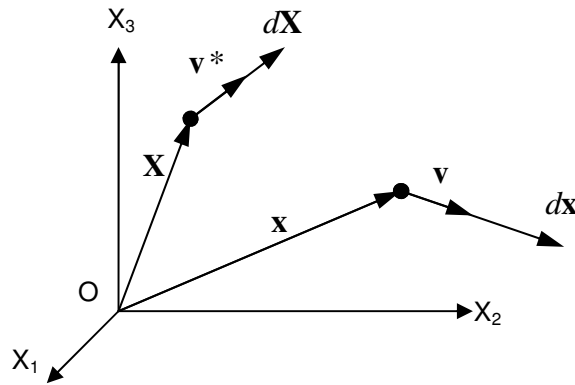
Figure 4.2. Extension of a material line element.

Then, from (4.5) we have

$$\mathbf{v}|d\mathbf{x}| = \mathbf{F}\mathbf{v}^*|d\mathbf{X}|\tag{4.18}$$

by squaring both sides we obtain

$$|d\mathbf{x}|^2 = \mathbf{v}^*\cdot(\mathbf{F}^T\mathbf{F}\mathbf{v}^*)|d\mathbf{X}|^2$$

and we can obtain the following

$$\lambda^2 = \frac{|d\mathbf{x}|^2}{|d\mathbf{X}|^2} = \mathbf{v}^*\cdot\left(\mathbf{C}\mathbf{v}^*\right),\tag{4.19}$$

where λ is called the stretch ratio of a line element. Thus knowledge of $\mathbf{C}$ allows us to calculate the stretch ratio of any line element. On the other hand knowledge of $\mathbf{B}$ or $\mathbf{B}^{-1}$ more specifically allows us to determine the local deformation in the neighbourhood of a point in the deformed configuration.

Polar decomposition of the deformation gradient tensor

Since the tensor $\mathbf{F}$ is non-singular it permits unique decompositions

$$\mathbf{F} = \mathbf{RU} = \mathbf{VR} \tag{4.20}$$

where $\mathbf{U}$ and $\mathbf{V}$ are positive-definite symmetric tensors and $\mathbf{R}$ is proper orthogonal tensor. The tensors $\mathbf{U}$ and $\mathbf{V}$ are called the right and left stretching tensors respectively and $\mathbf{R}$ is rotational tensor. To observe the physical significance of the decomposition (4.20) we write (4.5) in the form

$$dx_i = R_{iK} U_{KL} dX_L \tag{4.21}$$

or equivalently

$$dx_i = R_{iK} dy_K, \qquad dy_K = U_{KL} dX_L \tag{4.22}$$

From (4.22) we can split the deformation into two parts. First we have stretching of line elements dX_L into dy_K and then rigid-body rotation of dy_K into dx_i.

The relation between the Cauchy-Green deformation tensors and (4.20) is as follows

$$\mathbf{C} = \mathbf{F}^T \mathbf{F} = \mathbf{U}^T \mathbf{R}^T \mathbf{RU}$$

by use of the following property of proper orthogonal tensors

$$\mathbf{R}^T \mathbf{R} = \mathbf{I}$$

we have that

$$\mathbf{C} = \mathbf{U}^T \mathbf{U} = \mathbf{U}^2 \tag{4.23}$$

Similarly

$$\mathbf{B} = \mathbf{V}^2 \tag{4.24}$$

As it was already mentioned $\mathbf{U}$ is a positive-definite symmetric tensor and as such it possesses principal axes. When the coordinate axes coincide with the principal axes then $\mathbf{U}$ is diagonal and its components are the stretch ratios $\lambda_1, \lambda_2, \lambda_3$

$$\mathbf{U} = \begin{pmatrix} \lambda_1 & 0 & 0 \\ 0 & \lambda_2 & 0 \\ 0 & 0 & \lambda_3 \end{pmatrix}$$

The directions of principal axes of $\mathbf{U}$ can be found from (4.18) with use of (4.19) and (4.20). We then arrive at

$$\lambda \mathbf{v} = \mathbf{RUv}^* \tag{4.25}$$

assuming there is no rotation then $\mathbf{v} = \mathbf{v}^*$ and we have

$$\lambda \mathbf{v} = \mathbf{Uv} \tag{4.26}$$

or equivalently

$$(\mathbf{U} - \lambda\mathbf{I})\mathbf{v} = 0 \tag{4.27}$$

where $\mathbf{v}$ is an eigenvector of $\mathbf{U}$ and λ is its eigenvalue. The triad of eigenvectors v_i defines the principal axes of $\mathbf{U}$. From (4.23) we can see that $\mathbf{C} = \mathbf{U}^2$ and so the eigenvectors of $\mathbf{C}$ coincide with those of $\mathbf{U}$. Similarly from (4.24), the eigenvectors of $\mathbf{B}$ coincide with those of $\mathbf{V}$.

Principal invariants of the right and left Cauchy-Green deformation tensor

Principal invariants of $\mathbf{C}$ can be obtained from the characteristic equation for $\mathbf{C}$

$$\det(\mathbf{C} - \lambda\mathbf{I}) = 0$$

that is,

$$\lambda^3 - I_1\lambda^2 + I_2\lambda - I_3 = 0 \tag{4.28}$$

where

$$I_1 = C_{KK} = tr\mathbf{C}$$
$$I_2 = \frac{1}{2}(C_{KK}C_{LL} - C_{KL}C_{KL}) = \frac{1}{2}(tr\mathbf{C})^2 - \frac{1}{2}tr\mathbf{C}^2 \tag{4.29}$$
$$I_3 = \det\mathbf{C}$$

In terms of principal stretches they are expressed as follows

$$I_1 = \lambda_1^2 + \lambda_2^2 + \lambda_3^2$$
$$I_2 = \lambda_1^2\lambda_2^2 + \lambda_2^2\lambda_3^2 + \lambda_3^2\lambda_1^2 \tag{4.30}$$
$$I_3 = \lambda_1^2\lambda_2^2\lambda_3^2$$

Principal invariants of $\mathbf{B}$ are exactly the same as those for $\mathbf{C}$, even if their principal axes do not coincide. We can observe that

$$I_3 = \det\mathbf{C} = (\det\mathbf{F})^2 = \lambda_1^2\lambda_2^2\lambda_3^2 = (\frac{\partial v}{\partial V})^2 \tag{4.31}$$

From (4.31) it is obvious that for an incompressible material $I_3 = 1$ and

$$\lambda_1\lambda_2\lambda_3 = 1 \tag{4.32}$$

4.1.3 Material time derivative and mass balance

Before talking about mass balance it is convenient to introduce the material time derivative, which is actually not needed here but will be use in the next chapter.

Suppose that certain quantity Φ varies throughout a body in space and time. This means that Φ is a function of time and material or spatial coordinates, thus $\Phi = G(X_R, t) = g(x_i, t)$. We are interested in measuring the time derivative of Φ following a given particle X_R, that is $\dfrac{\partial G(X_R, t)}{\partial t}$ when the quantity is described in material coordinates. The material time derivative of Φ, which we choose to denote by $\dfrac{d\Phi}{dt}$ is given by

$$\frac{d\Phi}{dt} = \dot{\Phi} = \frac{\partial G(X_R, t)}{\partial t} \qquad (4.33)$$

When Φ is given in spatial description its time derivative is denoted by $\dfrac{\partial g(x_i, t)}{\partial t}$, which is a different quantity from $\dfrac{\partial G(X_R, t)}{\partial t}$, and it is necessary to express $\dfrac{d\Phi}{dt}$ by the derivatives of $g(x_i, t)$

$$\frac{d\Phi}{dt} = \frac{\partial g(x_i, t)}{\partial x_j} \frac{\partial x_j(X_R, t)}{\partial t} + \frac{\partial g(x_i, t)}{\partial t} \qquad (4.34)$$

observe that

$$\frac{\partial x_j(X_R, t)}{\partial t} = \dot{x}_j(X_R, t) \qquad (4.35)$$

where $\dot{x}_j(X_R, t)$ are velocity components of particles which initially occupied positions X_R. With use of (4.35) equation (4.34) can be given in the following form

$$\frac{d\Phi}{dt} = \frac{\partial g(x_i, t)}{\partial x_j} \dot{x}_j + \frac{\partial g(x_i, t)}{\partial t} \qquad (4.36)$$

or in the vector form

$$\frac{d\Phi}{dt} = \dot{\mathbf{x}} \cdot grad\ g(x_i, t) + \frac{\partial g(x_i, t)}{\partial t} \qquad (4.37)$$

Conservation of mass and continuity equation

Consider an arbitrary body $\mathcal{B}$ with volume $\mathcal{V}$ and surface S, fixed in space in relation to a fixed frame of reference, see Figure 4.3. The rate at which the mass of the body $\mathcal{B}$ increases is equal to the rate at which mass flows into volume $\mathcal{V}$ over surface S

$$\frac{\partial m}{\partial t} = \int_V \frac{\partial \rho}{\partial t} dV = -\int_S \rho \dot{x}_n dS \qquad (4.38)$$

where ρ is density of the body $\mathcal{B}$ and $\dot{x}_n$ is the normal component of velocity.
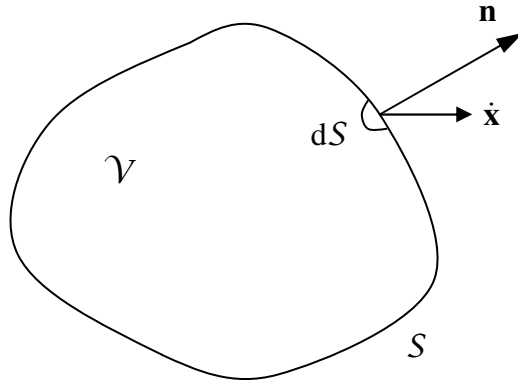
Figure 4.3. Flux through the surface of the body $\mathcal{B}$.

By applying the divergence theorem to (4.38) we have that

$$\int_V \left[\frac{\partial \rho}{\partial t} + div(\rho \dot{\mathbf{x}}) \right] dV = 0 \qquad (4.39)$$

Equation (4.39) hold everywhere throughout the body, hence

$$\frac{\partial \rho}{\partial t} + div(\rho \dot{\mathbf{x}}) = 0 \qquad (4.40)$$

or in component form

$$\frac{\partial \rho}{\partial t} + \dot{x}_i \frac{\partial \rho}{\partial x_i} + \rho \frac{\partial \dot{x}_i}{\partial x_i} = 0 \qquad (4.41)$$

which is the continuity equation. Using the material derivative

$$\frac{d\rho}{dt} = \frac{\partial \rho}{\partial t} + \dot{x}_i \frac{\partial \rho}{\partial x_i} \qquad (4.42)$$

we obtain another form of the continuity equation

$$\frac{d\rho}{dt} + \rho \frac{\partial \dot{x}_i}{\partial x_i} = 0 \qquad (4.43)$$

For incompressible material the density remains constant throughout the deformation, so that $\dfrac{d\rho}{dt} = 0$ and (4.43) takes the form

$$\frac{\partial \dot{x}_i}{\partial x_i} = 0 \ \text{ or } \ div\,\dot{\mathbf{x}} = 0 \tag{4.44}$$

which is the incompressibility condition.

4.1.4   Forces and conservation of linear and angular momentum

Consider the body $\mathcal{B}$ described in the previous subsection and assume that some external forces act on it. We can divide the forces exerted on the body into body forces and surface tractions. In general the body forces are forces per unit mass acting on particles of $\mathcal{B}$ and surface tractions are forces per unit area, acting on the surface S of the body, see the Figure 4.4. Good examples of body and traction forces are gravity force and pressure respectively.
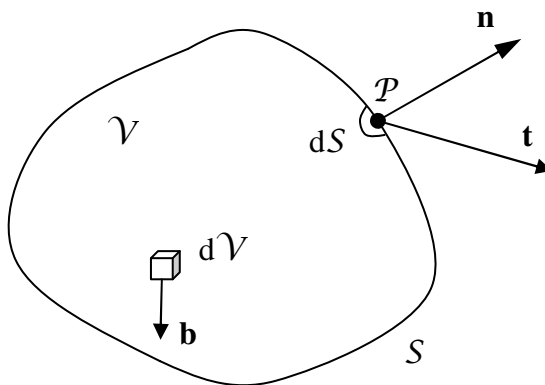
Figure 4.4. Body and traction forces

Then the resultant force acting on the body is of the form

$$\text{resultant force} = \int_V \rho\mathbf{b}dV + \int_S \mathbf{t}dS \tag{4.45}$$

and the total linear momentum of $\mathcal{B}$ is given by

$$\int_V \rho \dot{\mathbf{x}} dV \tag{4.46}$$

The rate of change of linear momentum of particles of body $\mathcal{B}$ is proportional to the resultant of the body forces $\mathbf{b}$ and the resultant of the surface tractions $\mathbf{t}$. Therefore we have the following

$$\frac{d}{dt}\int_V \rho \dot{\mathbf{x}} dV = \int_V \rho \mathbf{b} dV + \int_S \mathbf{t} dS \tag{4.47}$$

which is the equation of conservation of linear momentum.

Let $\mathbf{r}$ be a position vector from an arbitrary chosen origin, then the resultant moment acting on the body is defined by

$$\text{resultant moment} = \int_V \rho \mathbf{r} \times \mathbf{b} dV + \int_S \mathbf{r} \times \mathbf{t} dS \tag{4.48}$$

and the total angular momentum of $\mathcal{B}$ is given by

$$\int_V \rho \mathbf{r} \times \dot{\mathbf{x}} dV \tag{4.49}$$

Similar to conservation of linear momentum the conservation of angular momentum is defined such that the total angular momentum of particles of a body is proportional to the rate of change of resultant momentum of body and surface forces. This is given by the following

$$\frac{d}{dt}\int_V \rho \mathbf{r} \times \dot{\mathbf{x}} dV = \int_V \rho \mathbf{r} \times \mathbf{b} dV + \int_S \mathbf{r} \times \mathbf{t} dS \tag{4.50}$$

4.1.5 Cauchy and Piola stress tensors

In this section we are concerned with forces acting in the interior of the body $\mathcal{B}$. The surface traction $\mathbf{t}$, at point $\mathcal{P}$, acting on area element $\mathrm{d}S$, with unit normal $\mathbf{n}$, as seen in Figure 4.4, is transmitted from the outside to the inside of $\mathcal{B}$. A similar surface traction, equal in magnitude but opposite in direction to $\mathbf{t}$, is transmitted across the element with area $\mathrm{d}S$ from the inside to the outside of the body.

At point $\mathcal{P}$ there is a vector $\mathbf{t}$ associated with each direction through $\mathcal{P}$. In particular, given a system of rectangular coordinates system with base vectors $\mathbf{e}_i$, there is such a vector associated with the direction of each of the base vectors. Let $\mathbf{t}_1$ be the surface traction associated with the direction of $\mathbf{e}_1$, from the positive to the

negative side of the surface, as depicted in Figure 4.5. Surface tractions $\mathbf{t}_2$ and $\mathbf{t}_3$ are defined in a similar way.
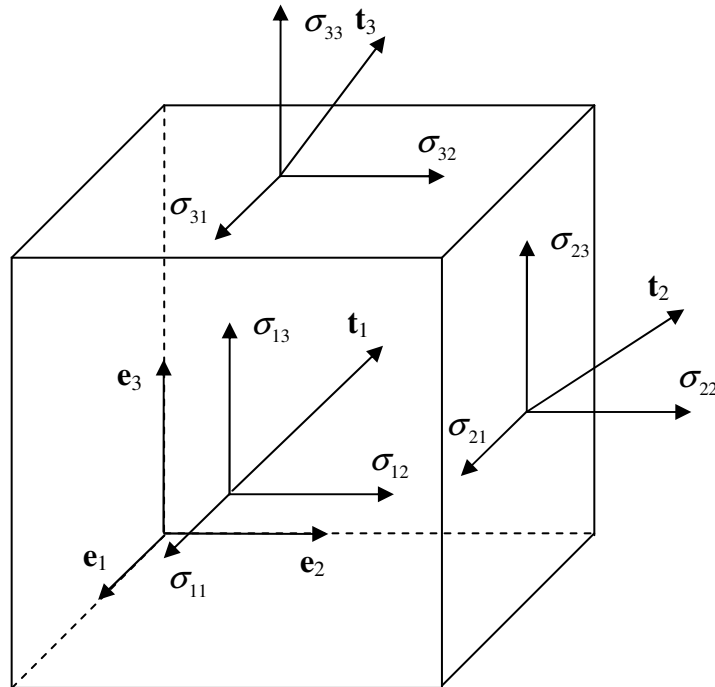
Figure 4.5. Components of traction forces on three faces of a unit cube.

We can now decompose the traction force $\mathbf{t}_i$, acting on the face, of a unit cube, with normal in the direction of $\mathbf{e}_i$ into three components σ_{ij}, j=1,2,3, as depicted on the Figure 4.5. This is expressed by the following equation

$$\mathbf{t}_i = \sigma_{ij}\mathbf{e}_j \quad \left(i, j = 1, 2, 3\right) \tag{4.51}$$

The quantities σ_{ij} form the components of a second-order tensor $\boldsymbol{\sigma}$ known as the Cauchy stress tensor

$$\boldsymbol{\sigma} = \begin{pmatrix} \sigma_{11} & \sigma_{12} & \sigma_{13} \\ \sigma_{21} & \sigma_{22} & \sigma_{23} \\ \sigma_{31} & \sigma_{32} & \sigma_{33} \end{pmatrix} \tag{4.52}$$

The components $\sigma_{ij}\left(i = j\right)$ are called normal stress components while the remaining components $\sigma_{ij}\left(i \neq j\right)$ are called shearing stress components. As it has been proven in the literature, see for example (Spencer, 1980b; Atkin & Fox, 1980b), the stress

tensor is symmetric $\sigma_{ij} = \sigma_{ji}$ and only six components need to be specified in the general case.

Nominal and Piola stress tensors

The Cauchy's stress tensor is defined in terms of the traction forces acting on a material surface which is specified in the current configuration. For some purposes it is more convenient to use stress tensor related to the reference configuration. Thus we introduce the first Piola stress tensor defined by

$$\mathbf{\Pi}^T = \mathbf{\sigma}(\det \mathbf{F})\mathbf{F}^{-T} \tag{4.53}$$

with components Π_{Ri} representing the components of forces in the x_i direction acting on a surface which is normal to the x_R-axis in the reference configuration, measured per unit surface area in the reference configuration. The nominal stress tensor is defined as the transpose of the Piola tensor

$$\mathbf{\Pi} = (\det \mathbf{F})\mathbf{F}^{-1}\mathbf{\sigma} \tag{4.54}$$

Since both the nominal and the first Piola stress tensors are not symmetric, we define the second Piola-Kirchhoff stress tensor by

$$\mathbf{S} = (\det \mathbf{F})\mathbf{F}^{-1}\mathbf{\sigma}\mathbf{F}^{-T} \tag{4.55}$$

which is related to $\mathbf{\Pi}$ by

$$\mathbf{\Pi}^T = \mathbf{F}\mathbf{S} \text{ or } \mathbf{S} = \mathbf{F}^{-1}\mathbf{\Pi}^T \tag{4.56}$$

4.1.6 Equations of motion and equilibrium

The equations of motion can be derived from the principle of conservation of linear momentum (4.47) and Cauchy's decomposition of surface tractions (4.51). After applying the divergence theorem to (4.47) we obtain

$$\int_V \left(\rho \frac{d\dot{x}_j}{dt} - \rho b_j - \frac{\partial \sigma_{ij}}{\partial x_i} \right) dV = 0 \tag{4.57}$$

and by dropping the integral sign and substituting for $\dfrac{d\dot{x}_j}{dt} = \ddot{x}_j$, which are components of acceleration vector $\ddot{\mathbf{x}}$, we arrive at

$$\frac{\partial \sigma_{ij}}{\partial x_i} + \rho b_j = \rho \ddot{x}_j \qquad (4.58)$$

which is the equation of motion.

In the case of static equilibrium we assume that there are no forces due to the body accelerating, and there are no inertia terms. This results in the following equations of equilibrium

$$\frac{\partial \sigma_{ij}}{\partial x_i} + \rho b_j = 0 \qquad (4.59)$$

Equation (4.59) is given in the current configuration and since in the current model quantities are related to the reference configuration the following equation of equilibrium in terms of the nominal stress tensor and the case where there are no body forces is given

$$\frac{\partial \Pi_{ij}}{\partial X_i} = 0 \qquad (4.60)$$

4.1.7 Deformation quantities in cylindrical polar coordinates

In previous sections the general equations of continuum mechanics in terms of cartesian coordinates were introduced. But due to the nature of the current problem, namely the symmetry about the z axis, cylindrical polar coordinates for description of the deformation quantities are used. Therefore the following way of deriving the main equations in terms of cylindrical polar coordinates is presented.

Observe that the relation between cartesian coordinates x_1, x_2, x_3 and cylindrical polar coordinates r, ϕ, z is given by

$$x_1 = r \cos \phi, \quad x_2 = r \sin \phi, \quad x_3 = z \qquad (4.61)$$

Transformation of a vector $\mathbf{x}$ with components x_1, x_2, x_3 in the cartesian coordinate system to x_r, x_ϕ, x_z in the cylindrical polar coordinate system can be performed by the following

$$x_r = x_1 \cos \phi + x_2 \sin \phi$$

$$x_\phi = -x_1 \sin \phi + x_2 \cos \phi$$

$$x_z = x_3$$

or using matrix notation

$$(x_r \ x_\phi \ x_z)^T = \mathbf{R}(x_1 \ x_2 \ x_3)^T, \quad (x_1 \ x_2 \ x_3)^T = \mathbf{R}^T(x_r \ x_\phi \ x_z)^T$$

where the matrix $\mathbf{R}$ is given by

$$\mathbf{R} = \begin{pmatrix} \cos\phi & \sin\phi & 0 \\ -\sin\phi & \cos\phi & 0 \\ 0 & 0 & 1 \end{pmatrix} \tag{4.62}$$

Now consider a finite deformation in which a typical particle which in the reference configuration has cylindrical polar coordinates R, Φ, Z moves to the position with cylindrical polar coordinates r, ϕ, z. The relation between cartesian and polar coordinates in the reference configuration can be given by (4.61) and in the current configuration by the following equations

$$x_1 = r\cos\phi, \quad x_2 = r\sin\phi, \quad x_3 = z \tag{4.63}$$

$$X_1 = R\cos\Phi, \quad X_2 = R\sin\Phi, \quad X_3 = Z \tag{4.64}$$

Then the motion of the particle is given by

$$r = r(R, \Phi, Z), \quad \phi = \phi(R, \Phi, Z), \quad z = z(R, \Phi, Z) \tag{4.65}$$

To perform the transformation of the deformation gradient tensor given in cartesian coordinates, defined by (4.6), to cylindrical polars we need to derive the gradients of mapping (4.64)

$$\frac{\partial}{\partial R} = \frac{\partial}{\partial X_1}\frac{\partial X_1}{\partial R} + \frac{\partial}{\partial X_2}\frac{\partial X_2}{\partial R} + \frac{\partial}{\partial X_3}\frac{\partial X_3}{\partial R} = \frac{\partial}{\partial X_1}\cos\Phi + \frac{\partial}{\partial X_2}\sin\Phi$$

$$\frac{\partial}{\partial \Phi} = \frac{\partial}{\partial X_1}\frac{\partial X_1}{\partial \Phi} + \frac{\partial}{\partial X_2}\frac{\partial X_2}{\partial \Phi} + \frac{\partial}{\partial X_3}\frac{\partial X_3}{\partial \Phi} = -\frac{\partial}{\partial X_1}R\sin\Phi + \frac{\partial}{\partial X_2}R\cos\Phi \tag{4.66}$$

$$\frac{\partial}{\partial Z} = \frac{\partial}{\partial X_1}\frac{\partial X_1}{\partial Z} + \frac{\partial}{\partial X_2}\frac{\partial X_2}{\partial Z} + \frac{\partial}{\partial X_3}\frac{\partial X_3}{\partial Z} = \frac{\partial}{\partial X_3}$$

From equations (4.66) we can define the following orthogonal matrix $\mathbf{P}$

$$\mathbf{P} = \begin{pmatrix} \cos\Phi & \sin\Phi & 0 \\ -\sin\Phi & \cos\Phi & 0 \\ 0 & 0 & 1 \end{pmatrix} \tag{4.67}$$

Using (4.63), (4.6), (4.67), and (4.66) we can obtain the following transformation of the deformation gradient tensor defined in cartesian coordinates to cylindrical polar coordinates

$$\mathbf{F}^* = \mathbf{R}\mathbf{F}\mathbf{P}^T = \begin{pmatrix} \dfrac{\partial r}{\partial R} & \dfrac{1}{R}\dfrac{\partial r}{\partial \Phi} & \dfrac{\partial r}{\partial Z} \\[2mm] r\dfrac{\partial \phi}{\partial R} & \dfrac{r}{R}\dfrac{\partial \phi}{\partial \Phi} & r\dfrac{\partial \phi}{\partial Z} \\[2mm] \dfrac{\partial z}{\partial R} & \dfrac{1}{R}\dfrac{\partial z}{\partial \Phi} & \dfrac{\partial z}{\partial Z} \end{pmatrix} \tag{4.68}$$

The right Cauchy-Green deformation tensor defined in cartesian coordinates by (4.14) can be expressed in cylindrical polar coordinates by the following

$$\mathbf{C}^* = \mathbf{P}\mathbf{C}\mathbf{P}^T = \mathbf{P}\mathbf{F}^T\mathbf{F}\mathbf{P}^T = \mathbf{P}\mathbf{F}^T\mathbf{R}^T\mathbf{R}\mathbf{F}\mathbf{P}^T = \mathbf{F}^{*T}\mathbf{F}^* \tag{4.69}$$

Similarly the left Cauchy-Green deformation tensor defined in cartesian coordinates by (4.16) can be transformed to cylindrical polar coordinates by the following

$$\mathbf{B}^* = \mathbf{R}\mathbf{B}\mathbf{R}^T = \mathbf{R}\mathbf{F}\mathbf{F}^T\mathbf{R}^T = \mathbf{R}\mathbf{F}\mathbf{P}^T\mathbf{P}\mathbf{F}^T\mathbf{R}^T = \mathbf{F}^*\mathbf{F}^{*T} \tag{4.70}$$

where we used the fact that $\mathbf{R}^T\mathbf{R} = \mathbf{I}, \mathbf{P}^T\mathbf{P} = \mathbf{I}$.

The relation between the stress tensor $\boldsymbol{\sigma}^*$ referred to cylindrical polar coordinates r, ϕ, z and the stress tensor $\boldsymbol{\sigma} = (\sigma_{ij})$ expressed in cartesian coordinates is as follows

$$\boldsymbol{\sigma}^* = \mathbf{R}\boldsymbol{\sigma}\mathbf{R}^T = \begin{pmatrix} \sigma_{rr} & \sigma_{r\phi} & \sigma_{rz} \\ \sigma_{\phi r} & \sigma_{\phi\phi} & \sigma_{\phi z} \\ \sigma_{zr} & \sigma_{z\phi} & \sigma_{zz} \end{pmatrix} \tag{4.71}$$

where the matrix $\mathbf{R}$ is given by (4.62).

4.2 Axisymmetric membrane model

In this section a membrane model of a thin sheet is described and the quantities used in a membrane model, such as the membrane deformation gradient, membrane stress and stretch are given. In the case of current mould and sheet geometry it is convenient to use an axisymmetric membrane model to describe the deformation process. The deformation that is obtained from a given loading is governed by the equations of quasi-static equilibrium which are given in terms of the nominal stress $\mathbf{\Pi}_m$, the components of which are related to the (tangential) principal stresses σ_1 and σ_2, with the material dependent part being concerned with how σ_1 and σ_2 are related to λ_1 and λ_2.

4.2.1 Description of membrane deformation

We are concerned here with a membrane of uniform thickness h_0 in the undeformed state. The membrane is assumed to be composed of homogenous, isotropic, incompressible material. In the membrane theory it is assumed that material fibers, which are normal to the membranes mid-surface, remain normal to the membranes mid-surface during the entire process of deformation, see the Figure 4.6.

Figure 4.6. Specific characteristic of a membrane deformation.

Moreover, the stress components in the direction of the normal are much smaller in magnitude than are the stress components in the tangential directions and therefore are assumed to be zero, i.e. $\boldsymbol{\sigma n} = 0$. This implies that in the membrane theory the deformation of the sheet can be described by quantities which just relate to the tangential directions (Green & Adkins, 1970).

Let (x_1, x_2, x_3) denote Cartesian coordinates and let (r, θ, x_3) denote cylindrical polar coordinates and with respect to cylindrical polars let the undeformed region be given by

$$\{(r,\theta,x_3): \quad 0 \leq r \leq 1, \quad -\pi \leq \theta < \pi, \quad |x_3| \leq h_0 / 2\} \tag{4.72}$$

where h_0 is the undeformed thickness. With an axisymmetric deformation we can omit the θ part here and describe the mid-surface deformation by

$$(r,0) \rightarrow (r+u_1,u_3) \tag{4.73}$$

where here $u_1=u_1(r)$ is the radial displacement and $u_3=u_3(r)$ is the vertical displacement, as illustrated on the Figure 4.7. However, the thickness of the membrane has to be taken into consideration. Hence, we have the following mapping

$$\mathbf{x}(r, x_3) = (r + u_1)\mathbf{e}_r + u_3\mathbf{e}_3 + \lambda x_3\mathbf{n} = (r + u_1 + \lambda x_3 n_1)\mathbf{e}_r + (u_3 + \lambda x_3 n_3)\mathbf{e}_3 \quad (4.74)$$

where $\mathbf{n} = (n_1(r), 0, n_3(r))^T$ denotes the unit normal vector on a deformed midpoint of the membrane. The factor $\lambda = \lambda(r)$ is the stretch ratio of material fibres, because even though the material fibres stay orthogonal to the membranes mid-surface throughout entire deformation, they can however change in length.
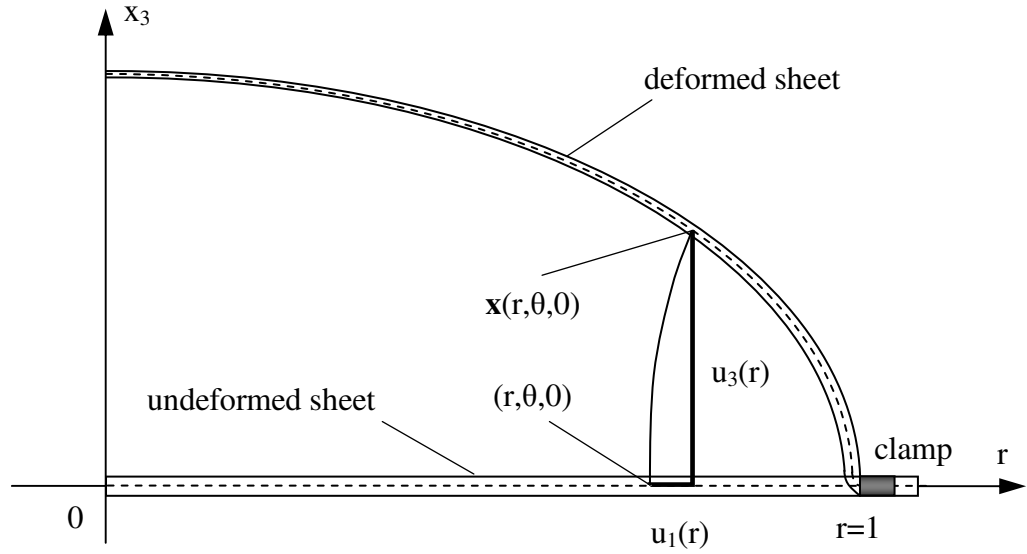
Figure 4.7. Sheet deformation sketch with deformation mapping of the mid-surface.

As spatial dependence is only on r it is convenient in what follows to use $'$ to denote differentiation with respect to r. The deformation gradient evaluated on the membranes mid-surface is given by

$$\mathbf{F} = (\mathbf{F}_m, \lambda_3 \mathbf{n}) = \begin{pmatrix} 1 + u_1' & 0 & \lambda_3 n_1 \\ 0 & 1 + \dfrac{u_1}{r} & 0 \\ u_3' & 0 & \lambda_3 n_3 \end{pmatrix} \quad (4.75)$$

where $\mathbf{F}_m$ denotes the first two columns, and the related right Cauchy Green tensor $\mathbf{C}_m$ in this case is as follows

$$\mathbf{C}_m = \mathbf{F}_m^T \mathbf{F}_m = \begin{pmatrix} (1 + u_1')^2 + (u_3')^2 & 0 \\ 0 & \left(1 + \dfrac{u_1}{r}\right)^2 \end{pmatrix} \quad (4.76)$$

From (4.23) we can see that the terms of $\mathbf{C}_m$ are squared principal stretches λ_1^2, λ_2^2, thus

$$\lambda_1 = \sqrt{\left(1+u_1'\right)^2 + \left(u_3'\right)^2}, \ \lambda_2 = \left(1+\frac{u_1}{r}\right) \tag{4.77}$$

They are associated respectively with the base directions $\mathbf{e}_r$ and $\mathbf{e}_\theta$ with respect to the undeformed configuration and the directions $\mathbf{t}$ and $\mathbf{e}_\theta$ with respect to the deformed configuration where $\mathbf{t}$ is a unit vector defined via the relation

$$\lambda_1 \mathbf{t} = \left(1+u_1', u_3'\right) \tag{4.78}$$

With this notation the unit vector $\mathbf{n}$ normal to the mid-surface is similarly defined via the relation

$$\lambda_1 \mathbf{n} = \left(-u_3', 1+u_1'\right) \tag{4.79}$$

To describe the stresses we note again that in a membrane approximation of how a thin sheet behaves it is assumed that

$$\boldsymbol{\sigma}\mathbf{n} = \mathbf{0} \tag{4.80}$$

where $\boldsymbol{\sigma}$ denotes the Cauchy stress tensor. With an axisymmetric deformation we also have that in the $\mathbf{e}_\theta$ direction

$$\boldsymbol{\sigma}\mathbf{e}_\theta = \sigma_2 \mathbf{e}_\theta \tag{4.81}$$

where σ_2 is a principal stress. These two conditions imply that the other direction of principal stress is $\mathbf{t}$ with

$$\boldsymbol{\sigma}\mathbf{t} = \sigma_1 \mathbf{t} \tag{4.82}$$

where σ_1 is the other principal stress. These last three relations imply that if we consider the polar decomposition of $\mathbf{F} = \mathbf{R}\mathbf{U}$ involving a proper orthogonal tensor $\mathbf{R}$ and a positive definite tensor $\mathbf{U}$ then we have

$$\mathbf{R}^T \boldsymbol{\sigma} \mathbf{R} = \begin{pmatrix} \sigma_1 & 0 & 0 \\ 0 & \sigma_2 & 0 \\ 0 & 0 & 0 \end{pmatrix} \tag{4.83}$$

Now the nominal stress for a three dimensional deformation is given by $\mathbf{\Pi} = \left(\det \mathbf{F}\right)\mathbf{F}^{-1}\boldsymbol{\sigma}$ and as $\det \mathbf{F} = 1$ in our case the first Piola stress $\mathbf{\Pi}^T$ is given by

$$\mathbf{\Pi}^T = \boldsymbol{\sigma}\mathbf{F}^{-T} = \boldsymbol{\sigma}\mathbf{R}\mathbf{U}^{-1} = \mathbf{R}\left(\mathbf{R}^T \boldsymbol{\sigma} \mathbf{R}\right)\mathbf{U}^{-1} = \left(\frac{\sigma_1}{\lambda_1}\mathbf{t}, \frac{\sigma_2}{\lambda_2}\mathbf{e}_\theta, \mathbf{0}\right) \tag{4.84}$$

Thus the connection between the components of the nominal stress and the principle Cauchy stresses is given by

$$\mathbf{\Pi}_m^T = \left(\frac{\sigma_1}{\lambda_1} \mathbf{t}, \frac{\sigma_2}{\lambda_2} \mathbf{e}_\theta \right) = \begin{pmatrix} \dfrac{(1+u_1')\sigma_1}{\lambda_1^2} & 0 \\ 0 & \dfrac{\sigma_2}{\lambda_2} \\ \dfrac{u_3'\sigma_1}{\lambda_1^2} & 0 \end{pmatrix} \tag{4.85}$$

4.2.2 Quasi-static equilibrium with pressure loading

The details for a membrane model of the thin sheet up to the point of first contact with the mould are given in a weak form as follows. We have that the displacement $\mathbf{u}$ is such that $u_1, u_3 \in H^1(0,1)$ satisfies the boundary conditions and axisymmetric condition and, for pressures $0 = P_0 < P_1 < P_2 < \cdots$ satisfies

$$a(\mathbf{u}, \mathbf{v}) - Pb(\mathbf{u}, \mathbf{v}) = 0 \quad \forall \mathbf{v} \in V, \quad P = P_j \tag{4.86}$$

where

$$V = \left\{ \mathbf{v} = (v_1, v_3)^T : v_1, v_3 \in H^1(0,1), v_1(0) = v_1(1) = v_3(1) = 0 \right\} \tag{4.87}$$

and where in our axisymmetric case

$$a(\mathbf{u}, \mathbf{v}) = h_0 \int_0^1 \left(\mathbf{\Pi}_m^T : \nabla \mathbf{v} \right) r \, dr = h_0 \int_0^1 \left(\frac{(1+u_1')\sigma_1 v_1'}{\lambda_1^2} + \frac{\sigma_2 v_1}{r \lambda_2} + \frac{u_3'\sigma_1 v_3'}{\lambda_1^2} \right) r \, dr \tag{4.88}$$

where : denotes the double dot-product operation (i.e. $A : B := tr(A^T B)$) and

$$\nabla \mathbf{v} = \begin{pmatrix} v_1' & 0 \\ 0 & \dfrac{v_1}{r} \\ v_3' & 0 \end{pmatrix}$$

and

$$b(\mathbf{u}, \mathbf{v}) = \int_0^1 \mathbf{v} \cdot (\mathbf{f}_1 \times \mathbf{f}_2) r \, dr = \int_0^1 (r + u_1)(-u_3' v_1 + (1 + u_1') v_3) \, dr \tag{4.89}$$

where $\mathbf{f}_1$ and $\mathbf{f}_2$ are the first two columns of $\mathbf{F}_m$. It can also be shown that the integrand in (4.89) can be written as $\lambda_1 \lambda_2 \mathbf{n} \cdot \mathbf{v}$. The pressure forcing action term

depends on the displacement **u** as it is a force described with respect to the deformed sheet.

4.3 Hyperelastic constitutive models for isotropic material

To complete the description of the mathematical model we need constitutive equations specific to the materials being used which connect the stresses σ_1 and σ_2 with the stretches λ_1 and λ_2. From the material tests described in Chapter 3 it appears that the behaviour of the material does not depend very much on the rate at which it is deformed at the temperatures that are used and thus a viscoelastic model is not needed. It should also be noted that in the implementation of thermoforming that is being considered here the loading is continually increased and thus there is no unloading. With these two observations we are led to consider hyperelastic relations.

Hyperelastic models are based on the assumption that if e denotes the internal energy of the material, ρ is the density (which is constant for an incompressible material) and $W = \rho e$ denotes the strain energy density then W only depends on the current deformation and

$$\frac{dW}{dt} = \boldsymbol{\sigma} : \mathbf{D} \tag{4.90}$$

where $\mathbf{D} = \left(\mathbf{L} + \mathbf{L}^T \right)/2$ and where

$$\mathbf{L} = \dot{\mathbf{F}}\mathbf{F}^{-1} \tag{4.91}$$

In words this says that the rate of change in this energy is entirely accounted for by the rate of mechanical working by the stresses. In contrast, for non-elastic materials there are dissipation terms to also consider with related energy terms dependent also on the rate at which the material is deformed.

To indicate briefly how the condition (4.90) leads to the relation between the stress and the stretch in the membrane case we first note that

$$\mathbf{D} = \frac{1}{2}\left(\dot{\mathbf{F}}\mathbf{F}^{-1} + \mathbf{F}^{-T}\dot{\mathbf{F}}^{T} \right) \tag{4.92}$$

and with $\mathbf{C} = \mathbf{F}^T\mathbf{F}$ we observe that $\dot{\mathbf{C}}$ and $\mathbf{D}$ are related by

$$\dot{\mathbf{C}} = \dot{\mathbf{F}}^T\mathbf{F} + \mathbf{F}^T\dot{\mathbf{F}} = 2\mathbf{F}^T\mathbf{D}\mathbf{F}, \quad 2\mathbf{D} = \mathbf{F}^{-T}\dot{\mathbf{C}}\mathbf{F}^{-1}, \quad 2\mathbf{F}^T\mathbf{D}\mathbf{F}^{-T} = \dot{\mathbf{C}}\mathbf{C}^{-1} \tag{4.93}$$

As similar tensors have the same trace and the incompressibility condition $\det \mathbf{F} = 1$ implies that $tr(\mathbf{D}) = 0$ we hence also have that $tr(\dot{\mathbf{C}}\mathbf{C}^{-1}) = 0$. Thus

$$2\boldsymbol{\sigma}\mathbf{D} = \boldsymbol{\sigma}\mathbf{F}^{-T}\dot{\mathbf{C}}\mathbf{F}^{-1} \quad \text{is similar to } \mathbf{S}\dot{\mathbf{C}}, \quad \text{where } \mathbf{S} = \mathbf{F}^{-1}\boldsymbol{\sigma}\mathbf{F}^{-T} \qquad (4.94)$$

Recall that the tensor $\mathbf{S}$ is called the second Piola stress tensor that was given earlier in (4.56). Using (4.94) with (4.90) and assuming at the moment that $W = W(\mathbf{C})$ the chain rule of partial differentiation written in tensor form using the : operator gives

$$2\frac{\partial W}{\partial \mathbf{C}} : \dot{\mathbf{C}} = \mathbf{S} : \dot{\mathbf{C}} \qquad (4.95)$$

For this to be true for all deformations satisfying the incompressibility relation this implies that $\mathbf{S}$ and $\boldsymbol{\sigma}$ are of the form

$$\mathbf{S} = -p\mathbf{C}^{-1} + 2\frac{\partial W}{\partial \mathbf{C}}, \quad \boldsymbol{\sigma} = \mathbf{F}\mathbf{S}\mathbf{F}^{T} = -p\mathbf{I} + 2\mathbf{F}\frac{\partial W}{\partial \mathbf{C}}\mathbf{F}^{T} \qquad (4.96)$$

where p is known as the hydrostatic pressure which is usually not determined by the local deformation, and the derivative $\frac{\partial W}{\partial \mathbf{C}} = \left(\frac{\partial W}{\partial C_{ij}}\right)$ where $\frac{\partial W}{\partial C_{ij}}$ is a partial derivative of W considered as a function of all nine components $C_{11}, C_{12}, ..., C_{33}$ which is symmetric in that the same expression is obtained when C_{kl} and C_{lk} are swapped. In the case of an isotropic material we actually just have that $W(\mathbf{C}) = \tilde{W}(\lambda_1, \lambda_2, \lambda_3)$ and with appropriate meaning of the partial derivatives in each case we have

$$2\mathbf{F}\frac{\partial W}{\partial \mathbf{C}}\mathbf{F}^{T} = 2\mathbf{F}\left(\frac{\partial \tilde{W}}{\partial \lambda_1}\frac{\partial \lambda_1}{\partial \mathbf{C}} + \frac{\partial \tilde{W}}{\partial \lambda_2}\frac{\partial \lambda_2}{\partial \mathbf{C}} + \frac{\partial \tilde{W}}{\partial \lambda_3}\frac{\partial \lambda_3}{\partial \mathbf{C}}\right)\mathbf{F}^{T} \qquad (4.97)$$

If we let $\mathbf{c}_1, \mathbf{c}_2$ and $\mathbf{c}_3$ denote the eigenvectors of unit length of $\mathbf{C}$ which correspond respectively to the eigenvalues λ_1^2, λ_2^2 and λ_3^2 with similarly $\mathbf{b}_1, \mathbf{b}_2$ and $\mathbf{b}_3$ denoting the eigenvectors of $\mathbf{B} = \mathbf{F}\mathbf{F}^{T}$ then

$$\mathbf{C}\mathbf{c}_i = \lambda_i^2\mathbf{c}_i, \quad \mathbf{B}\mathbf{b}_i = \lambda_i^2\mathbf{b}_i, \quad \mathbf{F}\mathbf{c}_i = \lambda_i\mathbf{b}_i, \quad \mathbf{F}^{T}\mathbf{b}_i = \lambda_i\mathbf{c}_i \qquad (4.98)$$

As $\mathbf{c}_i$ is a unit vector we have

$$\lambda_i^2 = \mathbf{c}_i^{T}\mathbf{C}\mathbf{c}_i \text{ giving } 2\lambda_i\frac{\partial \lambda_i}{\partial \mathbf{C}} = \mathbf{c}_i\mathbf{c}_i^{T} \text{ and giving } 2\mathbf{F}\frac{\partial \lambda_i}{\partial \mathbf{C}}\mathbf{F}^{T} = \lambda_i\mathbf{b}_i\mathbf{b}_i^{T} \qquad (4.99)$$

Substituting (4.99) and (4.97) into (4.96) we obtain

$$\boldsymbol{\sigma} = -p\mathbf{I} + \lambda_1 \frac{\partial \tilde{W}}{\partial \lambda_1} \mathbf{b}_1 \mathbf{b}_1^T + \lambda_2 \frac{\partial \tilde{W}}{\partial \lambda_2} \mathbf{b}_2 \mathbf{b}_2^T + \lambda_3 \frac{\partial \tilde{W}}{\partial \lambda_3} \mathbf{b}_3 \mathbf{b}_3^T \qquad (4.100)$$

Now in the case of our membrane deformation the stretches λ_1, λ_2 and λ_3 relate to tangential directions with $\mathbf{c}_1, \mathbf{c}_2$ and $\mathbf{c}_3$ being these directions with respect to the undeformed mid-surface and with $\mathbf{b}_1, \mathbf{b}_2$ and $\mathbf{b}_3$ being the corresponding directions with respect to the deformed mid-surface. In the direction $\mathbf{n}$ normal to the sheet $\mathbf{b}_3 = \mathbf{n}$ and the membrane assumption implies that $\boldsymbol{\sigma}\mathbf{n} = \mathbf{0}$ giving

$$0 = \boldsymbol{\sigma}\mathbf{n} = \left(-p + \lambda_3 \frac{\partial \tilde{W}}{\partial \lambda_3} \right)\mathbf{n} \text{ and } p = \lambda_3 \frac{\partial \tilde{W}}{\partial \lambda_3} \qquad (4.101)$$

And in the case of an incompressible deformation $\lambda_3 = \lambda_1^{-1}\lambda_2^{-1}$. Now, let $\hat{W}(\lambda_1, \lambda_2) = \tilde{W}\left(\lambda_1, \lambda_2, \lambda_1^{-1}\lambda_2^{-1}\right)$ giving

$$\lambda_1 \frac{\partial \hat{W}}{\partial \lambda_1} = \lambda_1 \frac{\partial \tilde{W}}{\partial \lambda_1} - \lambda_1 \left(\frac{1}{\lambda_1^2 \lambda_2} \right) \frac{\partial \tilde{W}}{\partial \lambda_3} = \lambda_1 \frac{\partial \tilde{W}}{\partial \lambda_1} - \lambda_3 \frac{\partial \tilde{W}}{\partial \lambda_3} \qquad (4.102)$$

In the membrane case we obtain

$$\underset{\sim}{\boldsymbol{\sigma}} = -\lambda_3 \frac{\partial \tilde{W}}{\partial \lambda_3} \mathbf{I} + \lambda_1 \frac{\partial \tilde{W}}{\partial \lambda_1} \mathbf{b}_1 \mathbf{b}_1^T + \lambda_2 \frac{\partial \tilde{W}}{\partial \lambda_2} \mathbf{b}_2 \mathbf{b}_2^T + \lambda_3 \frac{\partial \tilde{W}}{\partial \lambda_3} \mathbf{b}_3 \mathbf{b}_3^T$$

Now $\mathbf{I} = \mathbf{b}_1 \mathbf{b}_1^T + \mathbf{b}_2 \mathbf{b}_2^T + \mathbf{b}_3 \mathbf{b}_3^T$ and $\boldsymbol{\sigma}$ in the isotropic incompressible membrane case is given by

$$\underset{\sim}{\boldsymbol{\sigma}} = \left(\lambda_1 \frac{\partial \tilde{W}}{\partial \lambda_1} - \lambda_3 \frac{\partial \tilde{W}}{\partial \lambda_3} \right)\mathbf{b}_1 \mathbf{b}_1^T + \left(\lambda_2 \frac{\partial \tilde{W}}{\partial \lambda_2} - \lambda_3 \frac{\partial \tilde{W}}{\partial \lambda_3} \right)\mathbf{b}_2 \mathbf{b}_2^T = \sigma_1 \mathbf{b}_1 \mathbf{b}_1^T + \sigma_2 \mathbf{b}_2 \mathbf{b}_2^T \quad (4.103)$$

where we used (4.102) and the following

$$\sigma_i = \lambda_i \frac{\partial \hat{W}}{\partial \lambda_i} \mathbf{b}_i \mathbf{b}_i^T, \ i = 1, 2 .$$

In the computational model we use an Ogden form for W (we drop $\wedge$ now) which involves a relation of the form

$$W = \sum_i \frac{C_i}{\alpha_i} \left(\lambda_1^{\alpha_i} + \lambda_2^{\alpha_i} + \lambda_1^{-\alpha_i} \lambda_2^{-\alpha_i} - 3 \right), \quad \frac{C_i}{\alpha_i} > 0 \qquad (4.104)$$

where C_i and α_i are constants. This form of the relation includes the neo-Hookean model $(M = 1, \alpha_1 = 2)$, the Mooney-Rivlin model $(M = 2, \alpha_1 = 2, \alpha_2 = -2)$ and the Jones-Treloer model which has 3 terms and is of the form

$$W = \frac{0.63}{1.3}\left(\lambda_1^{1.3} + \lambda_2^{1.3} + \lambda_1^{-1.3}\lambda_2^{-1.3} - 3\right) + \frac{0.01}{4}\left(\lambda_1^{4} + \lambda_2^{4} + \lambda_1^{-4}\lambda_2^{-4} - 3\right)$$
$$+ \frac{0.0122}{-2}\left(\lambda_1^{-2} + \lambda_2^{-2} + \lambda_1^{2}\lambda_2^{2} - 3\right) \tag{4.105}$$

The actual coefficients C_i and α_i in such models need to be determined by material testing.

4.4 Consideration of moisture content in the constitutive equation

The difference between starch–based bioplastics and conventional polymers is the dependence of their properties on moisture content. This leads to the necessity of introducing moisture content into the constitutive equation in addition to the temperature dependence as shown in Figure 3.3. Most of the stress-strain curves in Figure 3.3 are typical of an elasto-plastic material in having an elastic region (the first linear part) followed by a plastic region in which the slope of the curve is small. Other tests, not reported here, involving unloading show permanent plastic deformation after unloading. However, as already mentioned, the pressure forcing action does not lead to any unloading and thus unloading doesn't have to be considered in this application and hence for the purpose of investigation of moisture content effect a hyperelastic model is considered to be sufficient. The particular model, which incorporates moisture dependence, is based on the following assumptions

- the moisture content effect in the plastic and elastic regions of the stress-strain relation is similar,
- the gradient of moisture content effect does not depend on temperature, but the moisture content (determined by the rate of loss) itself may depend on temperature.

A possible way of introducing moisture content and a temperature dependence into the constitutive model is to consider a strain energy function of the Ogden form

$$W = C\left(MC, T\right)\sum_{i=1}^{M}\frac{C_i\left(T\right)}{\alpha_i\left(T\right)}\left(\lambda_1^{\alpha_i(T)} + \lambda_2^{\alpha_i(T)} + \lambda_1^{-\alpha_i(T)}\lambda_2^{-\alpha_i(T)} - 3\right) \tag{4.106}$$

with coefficients which depend on the moisture content MC and the temperature T. Here the outer term $C(MC,T)$ is included in order to capture the effect of changes in moisture content and temperature. Based on the assumption that the moisture effect is similar at all strain levels the moisture dependence was deduced using the elastic region. From experimental curves obtained at room temperature $T_r = 23°C$, as shown in Figure 4.8, $C(MC,T_r)$ was normalised, so that when $MC = 15.52\%$, $C(MC,T_r) = 1$. Then $i = 1$ and $\alpha = -4$ was chosen in the equation (4.106) and W takes the following form

$$W = \frac{C(T)}{-4}\left(\lambda_1^{-4} + \lambda_2^{-4} + \lambda_1^4\lambda_2^4 - 3\right)$$

(4.107)

To find the remaining constant $C(T)$ observe that for uniaxial tensile test $\lambda_2 = \lambda_3$ and from (4.32), (4.101) and (4.107) we have

$$\sigma_1 = C(T)\left(\lambda_1^{-4} - \lambda_1^2\right)$$

(4.108)

Fitting (4.108) to the lowest curve of Figure 4.8 $C(T) = -172.18$ was obtained and the equation for tensile stress is given by

$$\sigma_1 = 172.18\left(\lambda_1^2 - \lambda_1^{-4}\right)$$

(4.109)

Multiplying this equation by $C(MC,T_r)$ and fitting to the remaining experimental curves values of $C(MC,T_r)$ at different moisture contents were obtained.
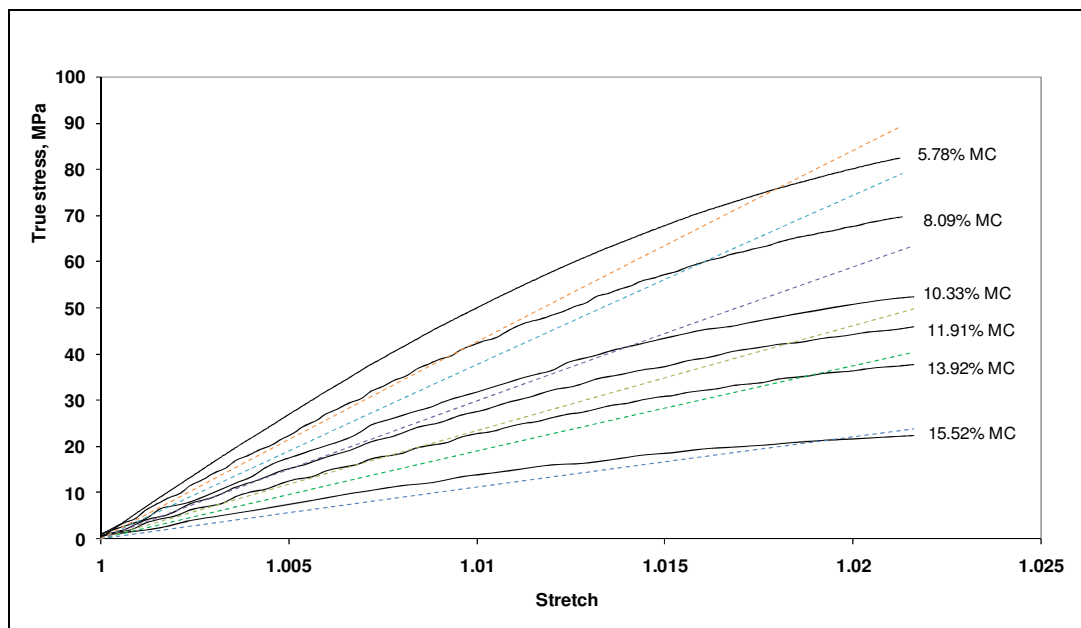
Figure 4.8. Elastic region of experimental curves (solid lines) with least square fits (dashed lines).

Figure 4.8 shows the elastic region of the experimental curves (solid lines) and the least square fits (dashed lines) that were obtained. A linear least square fit for obtained values of $C(MC, T_r)$ resulted in the following relation

$$C(MC, T_r) = 6.20 - 0.324MC \qquad (4.110)$$

as shown in Figure 4.9.
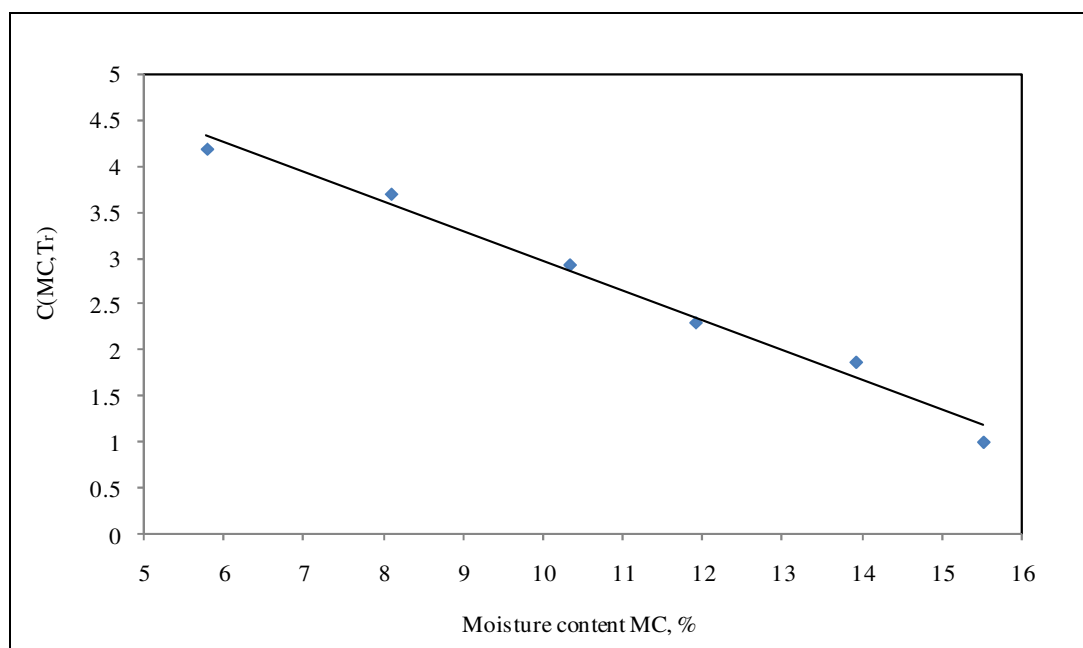
Figure 4.9. Obtained values of C(MC,T) and least square fit (solid line).

Using the assumption that the gradient of $C(MC,T)$ is independent of temperature variations, a strain-energy function for the Plantic® R1 material at other temperatures may be approximated by the following form

$$W = \left(-0.324MC + b(T)\right)\sum_{i=1}^{M}\frac{C_i(T)}{\alpha_i(T)}\left(\lambda_1^{\alpha_i(T)} + \lambda_2^{\alpha_i(T)} + \lambda_1^{-\alpha_i(T)}\lambda_2^{-\alpha_i(T)} - 3\right) \quad (4.111)$$

where $b(T)$, $C_i(T)$ and $\alpha_i(T)$ are constant at a given temperature T.

Since at any temperature moisture is escaping from the material, moisture content at a given time t can be deduced by solving the diffusion equation, in current case by (3.5). Values of moisture content put in (4.111) need to represent the moisture loss during tensile test only. This requires that moisture content after the heating stage needs to be calculated before starting the curve fitting. This is done with use of (3.5) where $t = 15s$ was set for heating time and $l = thickness / 2 = 0.21 \cdot 10^{-3} m$. The resultant moisture content change is depicted by the blue line in Figure 4.10.
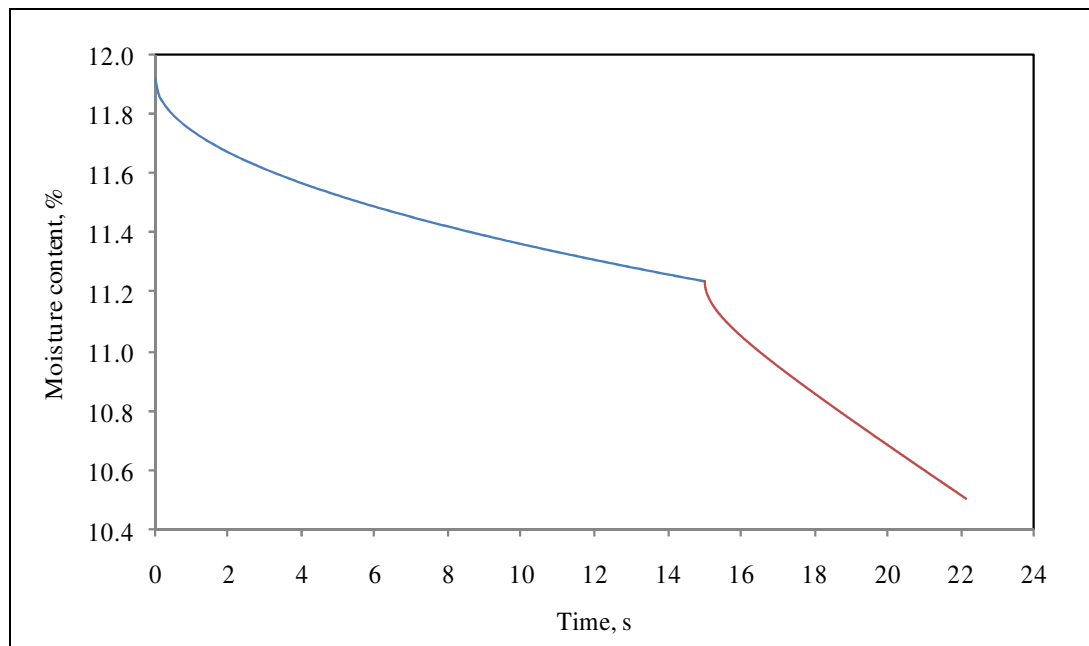
Figure 4.10. Calculated moisture loss during heating stage (blue line) and tensile test at crosshead speed of 500mm/min (red line).

The following red line denotes the moisture content change during tensile test and it was also calculated from (3.5) but this time l is calculated using (4.32) with $\lambda_2 = \lambda_3$ from the following

$$l = \frac{h_0}{2}\lambda_3 = \frac{h_0}{2}\lambda_1^{-0.5} \tag{4.112}$$

where h_0 is the initial thickness of the specimen. Equation (4.112) accounts for thickness change during tensile test and is the reason why the red line in Figure 4.10 has a greater slope than the blue line. In both cases the diffusion coefficient was taken to be constant and independent of concentration. Shrinkage effect was also omitted here.

For the constants $C_i(T)$ and $\alpha_i(T)$ in (4.111) the same α_i values as in the Jones-Treloer were used (i.e. $M = 3, \alpha_1 = 1.3, \alpha_1 = 4, \alpha_1 = -2$) and then $b(T), C_1(T), C_2(T), C_3(T)$ were determined by fitting to the experimental curves at 85°C at an initial moisture content of 11.91% and different cross-head speeds, i.e. the curves in Figure 3.5. See Figure 4.11 for a comparison of the experimental curves (solid lines) and the fits that this model gives (dashed lines). The fitting gives the following form of W

$$W = (-0.324MC + 3.80)\left[\begin{array}{l} \dfrac{2.91}{1.3}\left(\lambda_1^{1.3} + \lambda_2^{1.3} + \lambda_3^{1.3} - 3\right) + \dfrac{0.001}{4}\left(\lambda_1^4 + \lambda_2^4 + \lambda_3^4 - 3\right) \\ + \dfrac{-5.79}{-2}\left(\lambda_1^{-2} + \lambda_2^{-2} + \lambda_3^{-2} - 3\right) \end{array}\right] \tag{4.113}$$

This is the strain energy function which is used for the determination of the principal stresses σ_1 and σ_2 given by (4.101) for the $a(.,.)$ term given in (4.88).
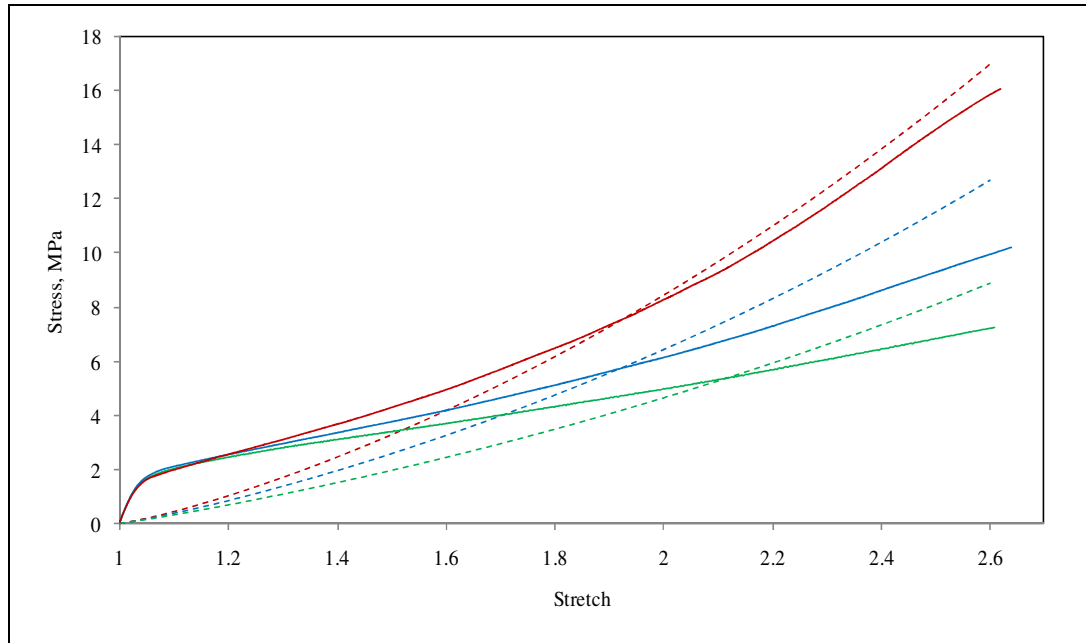
Figure 4.11. Experimental curves obtained at temperature of 85ºC, initial moisture content of 11.91% and different crosshead speeds (solid lines) and least square fits (dashed lines).

From Figure 4.12 we can observe the predicted effect of moisture loss on stress level. The solid green line presents least square fit to experimental curve at crosshead speed of 500mm/min, temperature of 85ºC, initial moisture content of 11.91% and the dashed line denotes hypothetical stress-stretch curve, which was obtained by keeping moisture content in (4.113) constant. Note that all of the dashed curves in Figure 4.11 originate from the dashed curve shown in Figure 4.12. This means that when omitting effect of rate of deformation and moisture loss the resultant stress-stretch curves at different crosshead speeds are identical.
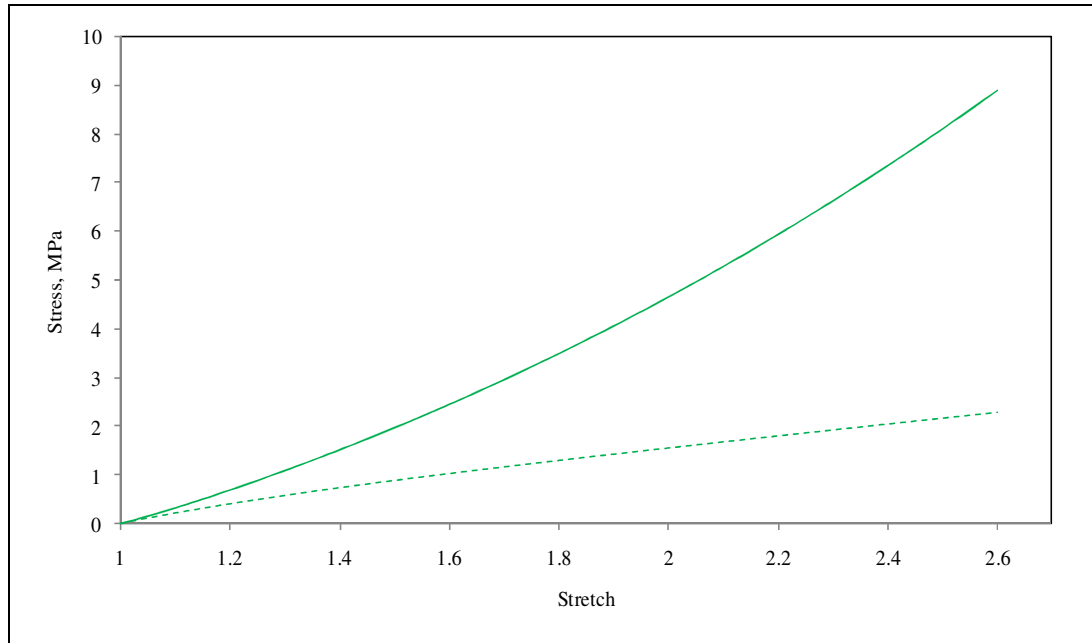
Figure 4.12. Least square fit (solid line) to experimental curve at crosshead speed of 500mm/min, temperature of 85ºC, initial moisture content of 11.91% and hypothetical curve obtained by keeping moisture content constant.

4.5 Inclusion of shrinkage in the model

As already discussed in section 3.6 Plantic® R1 shrinks on heating and this is caused by moisture escape from the material. In this section an attempt to account for this in the mathematical model is described. In the case of uniform shrinkage the deformation gradient tensor due to shrinkage is given by

$$\mathbf{F}_s = \begin{bmatrix} \lambda_s & 0 & 0 \\ 0 & \lambda_s & 0 \\ 0 & 0 & \lambda_s \end{bmatrix} \tag{4.114}$$

where

$$\lambda_s = 1 + \varepsilon_s \tag{4.115}$$

is the shrinkage stretch. ε_s in (4.115) is obtained from experimental measurements and in current case is given by (3.6).

Inclusion of shrinkage into uniaxial deformation

Simultaneous mechanical deformation and shrinkage is described on the example of uniaxial tensile test of a shrinking specimen, as schematically depicted on the Figure 4.13. It is assumed that this process can be modelled by assuming that the specimen first shrinks and then it is elongated with incompressibility assumption.
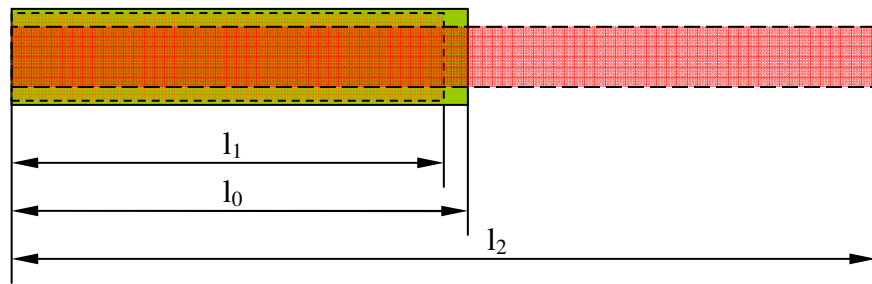
Figure 4.13. Uniaxial deformation of a shrinking specimen.

The principal stretches are given by

$$\lambda_s = \frac{l_1}{l_0}, \quad \lambda_{mech} = \frac{l_2}{l_1}, \quad \lambda = \frac{l_2}{l_0} \tag{4.116}$$

where λ_{mech} is the mechanical stretch and λ is the total stretch. The relation between the stretches is as follows

$$\lambda = \lambda_s \lambda_{mech} \tag{4.117}$$

It was assumed that the total deformation gradient can be decomposed into shrinkage and mechanical deformation gradients

$$\mathbf{F} = \mathbf{F}_s \mathbf{F}_{mech} = \mathbf{F}_{mech} \mathbf{F}_s = \lambda_s \mathbf{F}_{mech} \tag{4.118}$$

In the case of uniaxial deformation of incompressible material it is of the following form

$$\mathbf{F} = \begin{bmatrix} \lambda_s \lambda_{1,mech} & 0 & 0 \\ 0 & \lambda_s \lambda_{1,mech}^{-0.5} & 0 \\ 0 & 0 & \lambda_s \lambda_{1,mech}^{-0.5} \end{bmatrix} \tag{4.119}$$

To observe the effect of shrinkage on stress level note that the mechanical principal stretches should be put in (4.111) and the constants $b(T), C_i(T), \alpha_i(T)$ can be obtained by curve fitting to experimental data. The strain-energy function takes now the following form

$$W = (-0.324MC + 3.80) \begin{bmatrix} \dfrac{2.8}{1.3}\left(\left(\dfrac{\lambda_1}{\lambda_s}\right)^{1.3} + \left(\dfrac{\lambda_2}{\lambda_s}\right)^{1.3} + \left(\dfrac{\lambda_3}{\lambda_s}\right)^{1.3} - 3\right) \\ + \dfrac{0.001}{4}\left(\left(\dfrac{\lambda_1}{\lambda_s}\right)^{4} + \left(\dfrac{\lambda_2}{\lambda_s}\right)^{4} + \left(\dfrac{\lambda_3}{\lambda_s}\right)^{4} - 3\right) \\ + \dfrac{-5.5}{-2}\left(\left(\dfrac{\lambda_1}{\lambda_s}\right)^{-2} + \left(\dfrac{\lambda_2}{\lambda_s}\right)^{-2} + \left(\dfrac{\lambda_3}{\lambda_s}\right)^{-2} - 3\right) \end{bmatrix} \tag{4.120}$$

The calculated shrinkage effect on stress level during tensile test is presented in Figure 4.14.
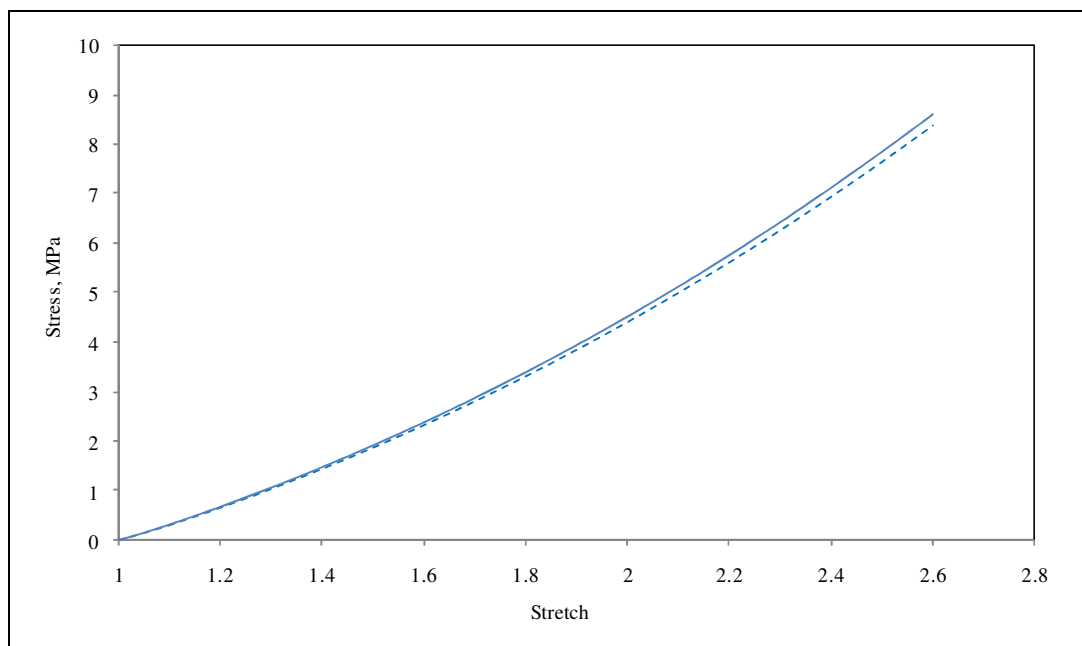
Figure 4.14. Predicted effect of shrinkage on stress. Solid line denotes results with shrinkage and dashed line without shrinkage for Plantic at temperature of 85ºC and 500mm/min crosshead speed.

Inclusion of shrinkage into membrane model

In the case of a membrane model the deformation gradient tensor is given by (4.75) and it is regarded as the total deformation gradient here. From (4.118) we can obtain the mechanical deformation gradient

$$\mathbf{F}_{mech} = \mathbf{F}_s^{-1}\mathbf{F} = \lambda_s^{-1}\mathbf{F} \tag{4.121}$$

The mechanical right Cauchy Green tensor in this case is given by the following

$$\mathbf{C}_{mech} = \mathbf{F}_{mech}^{T}\mathbf{F}_{mech} = \begin{bmatrix} \lambda_1^2\lambda_s^{-2} & 0 & 0 \\ 0 & \lambda_2^2\lambda_s^{-2} & 0 \\ 0 & 0 & \lambda_3^2\lambda_s^{-2} \end{bmatrix} \tag{4.122}$$

where λ_1, λ_2 are given by (4.77). From (4.122) the mechanical principal stretches can obtained

$$\lambda_{i,mech} = \lambda_i\lambda_s^{-1} \quad i = 1,2,3 \tag{4.123}$$

Using (4.123) and the material incompressibility condition $\lambda_{1,mech}\lambda_{2,mech}\lambda_{3,mech} = 1$ the total thickness ratio, i.e. the total third principal stretch λ_3 is given by

$$\lambda_3 = \frac{\lambda_s^3}{\lambda_1\lambda_2} \tag{4.124}$$

4.6 The computational model

The deformation that is obtained in thermoforming depends on the boundary conditions, the contact conditions when the sheet comes into contact with a mould together with an appropriate balancing of the forces resulting from the stresses with the forces as a result of the pressure loading. The computational model involves a straightforward one-dimensional finite element discretisation of the weak problem given by equations (4.86)-(4.89). The finite element method is based on two characteristic features. First a geometrically possibly complex domain of the problem is represented as a collection of non-overlapping sub-domains, not necessarily uniform, called the finite elements. These elements are of simple geometry. Second, the approximation over each element is a polynomial which is based on the idea that continuous functions can be accurately approximated by polynomials. The details of exactly how the method is implemented in any given situation depend on the

geometry of the elements and the degree or degrees of the polynomials used. A detailed description of this is contained in many different texts, see e.g. (Akin, 1994; Bathe, 1996; Reddy, 1984; Strang & Fix, 1973).

4.6.1 An overview of the discretisation

With the undeformed configuration of the mid-surface being $(r,0)$ and the pressure $P(t_j)$ being the pressure at time t_j we recall that the weak form is given by

$$a(\mathbf{u},\mathbf{v}) - Pb(\mathbf{u},\mathbf{v}) = 0 \quad \forall \mathbf{v} \in V, \quad P = P_j \tag{4.125}$$

where V is the space given by

$$V = \left\{ \mathbf{v} = (v_1, v_3)^T : v_1, v_3 \in H^1(0,1), v_1(0) = v_1(1) = v_3(1) = 0 \right\} \tag{4.126}$$

and in an axisymmetric case

$$a(\mathbf{u},\mathbf{v}) = h_0 \int_0^1 \left(\mathbf{\Pi}_m^T : \nabla \mathbf{v} \right) r \, dr = h_0 \int_0^1 \left(\frac{(1+u_1')\sigma_1 v_1'}{\lambda_1^2} + \frac{\sigma_2 v_1}{r\lambda_2} + \frac{u_3'\sigma_1 v_3'}{\lambda_1^2} \right) r \, dr \tag{4.127}$$

$$b(\mathbf{u},\mathbf{v}) = \int_0^1 \mathbf{v} \cdot (\mathbf{f}_1 \times \mathbf{f}_2) r \, dr = \int_0^1 (r + u_1)\left(-u_3' v_1 + (1+u_1') v_3 \right) dr \tag{4.128}$$

In this model the state of the body at time t_j at any point $(r,0)$ is hence described by $\mathbf{u} = (u_1(r), u_3(r))^T$ which is approximated by $\mathbf{u}_h = (u_{h1}(r), u_{h3}(r))^T$. Piecewise linear or piecewise quadratic elements are used here for both approximations to u_1 and u_3.

Piecewise linear elements

In the case of linear elements for the interval $[0,1]$ and an equidistant mesh of the form $0 = r_0 < r_1 < \cdots < r_{ne} = 1$, with mesh width $h = 1/ne$ involving ne elements and with $r_0, \cdots, r_{ne}$ denoting the nodal points, the discretised state of the body at time t_j is hence determined by the displacements $\mathbf{u}_h$ at these $ne+1$ nodal points on each of the ne elements. To describe $\mathbf{u}_h$ let $\hat{\Phi}_i \ (i = 0,1,...,ne)$ denote linear shape basis functions satisfying the condition

$$\hat{\Phi}_i(r_j) = \delta_{ij} \qquad (4.129)$$

as presented in Figure 4.15.
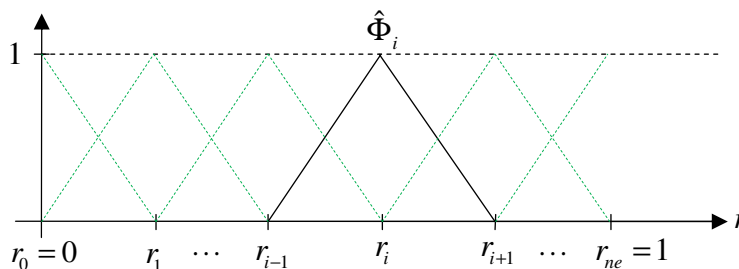
Figure 4.15. The approximation space for the finite element method with linear elements.

Using these functions we have at any given time t_j that $\mathbf{u}_h(r)$ can be written in the form

$$\mathbf{u}_h(r) = \sum_{i=0}^{ne} (\mathbf{u}_h)_i \hat{\Phi}_i(r) \qquad (4.130)$$

Piecewise quadratic elements

In the case of quadratics for the interval $[0,1]$ and an equidistant mesh of the form $0 = r_0 < r_1 < \cdots < r_{2ne} = 1$, with mesh width $h = 1/ne$ involving ne elements and with $r_0, \cdots, r_{2ne}$ denoting the nodal points, the discretised state of the body at time t_j is hence determined by the displacements $\mathbf{u}_h$ at these $2ne+1$ nodal points on each of the ne elements. Let $\hat{\Phi}_i$ $(i = 0, 1, ..., ne)$ denote quadratic shape basis functions satisfying the condition (4.129), see Figure 4.16.
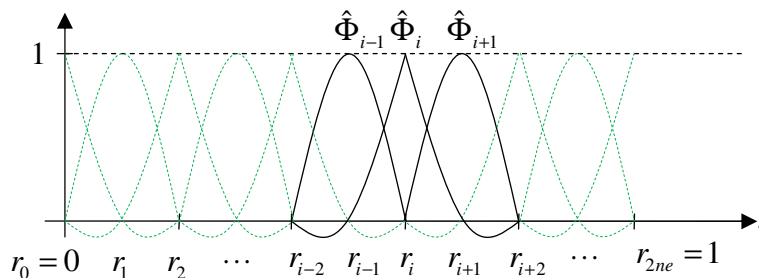
Figure 4.16. The approximation space for the finite element method with quadratic elements.

Using these functions we have at any given time t_j that $\mathbf{u}_h(r)$ can be written in the form

$$\mathbf{u}_h(r) = \sum_{i=0}^{2ne} (\mathbf{u}_h)_i \hat{\Phi}_i(r) \tag{4.131}$$

If we collect all the nodal values of $\mathbf{u}_h(r)_i$ into a vector $\mathbf{z}$ such that in the case of linear elements $\mathbf{z} = (u_{h1}(r_0), u_{h3}(r_0), \cdots, u_{h1}(r_i), u_{h3}(r_i), \cdots, u_{h1}(r_{ne}), u_{h3}(r_{ne}))^T$ or for quadratics $\mathbf{z} = (u_{h1}(r_0), u_{h3}(r_0), \cdots, u_{h1}(r_i), u_{h3}(r_i), \cdots, u_{h1}(r_{2ne}), u_{h3}(r_{2ne}))^T$ then (4.125) leads to a nonlinear system of equations in the form

$$\mathbf{f}(\mathbf{z}(P_j); P_j) = \mathbf{0} \tag{4.132}$$

which is solved using Newton's method

$$\mathbf{z}^{(n+1)} = \mathbf{z}^{(n)} - \left(J_f\left(\mathbf{z}^{(n)}; P_j\right)\right)^{-1} \mathbf{f}\left(\mathbf{z}^{(n)}; P_j\right), \quad n = 0, 1, 2, \cdots \tag{4.133}$$

where J_f denotes the Jacobian matrix associated with $\mathbf{f}$. For this to work we need a satisfactory starting vector $\mathbf{z}^{(0)}$ and at times t_j with $t_j > 1$ this is obtained from the solution $\mathbf{u}_h$ at the previous time t_{j-1}. If the iteration does not converge at time t_j then the time step is reduced with the 'failed' t_j replaced by $(t_{j-1} + t_j)/2$; i.e. we use a time closer to that which previously worked. Provided each nonlinear system has a solution and provided each Jacobian matrix $J_f(\mathbf{z}^{(n)}; P_j)$ is non-singular, this approach works well.

At the start of the computation at time t_1 some adjustments have to be made. When $P_0 = 0$, the sheet is flat and we know $\mathbf{u}_h$. If this sheet is pre-stretched corresponding to $u_{h1}(r)$ being non-zero then we can use this known state to construct $\mathbf{z}^{(0)}$. That is before the pressure is applied the displacement in the sheet is of the form

$$u_{h1}(r) = \beta r, \quad u_{h3}(r) = 0, \quad 0 \le r \le 1, \quad (\text{for some } \beta > 0)$$

The clamped boundary conditions are thus $u_{h1}(1) = \beta, u_{h3}(1) = 0$ and we also have the axisymmetric condition that $u_{h1}(0) = 0$. We set β to 0.1236 in current computations.

4.6.2 Calculations on element level

The calculations on the element level are presented as follows for the case of linear elements. The following coordinate transformation is used

$$r(\zeta) = \sum_{i=1}^{2} r_i \, \phi_i \, (\zeta) \tag{4.134}$$

to express the global coordinate r in terms of local coordinate ζ. r_i denotes the global coordinates of node i of the typical element $\Omega = (r_i, r_{i+1})$ and ϕ_i are the approximation functions on the interval $[0,1]$ of the standard element, see Figure 4.17.
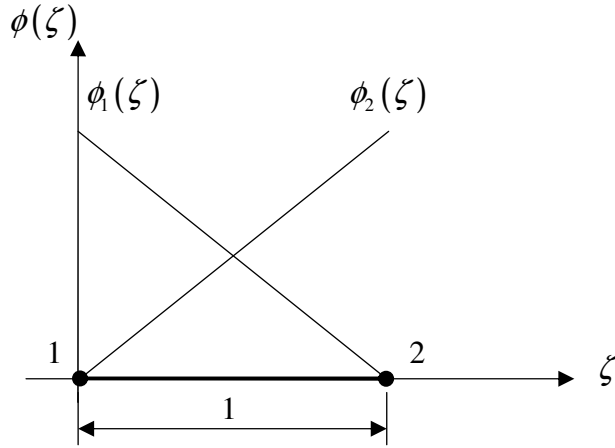
Figure 4.17. Standard linear element with unit length.

This form of transformation is used to form approximation $\mathbf{u}_h = \mathbf{u}_h(\zeta)$ on the standard element

$$\mathbf{u}_h(\zeta) = \sum_{i=1}^{2} (\mathbf{u}_h)_i \, \phi_i(\zeta) \tag{4.135}$$

The linear basis functions for the standard element on the interval $[0,1]$ are as follows

$$\phi_1(\zeta) = 1 - \zeta, \quad \phi_2(\zeta) = \zeta \tag{4.136}$$

and their derivatives

$$\frac{d\phi_1}{d\zeta} = -1 \quad \frac{d\phi_2}{d\zeta} = 1 \tag{4.137}$$

The derivative of $\phi_i(\zeta)$ with respect to the global coordinate r is given by

$$\frac{d\phi_i}{dr} = \frac{d\phi_i}{d\zeta}\frac{d\zeta}{dr} = \frac{d\phi_i}{d\zeta}J^{-1} \tag{4.138}$$

where $J = h$ is the Jacobian of transformation (4.134).

These basis functions were also chosen to obtain the test functions v_j in (4.127) and (4.128) on the standard element, thus $\left(v_j\right)_i = \phi_i$, where $j = 1,3$ and $i = 1,2$ is the node of the standard element.

If $\mathbf{u}_h(r_i)$ are displacements at the standard element node $i = 1,2$ then the following vector can be defined

$$\mathbf{z}^e = \left(u_{h1}(r_1), u_{h3}(r_1), u_{h1}(r_2), u_{h3}(r_2)\right)^T \in \mathbb{R}^4$$

which contains all the nodal displacement parameters. With this notation

$$\mathbf{u}_h^e(r) = \sum_{i=1}^{4}\left(\mathbf{z}^e\right)_i \mathbf{v}_i(r) \tag{4.139}$$

and the element vector $\mathbf{f}^e \in \mathbb{R}^4$, which is used to construct (4.132) is of the form

$$\mathbf{f}^e = a\left(\mathbf{u}_h^e, \mathbf{v}_i\right)_\Omega - Pb\left(\mathbf{u}_h^e, \mathbf{v}_i\right)_\Omega, \quad i = 1,...,4 \tag{4.140}$$

where $a\left(\mathbf{u}_h^e, \mathbf{v}_i\right)_\Omega$ and $b\left(\mathbf{u}_h^e, \mathbf{v}_i\right)_\Omega$ that the integrals are taken over the typical element $\Omega = (r_i, r_{i+1})$. Corresponding to the 4×1 vector $\mathbf{f}^e$ a 4×4 matrix J_h^e is also needed which contributes to the Jacobian matrix $J_h^e\left(\mathbf{z}(P_j); P_j\right)$, which is used to construct J_f in (4.132).

4.6.3 The contact algorithm and mould approximation

If the pressure increases linearly with the time t, i.e. $P = P_0 t$ (where P_0 is a constant), then the sheet inflates as t > 0 increases and at some time the sheet starts to come into contact with the mould. It is assumed that the sheet sticks on contact with the mould. With a mould cross-section of the form shown in the Figure 4.18 described parametrically by $(r, f(r))$, $0 \leq r \leq 1 + \text{prestretch}$, involving a union of

straight line segments and circular arcs it is straightforward to detect when a solution corresponds to a deformed membrane which has crossed the mould. Here $f(r)$ is the height and r is the radius.
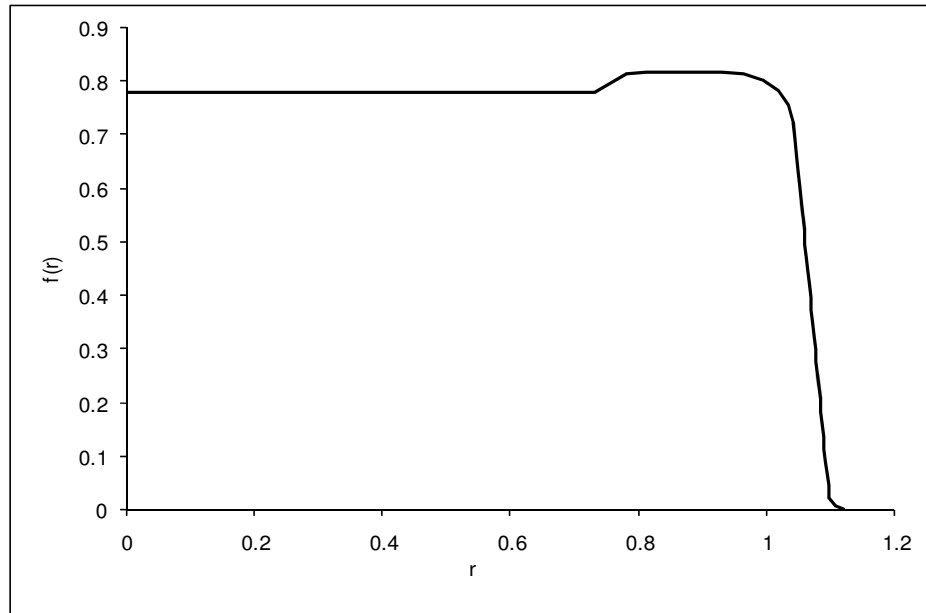
Figure 4.18. Approximated cross-section of the mould.

The original dimensions of the mould were normalised by division by the radius of the top inside edge, which is 39mm. The normalised dimensions were then multiplied by 1.1236 in order to "stretch" the mould to the pre-stretched radius of the sheet. This is because the sheet pre-stretch was set to this value. Then the mould cross-section is described by a set of functions of the form $\theta = \theta(r, f(r))$.

The contact detection algorithm is as follows:

- if $\quad u_3(r_k) - \theta\big(r_k + u_1(r_k), f\big(r_k + u_1(r_k)\big)\big) \geq 0 \quad$ then the point

  $\big(r_k + u_1(r_k), u_3(r_k)\big)$ is outside of the mould or on the mould,

- if $\quad u_3(r_k) - \theta\big(r_k + u_1(r_k), f\big(r_k + u_1(r_k)\big)\big) < 0 \quad$ then the point

  $\big(r_k + u_1(r_k), u_3(r_k)\big)$ is inside the mould.

If such a solution $\mathbf{z} = \mathbf{z}(t_j)$ is obtained at pressure $P(t_j)$ then for each deformed nodal point which is outside the mould linear interpolation involving the two solutions $\mathbf{z}(t_{j-1})$ and $\mathbf{z}(t_j)$ is used to estimate where contact of the node with the mould occurs and the node is "fixed" at that point on the mould. As the pressure further increases at this stage more and more of the sheet adheres to the mould. The equations (4.125)-(4.128) still apply with the modifications to the boundary conditions with in particular the region $\{r : 0 \leq r \leq 1\}$ being replaced by a subset of [0, 1] corresponding to the part of the sheet which has not yet made contact with the mould.

4.7 Comparison of thickness distribution and discussion

In this section computational results obtained from the hyperelastic model discussed in previous sections are presented. The computational model has been applied to the problem of the inflation of a sheet of the Plantic$^{\circledR}$ R1 material of thickness 0.42mm into an axisymmetric mould with cross section as shown in Figure 4.18. First, results of the computations with constant moisture content are discussed. Then results with moisture escaping from the material are presented and finally shrinkage and moisture loss during deformation are accounted for in our computations. The thickness ratio distribution obtained from the FE computations is compared with what is measured. Before the comparison the computed thickness ratio has to be corrected. This is because in this model pressure loading starts from a pre-stretched sheet and the initial thickness is reduced by $1/(1+\beta)^2$, where β is pre-stretch, thus the final thickness ratio is then corrected by $(1+\beta)^2$. Note that the measured thickness ratio presented in Figure 3.9 was obtained by averaging measurements taken from three thermoformed samples. The measured thickness was related to the initial sheet thickness, which did show some variation, although in the computations a uniform initial thickness was assumed.

4.7.1 Computations with constant moisture content

This section presents results of computations where moisture content in (4.113) was kept constant. That is it is assumed that no moisture loss or corresponding shrinkage were taken into account. There are no time dependent effects in this model and for the membrane model the deformation depends only on the ratio P/h_0, where P is the applied pressure and h_0 is the initial thickness. Linear finite elements with mesh consisting of $ne = 80$ elements was used.

The effect of moisture content on deformed shape during unconstrained deformation can be observed in Figure 4.19. The curves in Figure 4.19 represent deformed shapes after free inflation to one common pressure. As we can observe the deformed height of the sheet is gradually increasing with increase in the moisture content, that is softening of the material. Note that exactly the same shape and level of deformation can be obtained by varying pressure for sheets with different moisture content. This leads to the conclusion that in order to obtain a certain level of deformation of a dry sheet one would need to increase pressure during the thermoforming process. The dryer sheets will however break at lower strains than the softer moist sheets which limit the level of pressure that could be used in practice.

The comparison between computed and measured thickness distribution is presented in Figure 4.20. The computations were performed with moisture content of 11.91%. The comparison, although not perfect, captures the features of the thickness variation, showing that the thermoformed structure is thicker near the centre than near the corner region. The corner region is the thinnest part of the thermoformed structure. In Figure 4.21 the material particle paths predicted by the computational model are also shown.
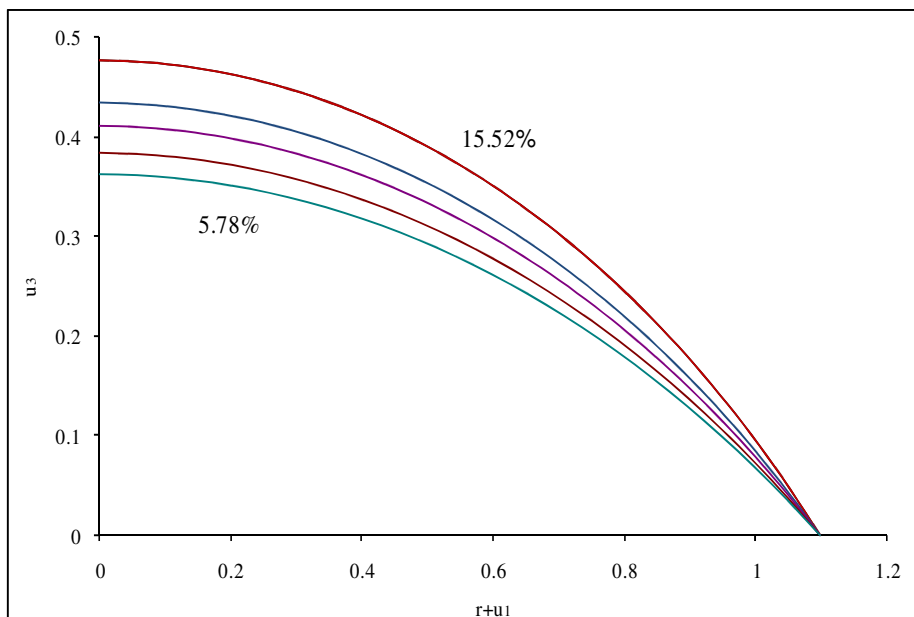
Figure 4.19. Free inflation results for different moisture content at one given pressure. The lowest curve corresponds to lowest moisture content and the top to highest.
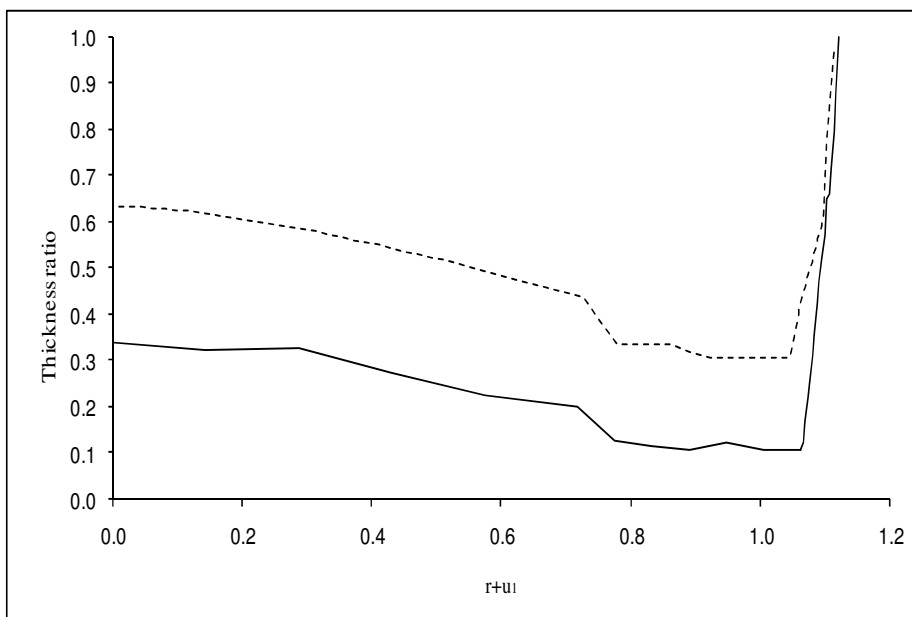
Figure 4.20. Thickness comparison between computational results without moisture loss (dashed line) and measurement results (solid line).
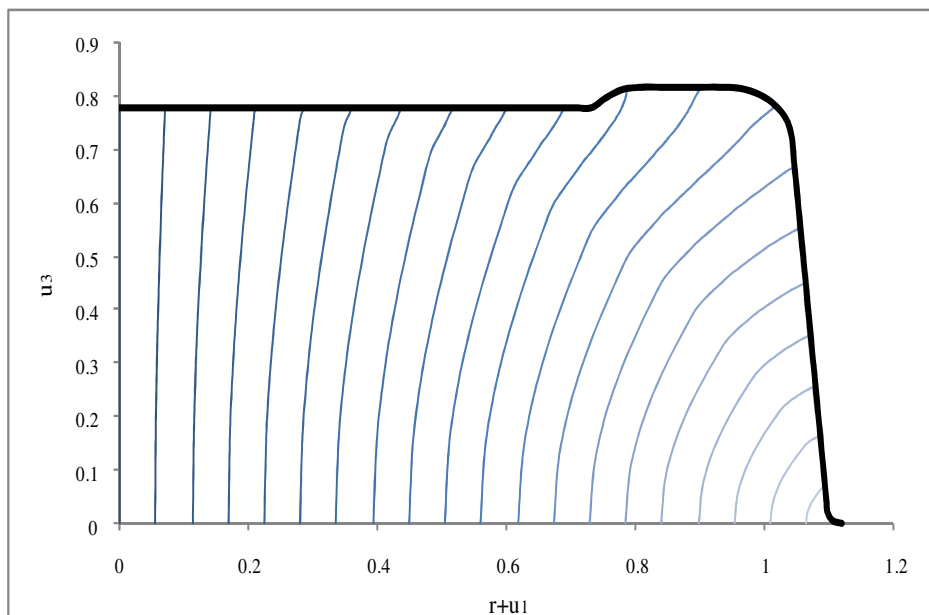
Figure 4.21. The prediction of the computational models of the material particle paths during the deformation.

4.7.2 Computations with moisture loss

In this section the results of computations with moisture loss due to evaporation from the sheet during the thermoforming process are presented. In this model an assumption was made that the sheet comes into full contact with the mould after 3 seconds. Although it wasn't possible to measure the exact time of the deformation during thermoforming trials, the 3 seconds time is close to the time observed experimentally. Because now moisture loss is accounted for, which is time dependent phenomenon, pressure is taken to be linearly dependent on time, $P = a \cdot t$, where a was selected such that after 3 seconds the deformation was finished.

An assumption is made that the moisture is escaping from the sheet until it comes into contact with the mould. This assumption is justified by the fact that when the sheet comes into contact with the mould it cools down rapidly and since temperature is the main reason for moisture loss it slows down moisture loss significantly. Further to that, contact with the mould builds a barrier which additionally limits moisture loss. Although this is idealised description, it is assumed to be sufficient for the current model.

Comparisons of thickness ratio are presented in Figure 4.22. The blue dashed line denotes thickness ratio computed with moisture escape during the deformation. Although there is some improvement compared to previous model with constant moisture content (red dashed line), the computed thickness ratio is still far from the experimental one, especially at the centre part. Inclusion of moisture loss in the model resulted in slight thinning of the sheet at the centre part and more at the shallow corners of the mould. This variation is due to the fact that moisture content distribution has now changed in the sheet. Initially uniform distribution of moisture in the sheet has been assumed, but as the time and deformation progresses the distribution changes. From equation (3.5) we know that not only time but also thickness affects moisture loss, thus the thinner the sheet the faster the loss. Calculated moisture distribution in the deformed sheet is presented in Figure 4.23 and the time at which the sheet came into contact with the mould is shown in Figure 4.24. The moisture distribution in the deformed sheet could be used for prediction of places of excessive embrittlement, which occurs with moisture loss.
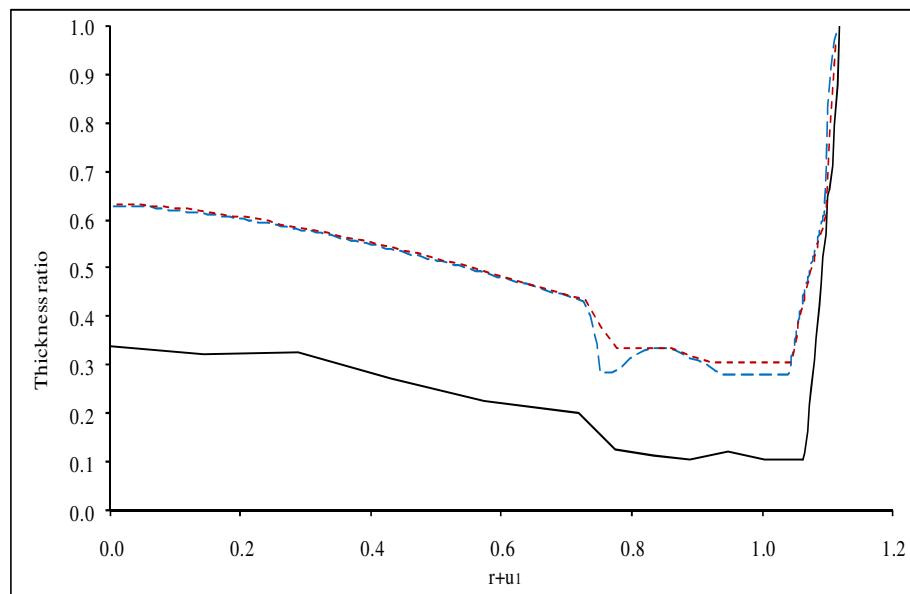
Figure 4.22. Thickness comparison between computational results with moisture loss (blue dashed line), without moisture loss (red dashed line) and measurement results (solid line).
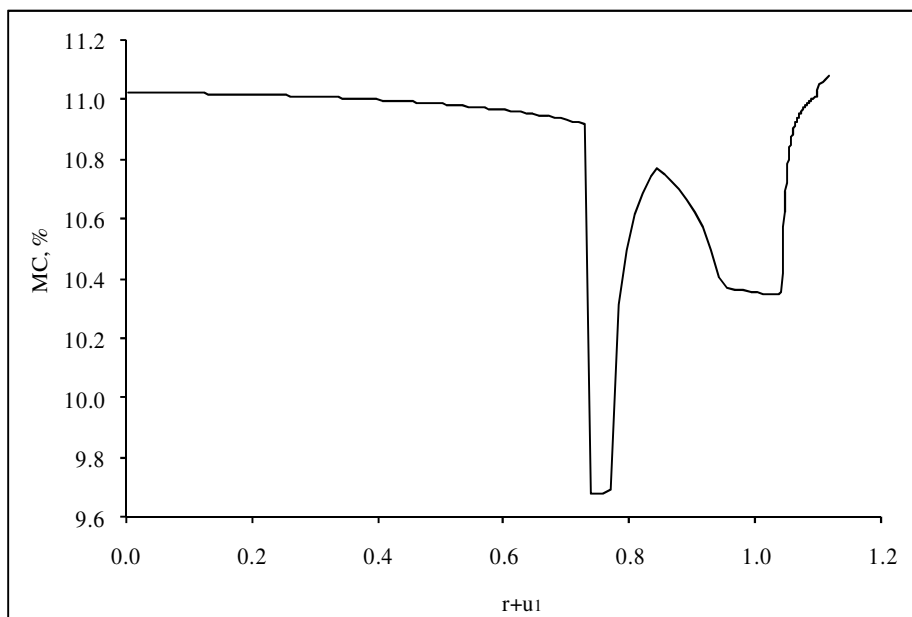
Figure 4.23. Predicted moisture distribution in deformed sheet.
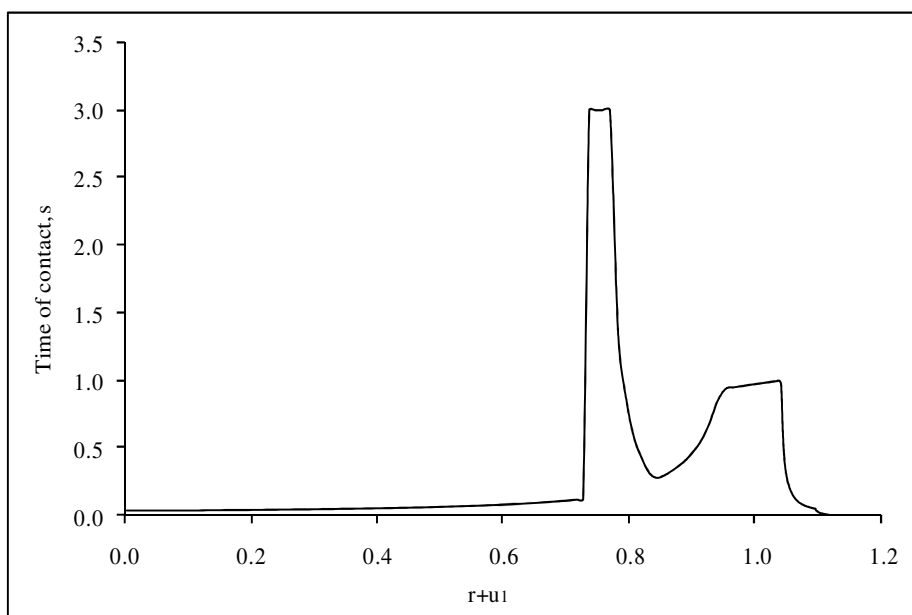
Figure 4.24. Predicted time of sheet contact with the mould.

4.7.3 Computations with moisture loss and shrinkage

The last computational model with hyperelastic strain-energy function involves moisture loss and shrinkage effects. The shrinkage effect discussed in

section 3.6 and 4.5 is the last phenomenon attributed with Plantic$^{®}$ R1 which is investigated here. This model uses the strain-energy function given in (4.120) with the total principal stretches being updated in each iteration by the shrinkage stretch from (4.123). Some other modifications compared to the previous model had to be made here. Because the shrinkage stretch depends on moisture loss, and with the previous assumption that moisture escapes from the sheet until contact is made with the mould, it follows that the sheet stops shrinking in the part that comes into contact with the mould. As previously, 3 seconds time for complete contact between the sheet and the mould is assumed.

The computational results in the form of a thickness comparison are presented in Figure 4.25, where the solid blue line denotes the calculated thickness ratio of the current model, the red dashed line denotes the calculated thickness ratio of the previous model and the black solid line denotes the measured thickness ratio. We can see that inclusion of shrinkage effect made little improvement over the previous model. The greatest difference is in the shallow corner part of the mould. This is because for this part of the sheet the time of contact was the highest and as a consequence more moisture was lost here than from the other parts of the sheet.
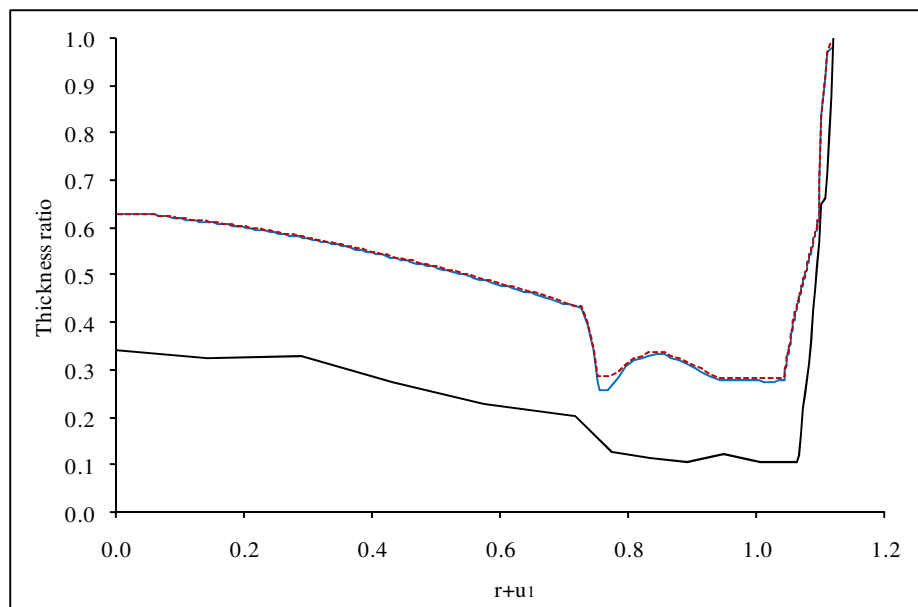
Figure 4.25. Thickness comparison between computational results with moisture loss and shrinkage (blue solid line), with only moisture loss (red dashed line) and measurement results (black solid line).

4.8 Comparison of hyperelastic and elasto-plastic models for free inflation

The computations reported in this chapter were based on the hyperelastic constitutive equation for the material description. The model was then modified to account for moisture loss and shrinkage. As it was shown in section 4.7 the computed thickness distribution is far from thickness obtained from experiments, although it is similar in shape. In order to improve this discrepancy a more accurate constitutive model has to be considered. A model that accounts for plastic flow, i.e. elasto-plastic model is considered next.

In this section a comparison between hyperelastic and elasto-plastic deformation for free inflation is made. The free inflation is an unconstrained deformation of a flat circular sheet of material and for this purpose, as previously, an axisymmetric model is chosen. Without going into much detail on elasto-plastic constitutive model, since it is discussed in next chapter, it is sufficient to say for now, that an elasto-plastic model with isotropic hardening is used. The parameters of this model, i.e. elastic modulus, yield stress and tangent modulus were found by fitting to experimental results at temperature of 85°C and cross-head speed of 500 mm/min. This is the same experimental curve as was used for hyperelastic model. For the comparison the shape and thickness ratio of deformed sheets is presented. The sheets were inflated to the height equal to their radius, see Figure 4.26 and Figure 4.27 respectively. As we can see the hyperelasic model produces more uniform thickness distribution comparing to elasto-plastic, which gives sharp change in thickness ratio from 1 at the corner to about 10 times less at the centre. The reason for this is elasto-plastic flow or yielding. We can also observe that the effect of Poisson's ratio is rather small. This is due to large range of plastic deformation comparing to elastic contribution in elasto-plastic deformation.
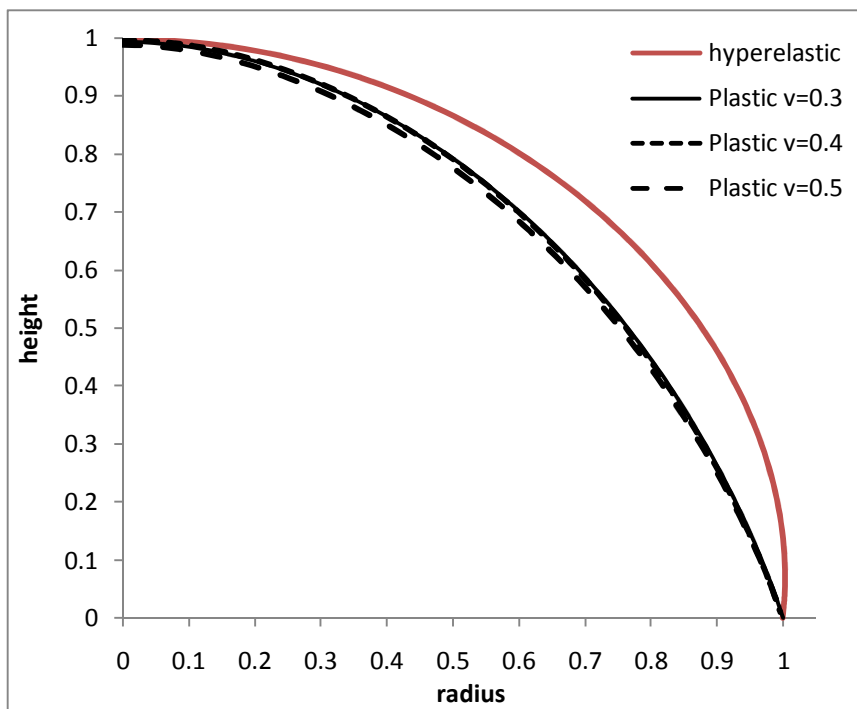
Figure 4.26. The deformed shape of inflated sheets for hyperelastic and elasto-plastic models with different Poisson's ratios.
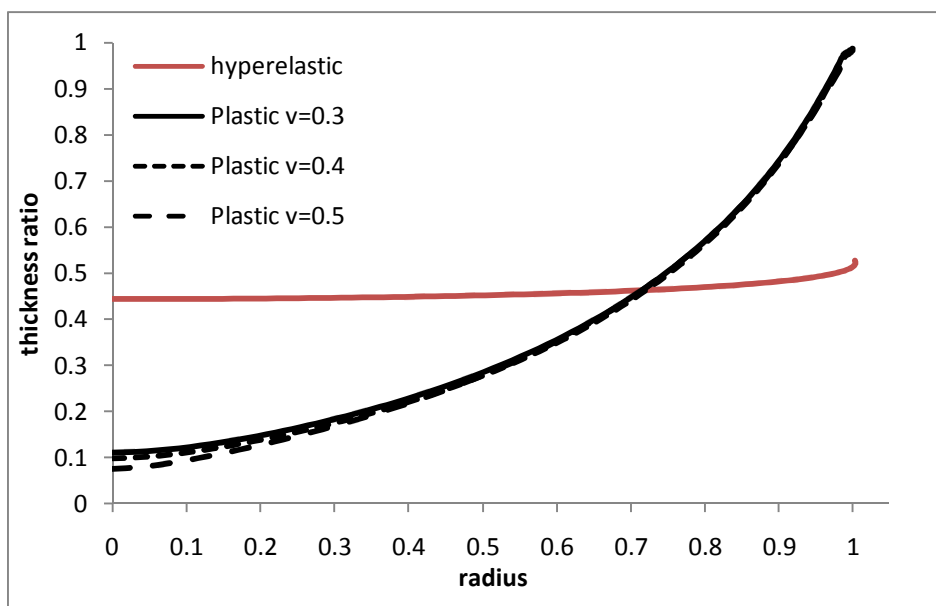
Figure 4.27. The thickness ratio of inflated sheets for hyperelastic and elasto-plastic models with different Poisson's ratios.

4.9 Summary

The computational model with hyperelastic constitutive equation was used to investigate the effect of moisture content, its loss and shrinkage effect. To verify the calculated results a comparison was made with experimental measurements in the form of the thickness distribution ratio. The present models show that moisture content affects mostly pressure values required to push a sheet into a mould, but there is little effect on the thickness distribution. Also inclusion of shrinkage in the model made little improvement in the results. To better observe thickness distribution and understand the deformation the results referred to the length of the cross-section of the mould are presented, see Figure 4.28. It can be seen that the model predicts thicker sheet at the centre bottom part and thinner at the wall. A similar pattern can be observed in comparison of hyperelastic with elasto-plastic deformation shown in section 4.8. This leads to a conclusion that use of the hyperelastic constitutive equation is responsible for the discrepancy between the results. The hyperelastic model does not account for yielding which is thought to be the cause of the discrepancy. Thus, the next chapter presents modeling with use of elasto-plastic constitutive equation.
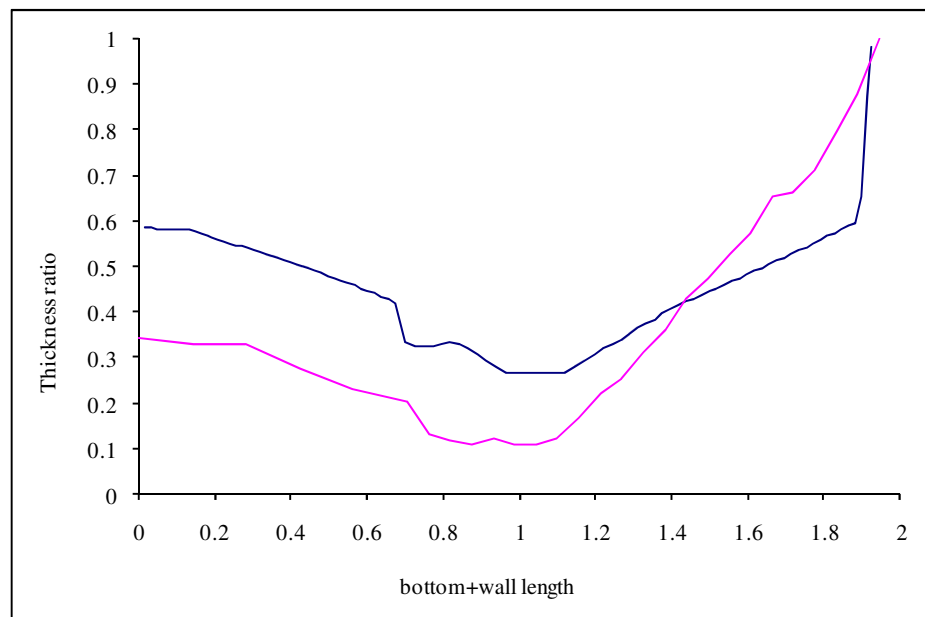
Figure 4.28. Thickness comparison between computational results without moisture loss (blue line) and measurement results (red line).

Chapter 5. Elasto-plastic model

In this chapter a description of modeling the thermoforming process of starch-based biopolymers with the use of an elasto-plastic constitutive model is presented. As a large deformation is considered here plasticity models are described in this context after introducing some background continuum plasticity under a small strain assumption. The discussion under the small strain assumption given in section 5.1 is used to more easily introduce the terminology of plasticity which is needed in later sections. Specifically, this section is focused mostly on an isotropic elasto-plastic model with von Mises yield criterion. The extension of the elasto-plastic coupling to large deformations, which is based on a multiplicative decomposition of the deformation gradient tensor, is then given in section 5.2 and this is followed by a discussion of the principle of material objectivity in section 5.3 as the large deformation constitutive relation needs to be expressed in terms which transform correctly when the frame of reference is changed. With the (finite) elasto-plastic constitutive model introduced the remainder of the chapter considers details of the three dimensional finite element model in section 5.4 followed by details of the implementation and the numerical results that are obtained. Specifically section 5.4 gives a description of a three dimensional solid model representing the finite deformation of an elasto-plastic sheet constrained by a rigid mould and then discuss how the model was built using ANSYS software and solved with the explicit dynamic solver of LS-DYNA in section 5.5. Finally, in section 5.6 the modeling results and a comparison of thickness distribution with that obtained experimentally is given.

5.1 Background continuum plasticity

This section provides an introduction to some fundamentals of time-independent small strain continuum plasticity which helps in the understanding of the finite strain which is described later. The selection of the material presented here is that which is needed for the thermoforming application, that is, multiaxial yield, normality hypothesis, consistency condition and isotropic hardening are given. For a broader description of continuum plasticity the reader is referred to (Dunne &

Petrinic, 2005a; Owen & Hinton, 1980a; Khan & Huang, 1995a; Hill, 1998). The decomposition of strain into elastic and plastic part is given first.

Additive decomposition of strain

The idealised stress-strain relation obtained from an uniaxial tensile test is shown in Figure 5.1. Initially the material deforms elastically, with slope E being elastic modulus, until yield stress σ_y is obtained. Plasticity commences when $\sigma \geq \sigma_y$, after which the material strain hardens. Hardening occurs when stress is increasing in relation to perfect plastic behaviour denoted with the dashed line. On unloading at a strain of ε the stress is decreasing linearly with strain such that the gradient of this part of the stress-strain curve is again Young's modulus E. After unloading the remaining strain in the test specimen is the plastic strain ε^p and the recovered strain is the elastic strain ε^e. The total strain ε is thus the sum of the two, i.e.

$$\varepsilon = \varepsilon^e + \varepsilon^p \tag{5.1}$$
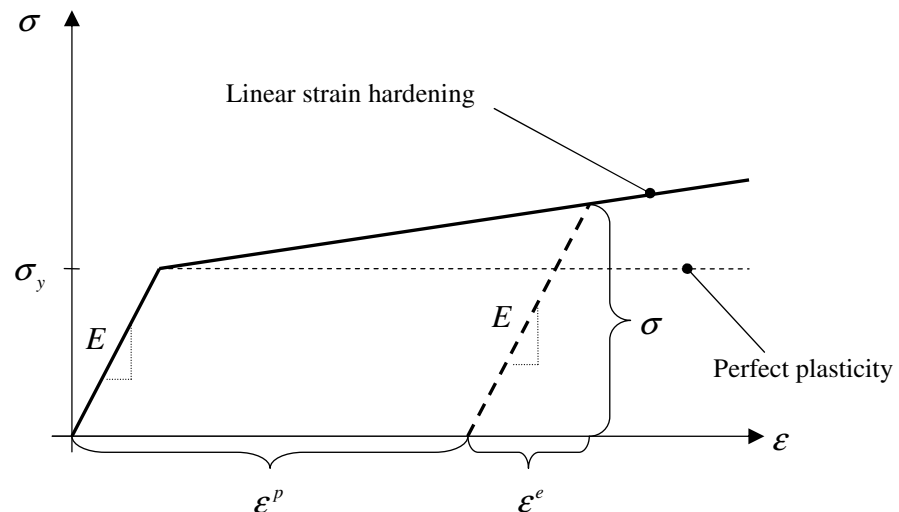
Figure 5.1. The classical decomposition of strain into elastic and plastic parts (Dunne & Petrinic, 2005b; Owen & Hinton, 1980b).

The stress achieved at a strain of ε is given by

$$\sigma = E\varepsilon^e = E\left(\varepsilon - \varepsilon^p\right) \tag{5.2}$$

Incompressibility condition

The incompressibility condition was first investigated by Bridgman who examined the material response to very high hydrostatic pressure. He performed tensile tests in the presence of hydrostatic pressure up to 24,000 atm. The experiments showed that the volume of the material does not change permanently even for large pressure; thus the material can be assumed to be plastically incompressible (Khan & Huang, 1995a). The consequence of that is that the sum of plastic strain rate components is zero:

$$\dot{\varepsilon}_1^p + \dot{\varepsilon}_2^p + \dot{\varepsilon}_3^p = 0 \tag{5.3}$$

Temperature and rate effects

The experimental studies show that the strain rate has a pronounced effect on the material behaviour in the plastic region. The effects of increasing the loading rate, shown in Figure 5.2, are usually that the initial and subsequent stresses increase with loading rate and the ductility of the material decreases (Khan & Huang, 1995a).
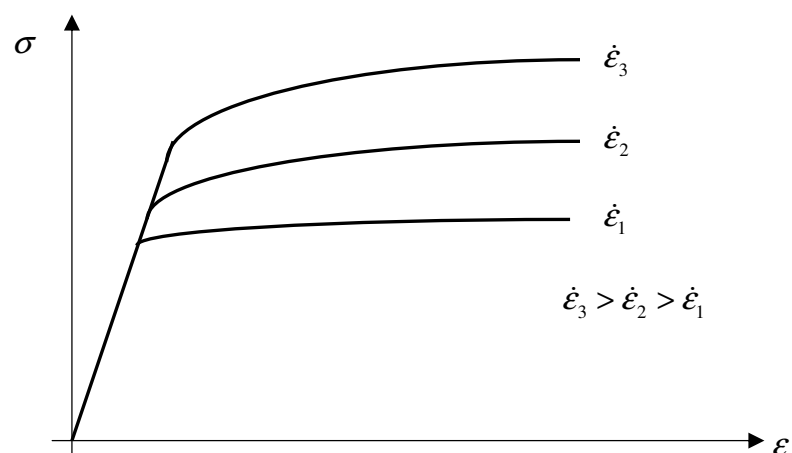
Figure 5.2. Effect of strain rate (Khan & Huang, 1995a).

The effect of temperature is presented in Figure 5.3. The stress-strain curve is higher for lower temperatures. This means that the material becomes stronger as the temperature decreases; however, lower temperature decreases ductility (Khan & Huang, 1995a).
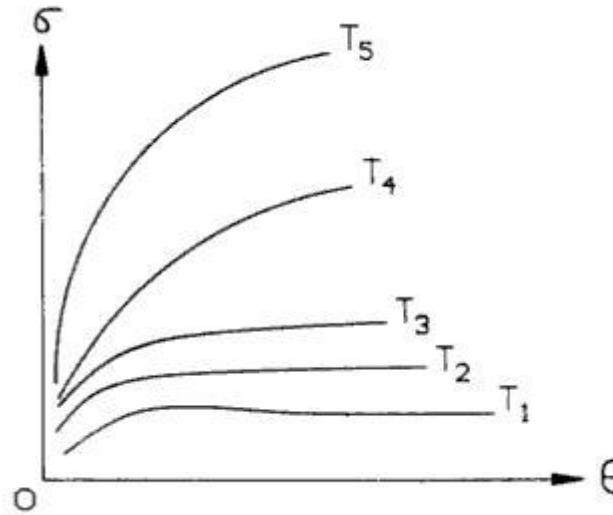
Figure 5.3. Stress-strain curves at different temperatures (Khan & Huang, 1995a). Temperatures $T_5 < T_4 < \cdots < T_1$.

5.1.1 Effective stress and plastic strain rate

The effective or von Mises equivalent tensile stress is used to predict yielding of materials under multiaxial loading conditions using results from simple uniaxial tensile tests. In terms of principal stresses σ_1, σ_2 and σ_3 it is defined as

$$\sigma_e = \frac{1}{\sqrt{2}}\left[\left(\sigma_1 - \sigma_2\right)^2 + \left(\sigma_2 - \sigma_3\right)^2 + \left(\sigma_3 - \sigma_1\right)^2\right]^{1/2} \tag{5.4}$$

or in terms of components of the stress tensor

$$\sigma_e = \left[\frac{3}{2}\left(\sigma_{11}^2 + \sigma_{22}^2 + \sigma_{33}^2 + 2\sigma_{12}^2 + 2\sigma_{23}^2 + 2\sigma_{31}^2\right)\right]^{1/2} \tag{5.5}$$

The effective stress σ_e is a scalar quantity and it originates from the postulate that yielding occurs when critical elastic shear energy is achieved. Similarly, an effective plastic strain rate $\dot{p}$ is defined as

$$\dot{p} = \frac{\sqrt{2}}{3}\left[\left(\dot{\varepsilon}_1^p - \dot{\varepsilon}_2^p\right)^2 + \left(\dot{\varepsilon}_2^p - \dot{\varepsilon}_3^p\right)^2 + \left(\dot{\varepsilon}_3^p - \dot{\varepsilon}_1^p\right)^2\right]^{1/2} \tag{5.6}$$

where $\dot{\varepsilon}_1^p, \dot{\varepsilon}_2^p$ and $\dot{\varepsilon}_3^p$ are the time derivatives of the plastic part of the principal strains. In tensor notation the effective stress and plastic strain rate may be written as

$$\sigma_e = \left(\frac{3}{2}\boldsymbol{\sigma}':\boldsymbol{\sigma}'\right)^{1/2}$$

$$\dot{p} = \left(\frac{2}{3}\dot{\boldsymbol{\varepsilon}}^p : \dot{\boldsymbol{\varepsilon}}^p\right)^{1/2} \approx \left(\frac{2}{3}\dot{\boldsymbol{\varepsilon}}:\dot{\boldsymbol{\varepsilon}}\right)^{1/2}, \quad \text{for } \varepsilon^e \ll \varepsilon^p \tag{5.7}$$

where $\boldsymbol{\sigma}'$ is the deviatoric stress tensor and the symbol ':' is the double dot product of two second-order tensors as used in chapter 4. The deviatoric stress tensor can be obtained by subtracting the hydrostatic stress tensor also called the mean stress tensor $\sigma_m = \frac{1}{3}(\sigma_{11} + \sigma_{22} + \sigma_{33})$ from the stress tensor, i.e.

$$\boldsymbol{\sigma}' = \boldsymbol{\sigma} - \frac{1}{3}Tr(\boldsymbol{\sigma})\mathbf{I} \tag{5.8}$$

The deviatoric stress tensor has three deviatoric stress invariants J_1', J_2', J_3' which have the same values regardless of the orientation of the coordinate system. The three invariants are given by

$$J_1' = \sigma_{kk}' = 0 \tag{5.9}$$

$$J_2' = \frac{1}{2}\sigma_{ij}'\sigma_{ji}' = -\sigma_1'\sigma_2' - \sigma_2'\sigma_3' - \sigma_3'\sigma_1' = \frac{1}{6}\left[(\sigma_1 - \sigma_2)^2 + (\sigma_2 - \sigma_3)^2 + (\sigma_3 - \sigma_1)^2\right] \tag{5.10}$$

$$J_3' = \det\left(\sigma_{ij}'\right) = \frac{1}{3}\sigma_{ij}'\sigma_{jk}'\sigma_{ki}' = \sigma_1\sigma_2\sigma_3 \tag{5.11}$$

Because $\sigma_{kk}' = 0$ the deviatoric stresses tend to distort the body and the hydrostatic stresses tend to change its volume. Note that using (5.10) the effective stress can be expressed in terms of second deviatoric invariant, that is

$$\sigma_e = \sqrt{3J_2'} \tag{5.12}$$

In the case of uniaxial tensile test $(\sigma_{11} = \sigma, \sigma_{22} = \sigma_{33} = 0)$, for a large plastic strain $(\varepsilon \approx \varepsilon^p)$ the deviatoric stress tensor and the strain rate tensor are given by

$$\boldsymbol{\sigma}' = \begin{pmatrix} \frac{2}{3}\sigma & 0 & 0 \\ 0 & -\frac{1}{3}\sigma & 0 \\ 0 & 0 & -\frac{1}{3}\sigma \end{pmatrix}, \quad \dot{\boldsymbol{\varepsilon}} = \begin{pmatrix} \dot{\varepsilon} & 0 & 0 \\ 0 & -\frac{1}{2}\dot{\varepsilon} & 0 \\ 0 & 0 & -\frac{1}{2}\dot{\varepsilon} \end{pmatrix}$$

Using now (5.7) we see that for a uniaxial tensile test the deviatoric stress tensor $\sigma_e = \sigma$ and the plastic strain rate $\dot{p} = \dot{\varepsilon}$.

5.1.2 Yield criterion

A yield criterion is a law defining the limit of elasticity under any possible combination of stresses and in general it is expressible in the form

$$f(J_1, J_2, J_3) = 0 \tag{5.13}$$

where J_1, J_2, J_3 are the first three invariants of the stress tensor $\boldsymbol{\sigma}$. In terms of principal stresses they are given by

$$J_1 = \sigma_1 + \sigma_2 + \sigma_3, \quad J_2 = -\sigma_1\sigma_2 - \sigma_2\sigma_3 - \sigma_3\sigma_1, \quad J_3 = \sigma_1\sigma_2\sigma_3 \tag{5.14}$$

The yield function (5.13) can be simplified by the experimental observations where it is noticed that yield of the material is not affected by a moderate hydrostatic pressure, thus it depends on invariants of deviatoric stress tensor (5.9) - (5.11). Moreover it must be independent of the Bauschinger effect, so that the magnitude of the yield stress is the same in tension and compression. Finally, yield in polycrystalline materials can be taken to be isotropic, thus the yield function must be symmetric.

The first main yield criterion is due to Tresca. The criterion, also known as maximum shear stress yield criterion is specified by

$$\max\left(|\sigma_1 - \sigma_2|, |\sigma_2 - \sigma_3|, |\sigma_3 - \sigma_1|\right) = \sigma_y \tag{5.15}$$

Another yield criterion commonly used in engineering practice is that due to von Mises. Von Mises suggested that yielding occurred when J_2' reached a critical value and for this reason the plastic flow based on the von Mises yield criterion is often called as J_2' plasticity. The von Mises yield function is defined by

$$f(J_2') = \sqrt{3J_2'} - \sigma_y = 0 \tag{5.16}$$

where σ_y is yield strength. Using (5.12) we have the yield function in terms of the effective stress

$$f = \sigma_e - \sigma_y = 0 \tag{5.17}$$

From equation (5.17) it is apparent that the material starts to yield when the effective stress reaches a critical value of yield strength.
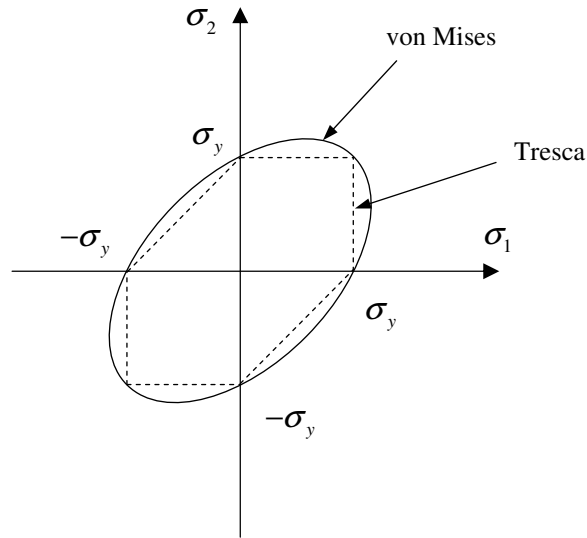
Figure 5.4. Comparison of the Tresca and von Mises yield surfaces in plane stress conditions.

The von Mises yield criterion in plane stress $\left(\sigma_3 = 0\right)$ becomes

$$f = \frac{1}{\sqrt{2}}\left[\left(\sigma_1 - \sigma_2\right)^2 + \sigma_2^2 + \sigma_1^2\right]^{1/2} - \sigma_y = 0 \qquad (5.18)$$

and so

$$\sigma_1^2 - \sigma_1\sigma_2 + \sigma_2^2 = \sigma_y^2 \qquad (5.19)$$

Equation (5.19) is an ellipse and is presented in Figure 5.4. Also in this figure the Tresca yield criterion is given for comparison. The Tresca yield criterion for plain stress is a set of straight lines

$$\sigma_1 = \pm\sigma_y \quad \sigma_2 = \pm\sigma_y \quad \sigma_1 - \sigma_2 = \pm\sigma_y \qquad (5.20)$$

We can see that Tresca's criterion predicts plastic yielding already for stress states that are still elastic according to the von Mises criterion.

5.1.3 The plastic flow rule

The plastic flow rule describes how the plastic phenomena occur. If the load point $\boldsymbol{\sigma}$ lies within the elasticity region $f\left(\boldsymbol{\sigma}\right) < 0$ then the strain increments $d\boldsymbol{\varepsilon}$ are

elastic. If the load point $\boldsymbol{\sigma}$ is on the boundary of the elasticity region $f(\boldsymbol{\sigma}) = 0$ but leaves it during elastic unloading $df(\boldsymbol{\sigma}) < 0$ the strain increment is also elastic. In the case when the load point $\boldsymbol{\sigma}$ is on the boundary of the elasticity region $f(\boldsymbol{\sigma}) = 0$ and $df(\boldsymbol{\sigma}) = 0$ then the strain increment $d\boldsymbol{\varepsilon}$ may not be elastic. This is expressed by (Suzalec, 2004)

$$d\boldsymbol{\varepsilon}^p = 0 \ \text{ if } \ f < 0 \ \text{ or if } \ f = 0 \ \text{ and } \ df < 0$$
$$d\boldsymbol{\varepsilon} = d\boldsymbol{\varepsilon}^e + d\boldsymbol{\varepsilon}^p \ \text{ if } \ f = 0 \ \text{ and } \ df = 0$$

$$(5.21)$$
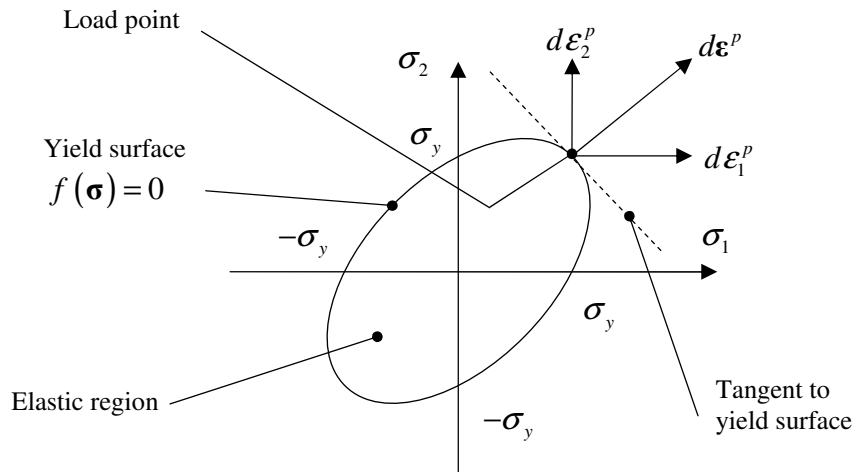
Figure 5.5. The von Mises yield surface represented in plane stress with the increment in plastic strain in a direction normal to the tangent to the surface (Dunne & Petrinic, 2005c).

For the von Mises yield criterion the yield surface is convex and the flow rule is associated with the criterion. The hypothesis of normality states that the increment in the plastic strain tensor is in a direction which is normal to the tangent to the yield surface at the load point, see Figure 5.5. This is given by the following

$$d\boldsymbol{\varepsilon}^p = d\lambda \frac{\partial f}{\partial \boldsymbol{\sigma}} \ \text{ or } \ \dot{\boldsymbol{\varepsilon}}^p = \dot{\lambda} \frac{\partial f}{\partial \boldsymbol{\sigma}}$$

$$(5.22)$$

where $\dfrac{\partial f}{\partial \boldsymbol{\sigma}}$ is the direction of the plastic strain increment or plastic strain rate and $d\lambda$ is the plastic multiplier, which determines the magnitude of the plastic strain

increment. Considering the principal components of the stress tensor and using (5.8) we have the direction of plastic flow given by the following

$$\frac{\partial f}{\partial \sigma_i} = \frac{(3/2)\left[\sigma_i - (1/3)(\sigma_1 + \sigma_2 + \sigma_3)\right]}{\sigma_e} = \frac{3}{2}\frac{\sigma_i'}{\sigma_e} \tag{5.23}$$

so that (5.22) is now expressed by

$$d\boldsymbol{\varepsilon}^p = \frac{3}{2}d\lambda\frac{\boldsymbol{\sigma}'}{\sigma_e} \tag{5.24}$$

Using now the expression for the effective plastic strain rate (5.7) we can write a similar equation for the increment in effective plastic strain, such that

$$dp = \left(\frac{2}{3}d\boldsymbol{\varepsilon}^p : d\boldsymbol{\varepsilon}^p\right)^{1/2} = \left(\frac{2}{3}\frac{3}{2}d\lambda\frac{\boldsymbol{\sigma}'}{\sigma_e} : \frac{3}{2}d\lambda\frac{\boldsymbol{\sigma}'}{\sigma_e}\right)^{1/2} = d\lambda\frac{\left((3/2)\boldsymbol{\sigma}':\boldsymbol{\sigma}'\right)^{1/2}}{\sigma_e} \tag{5.25}$$

where we used (5.24). With equation (5.7) we obtain

$$dp = d\lambda \text{ or } \dot{p} = \dot{\lambda} \tag{5.26}$$

This implies that for von Mises material the plastic multiplier $d\lambda$ is simply the increment in effective plastic strain. The plastic multiplier $d\lambda$ or $\dot{\lambda}$ can be determined from the consistency condition of plastic deformation. The consistency condition requires that the stress state or equivalently the load point must remain on the yield surface during plastic deformation or subsequent yield surface for hardening materials. The yield condition given in (5.17) depends on components of the stress tensor and the yield stress, which in turn very often increase (hardening) or decrease (softening). Generally,

$$\sigma_y = \sigma_y\left(\alpha_i\right) \tag{5.27}$$

where α_i are all the possible hardening parameters such as the equivalent plastic strain and the internal variables. α_i can be scalar, vector or tensor representing expansion, translation and distortion, respectively, of the yield surface. For von Mises material $\alpha = p$ and the yield function can now be written as

$$f\left(\boldsymbol{\sigma},\alpha\right) = f\left(\boldsymbol{\sigma}, p\right) = \sigma_e\left(\boldsymbol{\sigma}\right) - \sigma_y\left(p\right) = 0 \tag{5.28}$$

Considering the plastic deformation caused by an infinitesimal increment of stress $d\boldsymbol{\sigma}$ and plastic strain dp the consistency condition requires that

$$f\left(\boldsymbol{\sigma} + d\boldsymbol{\sigma}, p + dp\right) = 0 \tag{5.29}$$

The left hand side of (5.29) is expanded into

$$f\left(\boldsymbol{\sigma}+d\boldsymbol{\sigma},\,p+dp\right)=f\left(\boldsymbol{\sigma},p\right)+\frac{\partial f}{\partial\boldsymbol{\sigma}}:d\boldsymbol{\sigma}+\frac{\partial f}{\partial p}dp \tag{5.30}$$

Combining (5.28) and (5.29) with (5.30) gives

$$\frac{\partial f}{\partial\boldsymbol{\sigma}}:d\boldsymbol{\sigma}+\frac{\partial f}{\partial p}dp=0 \tag{5.31}$$

Taking the stress-strain relation for elastic deformation (5.2) in an incremental form we have

$$d\boldsymbol{\sigma}=\mathbf{C}^{e}d\boldsymbol{\varepsilon}^{e}=\mathbf{C}^{e}\left(d\boldsymbol{\varepsilon}-d\boldsymbol{\varepsilon}^{p}\right) \tag{5.32}$$

where $\mathbf{C}^{e}$ is the elastic stiffness matrix. Substituting (5.22) into (5.32) we obtain

$$d\boldsymbol{\sigma}=\mathbf{C}^{e}\left(d\boldsymbol{\varepsilon}-d\lambda\frac{\partial f}{\partial\boldsymbol{\sigma}}\right) \tag{5.33}$$

and now substituting (5.33) into (5.31) gives

$$\frac{\partial f}{\partial\boldsymbol{\sigma}}:\mathbf{C}^{e}\left(d\boldsymbol{\varepsilon}-d\lambda\frac{\partial f}{\partial\boldsymbol{\sigma}}\right)+\frac{\partial f}{\partial p}dp=0 \tag{5.34}$$

Using (5.22), (5.25) and (5.34) we can derive the equation for plastic multiplier

$$d\lambda=\frac{\left(\partial f/\partial\boldsymbol{\sigma}\right):\mathbf{C}^{e}d\boldsymbol{\varepsilon}}{\left(\partial f/\partial\boldsymbol{\sigma}\right):\mathbf{C}^{e}\left(\partial f/\partial\boldsymbol{\sigma}\right)-\left(\partial f/\partial p\right)\left(\left(2/3\right)\left(\partial f/\partial\boldsymbol{\sigma}\right):\left(\partial f/\partial\boldsymbol{\sigma}\right)\right)^{1/2}} \tag{5.35}$$

or using (5.25) and (5.31) we obtain the plastic multiplier in terms of stress increment

$$d\lambda=\frac{-\left(\partial f/\partial\boldsymbol{\sigma}\right):d\boldsymbol{\sigma}}{\left(\partial f/\partial p\right)\left(\left(2/3\right)\left(\partial f/\partial\boldsymbol{\sigma}\right):\left(\partial f/\partial\boldsymbol{\sigma}\right)\right)} \tag{5.36}$$

The stress increment can now be determined by substituting (5.35) into (5.33) to give

$$d\boldsymbol{\sigma}=\left(\mathbf{C}^{e}-\mathbf{C}^{e}\frac{\partial f}{\partial\boldsymbol{\sigma}}\frac{\left(\partial f/\partial\boldsymbol{\sigma}\right):\mathbf{C}^{e}}{\left(\partial f/\partial\boldsymbol{\sigma}\right):\mathbf{C}^{e}\left(\partial f/\partial\boldsymbol{\sigma}\right)-\left(\partial f/\partial p\right)\left(\left(2/3\right)\left(\partial f/\partial\boldsymbol{\sigma}\right):\left(\partial f/\partial\boldsymbol{\sigma}\right)\right)^{1/2}}\right)d\boldsymbol{\varepsilon} \tag{5.37}$$

or

$$d\boldsymbol{\sigma}=\mathbf{C}^{ep}d\boldsymbol{\varepsilon} \tag{5.38}$$

where $\mathbf{C}^{ep}$ is elasto-plastic stiffness tensor.

5.1.4 Isotropic hardening

For many plastic materials after initial yielding the stress required for further plastic deformation increases, this is called hardening. For isotropic, pressure-insensitive von Mises materials, the yield function for isotropic hardening can be given by (5.28). This is based on the assumption that the amount of hardening depends on the effective plastic strain but does not depend on the strain path.
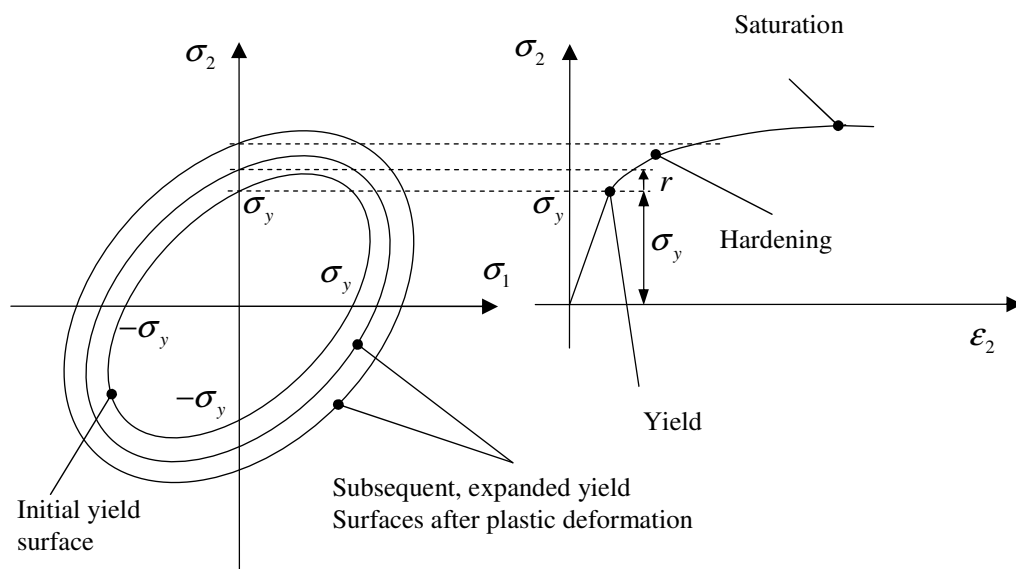
Figure 5.6. Isotropic hardening with corresponding stress-strain curve (Dunne & Petrinic, 2005d).

A stress-strain curve with nonlinear isotropic hardening is shown in Figure 5.6. As can be seen the yield function is expanding and the amount of expansion is often taken to be a function of accumulated plastic strain, thus $\sigma_y = \sigma_y(p)$. The yield stress might be of the form (Dunne & Petrinic, 2005d)

$$\sigma_y(p) = \sigma_{y0} + r(p) \tag{5.39}$$

where σ_{y0} is the initial yield stress and $r(p)$ is called isotropic yield function, which can be of the following form

$$\dot{r}(p) = b(Q - r)\dot{p} \quad \text{or} \quad dr(p) = b(Q - r)dp \tag{5.40}$$

in which b and Q are material constants, which give an exponential shape to the uniaxial stress-strain curve which saturates with increasing plastic strain, since solving (5.40) with the initial condition $r(0) = 0$ gives

$$r(p) = Q(1 - e^{-bp}),$$
(5.41)

where Q is the saturated value of r so that the peak stress achieved with this kind of hardening is therefore $(\sigma_{y0} + Q)$. The constant b determines the rate at which the saturation is achieved (Dunne & Petrinic, 2005d).

For linear isotropic hardening we can write the isotropic hardening function as follows

$$dr(p) = hdp$$
(5.42)

where h is a constant. The stress-strain curve for linear hardening is shown in Figure 5.7. For uniaxial conditions $dp = d\varepsilon^p$ and the stress increase due to isotropic hardening is just dr, hence we have the following

$$d\varepsilon^p = \frac{d\sigma}{h}$$
(5.43)

and the increment in elastic strain is

$$d\varepsilon^e = \frac{d\sigma}{E}$$
(5.44)

The total strain is

$$d\varepsilon = \frac{d\sigma}{E} + \frac{d\sigma}{h} = d\sigma\left(\frac{E+h}{Eh}\right)$$
(5.45)

giving

$$d\sigma = E\left(1 - \frac{E}{E+h}\right)d\varepsilon$$
(5.46)
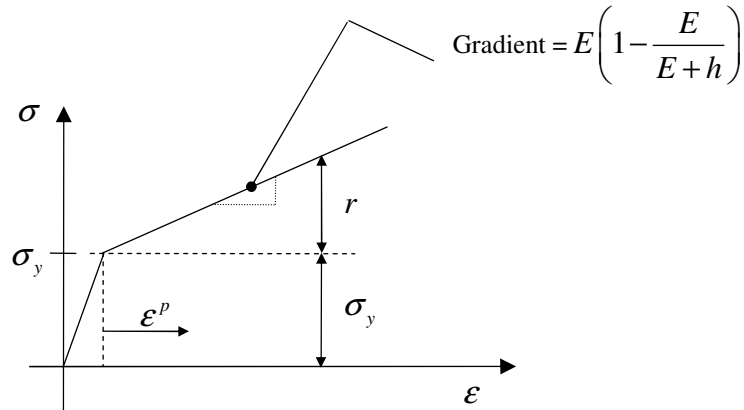
Figure 5.7. Stress-strain curve for linear strain hardening (Dunne & Petrinic, 2005e).

5.2 Elasto-plastic coupling

The kinematics of finite deformations was briefly introduced in section 4.1. This section describes elasto-plastic coupling of finite plastic deformations based on multiplicative decomposition of the deformation gradient tensor proposed by Lee (1969). Considering an element of material containing infinitesimal line segment $d\mathbf{X}$, which after deformation transforms to $d\mathbf{x}$, as shown schematically in Figure 5.8. The deformation is governed by the equation (4.9). In finite plasticity theory, see (Dunne & Petrinic, 2005f; Khan & Huang, 1995b), an intermediate configuration is introduced. This is an imaginary configuration, which can be obtained from the current configuration by unloading to a stress-free state, or by pure plastic deformation from undeformed configuration, such that $d\mathbf{X}$ deforms to $d\mathbf{p}$ in the intermediate configuration. The deformation of $d\mathbf{X}$ into $d\mathbf{x}$ can be accomplished in the following two steps:

1. purely plastic deformation of $d\mathbf{X}$ into $d\mathbf{p}$ given by

$$d\mathbf{p} = \mathbf{F}^p d\mathbf{X} \tag{5.47}$$

where $\mathbf{F}^p$ is the plastic deformation gradient,

$$\mathbf{F}^p = \frac{\partial \mathbf{p}}{\partial \mathbf{X}} \tag{5.48}$$

2. elastic deformation of $d\mathbf{p}$ into $d\mathbf{x}$ in the current configuration given by

$$d\mathbf{x} = \mathbf{F}^e d\mathbf{p} \qquad (5.49)$$

where $\mathbf{F}^e$ is the elastic deformation gradient,

$$\mathbf{F}^e = \frac{\partial \mathbf{x}}{\partial \mathbf{p}} \qquad (5.50)$$

Using (5.47) and (5.49) we can write

$$d\mathbf{x} = \mathbf{F}^e d\mathbf{p} = \mathbf{F}^e \mathbf{F}^p d\mathbf{X} \qquad (5.51)$$

This gives the following well-known multiplicative decomposition of the deformation gradient tensor

$$\mathbf{F} = \mathbf{F}^e \mathbf{F}^p \qquad (5.52)$$
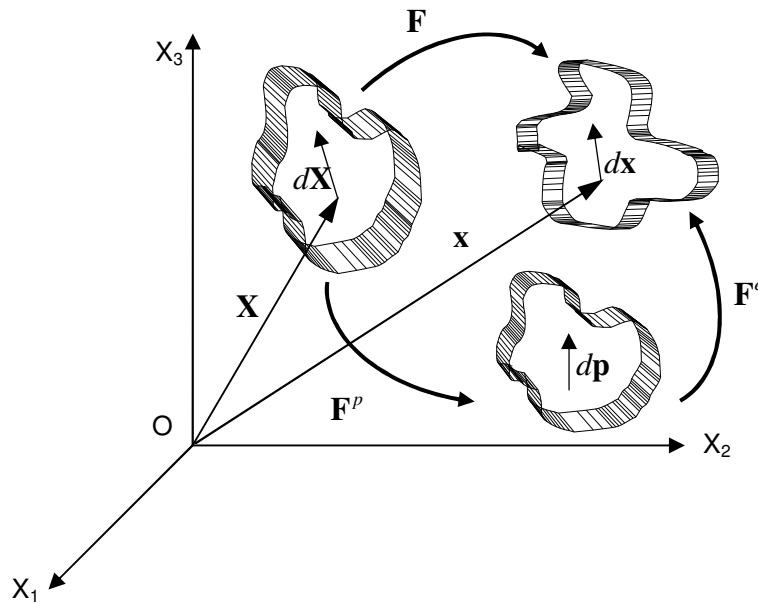
Figure 5.8. Multiplicative decomposition of the deformation gradient tensor.

For general inhomogeneous plastic deformation, unloading a body will not generally lead to zero stress state; instead, a residual stress field will result. In this case the body can be imaginarily divided into infinite number of infinitesimal elements, at which unstressed configuration can be obtained. This results in $\mathbf{F}^e$ and $\mathbf{F}^p$ being no longer continuous, but can be defined as point-functions that relate the

deformations in infinitesimal neighborhoods of a material particle, and (5.52) will hold. Moreover, the intermediate configuration $\mathbf{p}$, is in general, not uniquely determined since an arbitrary rigid body rotation can be superimposed on it and leave it unstressed. To overcome this nonuniqueness it is assumed, by convention, that the rigid body rotation is lumped into the plastic deformation gradient $\mathbf{F}^p$ and the elastic deformation gradient $\mathbf{F}^e$ includes pure deformation, without rigid body rotation. Thus, $\mathbf{F}^e$ is chosen to be

$$\mathbf{F}^e = \mathbf{V}^e \tag{5.53}$$

which is a symmetric tensor. For $\mathbf{F}^p$ we have

$$\mathbf{F}^p = \mathbf{V}^p \mathbf{R} \tag{5.54}$$

where $\mathbf{R}$ is the equivalent total rigid body rotation.

The velocity gradient (which was first introduced in (4.91)) in terms of elastic and plastic deformation gradients is given by

$$\begin{aligned}
\mathbf{L} = \dot{\mathbf{F}} \mathbf{F}^{-1} &= \frac{\partial}{\partial t} \left(\mathbf{F}^e \mathbf{F}^p \right) \left(\mathbf{F}^e \mathbf{F}^p \right)^{-1} = \left(\mathbf{F}^e \dot{\mathbf{F}}^p + \dot{\mathbf{F}}^e \mathbf{F}^p \right) \mathbf{F}^{p-1} \mathbf{F}^{e-1} \\
&= \dot{\mathbf{F}}^e \mathbf{F}^{e-1} + \mathbf{F}^e \dot{\mathbf{F}}^p \mathbf{F}^{p-1} \mathbf{F}^{e-1} = \dot{\mathbf{V}}^e \mathbf{V}^{e-1} + \mathbf{V}^e \dot{\mathbf{F}}^p \mathbf{F}^{p-1} \mathbf{V}^{e-1}
\end{aligned} \tag{5.55}$$

Introducing elastic and plastic velocity gradients $\mathbf{L}^e$ and $\mathbf{L}^p$ given by

$$\begin{aligned}
\mathbf{L}^e &= \dot{\mathbf{V}}^e \mathbf{V}^{e-1} = \mathbf{D}^e + \mathbf{W}^e \\
\mathbf{L}^p &= \dot{\mathbf{F}}^p \mathbf{F}^{p-1} = \mathbf{D}^p + \mathbf{W}^p
\end{aligned} \tag{5.56}$$

we have

$$\mathbf{L} = \mathbf{L}^e + \mathbf{V}^e \mathbf{L}^p \mathbf{V}^{e-1}, \tag{5.57}$$

where in (5.56) $\mathbf{D}^e, \mathbf{D}^p$ and $\mathbf{W}^e, \mathbf{W}^p$ are, respectively, the symmetric and antisymmetric parts of $\mathbf{L}^e$ and $\mathbf{L}^p$. Using (5.56) and (5.57) we obtain

$$\mathbf{D} = \mathbf{D}^e + \mathrm{sym}\left(\mathbf{V}^e \mathbf{D}^p \mathbf{V}^{e-1} \right) + \mathrm{sym}\left(\mathbf{V}^e \mathbf{W}^p \mathbf{V}^{e-1} \right) \tag{5.58}$$

and

$$\mathbf{W} = \mathbf{W}^e + \mathrm{asym}\left(\mathbf{V}^e \mathbf{D}^p \mathbf{V}^{e-1} \right) + \mathrm{asym}\left(\mathbf{V}^e \mathbf{W}^p \mathbf{V}^{e-1} \right) \tag{5.59}$$

From these two equations it can be seen that in finite elasto-plastic deformation the additive decomposition for the deformation rate does not hold in general:

$$\mathbf{D} \neq \mathbf{D}^e + \mathbf{D}^p \tag{5.60}$$

However, for most of the materials the elastic strain is negligible compared to plastic strain in the case of large deformation, so it is reasonable to assume that the

elastic stretch tensor $\mathbf{V}^e$ is not different from the unit tensor $\left(\text{i.e., } \mathbf{V}^e \approx \mathbf{I} + \boldsymbol{\varepsilon}^e\right)$, where $\boldsymbol{\varepsilon}^e$ is the infinitesimal strain tensor. Hence, we assume that

$$\mathbf{D} = \mathbf{D}^e + \mathbf{D}^p \tag{5.61}$$

and

$$\mathbf{W} = \mathbf{W}^e + \mathbf{W}^p \tag{5.62}$$

The above assumption is commonly used in the plasticity theories for finite deformation. This decomposition of the deformation rate $\mathbf{D}$ requires for constitutive laws for both $\mathbf{D}^e$ and $\mathbf{D}^p$. Often, in finite element implementations, the total rate of deformation, $\mathbf{D}$, is known such that if $\mathbf{D}^p$ is specified by a constitutive equation, then $\mathbf{D}^e$ can be determined using (5.61) so that the stress rate may be determined using Hooke's law. Once we know the stress rate, we can integrate over time to determine stress (Dunne & Petrinic, 2005f).

5.3 Material objectivity and objective stress rates

For the constitutive model that is used for the current finite elasto-plastic description of the material, relations expressed in terms which transform correctly if the frame of reference is changed are needed and the principle of material objectivity, also called principle of material frame indifference, is considered here. It requires that constitutive equation must be invariant under changes of frame of reference. In other words, the constitutive equation must provide information about the material response which is independent of rigid body rotation (Dunne & Petrinic, 2005g).

Consider a change of time-space reference given by

$$\mathbf{x}^*(t) = \mathbf{c}(t) + \mathbf{Q}(t)\mathbf{x} \tag{5.63}$$

$$t^* = t - a \tag{5.64}$$

where $\mathbf{c}(t)$ is a vector and $\mathbf{Q}(t)$ is an orthogonal tensor representing the translation and rotation of the spatial coordinate system, and a is a constant denoting the shift of time. A vector and tensor are objective if they satisfy the following transformation

$$\mathbf{v}^* = \mathbf{Q}\mathbf{v} \tag{5.65}$$

$$\mathbf{A}^* = \mathbf{Q}\mathbf{A}\mathbf{Q}^T \tag{5.66}$$

where * represents a quantity in the new frame of reference.

We will now look at the transformation of the deformation gradient, the velocity gradient and the rate of deformation tensor. For the deformation gradient $\mathbf{F}$ in the reference configuration we have that

$$dx = \mathbf{F}d\mathbf{X} \tag{5.67}$$

After rotation $\mathbf{Q}$ (5.67) becomes

$$dx^* = \mathbf{F}^* d\mathbf{X}^* \tag{5.68}$$

From equation (5.63) and (5.67) we have

$$dx^* = \mathbf{Q}dx = \mathbf{Q}\mathbf{F}d\mathbf{X} \tag{5.69}$$

and since $d\mathbf{X}$ remains unchanged under the deformation, so that $d\mathbf{X}^* = d\mathbf{X}$ we have from (5.69) the following

$$\mathbf{F}^* = \mathbf{Q}\mathbf{F} \tag{5.70}$$

Because $\mathbf{F}$ is a two-point tensor, only one of its two indices is in spatial coordinate $\mathbf{x}$, it is objective and transforms like a vector under change of frame of reference. It is not however objective as a tensor.

From equation (5.70), after differentiation we have

$$\dot{\mathbf{F}}^* = \dot{\mathbf{Q}}\mathbf{F} + \mathbf{Q}\dot{\mathbf{F}}$$

so that

$$\mathbf{L}^* = \dot{\mathbf{F}}^*\mathbf{F}^{*-1} = \left(\dot{\mathbf{Q}}\mathbf{F} + \mathbf{Q}\dot{\mathbf{F}}\right)\mathbf{F}^{-1}\mathbf{Q}^{-1} = \dot{\mathbf{Q}}\mathbf{Q}^T + \mathbf{Q}\dot{\mathbf{F}}\mathbf{F}^{-1}\mathbf{Q}^T = \dot{\mathbf{Q}}\mathbf{Q}^T + \mathbf{Q}\mathbf{L}\mathbf{Q}^T \tag{5.71}$$

This shows that the velocity gradient is not objective. Since $\mathbf{Q}\mathbf{Q}^T = \mathbf{I}$ we obtain

$$\dot{\mathbf{Q}}\mathbf{Q}^T + \mathbf{Q}\dot{\mathbf{Q}}^T = \mathbf{0}$$

and so

$$\dot{\mathbf{Q}}\mathbf{Q}^T = -\left(\dot{\mathbf{Q}}\mathbf{Q}^T\right)^T \tag{5.72}$$

From (5.72) we have seen that $\dot{\mathbf{Q}}\mathbf{Q}^T$ is antisymmetric, thus we can decompose $\mathbf{L}^*$ into symmetric part $\mathbf{D}^*$ and antisymmetric part $\mathbf{W}^*$ in the form

$$\mathbf{L}^* = \frac{1}{2}\mathbf{Q}\left(\mathbf{L} + \mathbf{L}^T\right)\mathbf{Q}^T + \frac{1}{2}\mathbf{Q}\left(\mathbf{L} - \mathbf{L}^T\right)\mathbf{Q}^T + \dot{\mathbf{Q}}\mathbf{Q}^T \tag{5.73}$$

Therefore from (5.73) we obtain

$$\mathbf{D}^* = \frac{1}{2}\mathbf{Q}\left(\mathbf{L} + \mathbf{L}^T\right)\mathbf{Q}^T = \mathbf{Q}\mathbf{D}\mathbf{Q}^T \tag{5.74}$$

$$\mathbf{W}^* = \frac{1}{2}\mathbf{Q}\left(\mathbf{L} - \mathbf{L}^T\right)\mathbf{Q}^T + \dot{\mathbf{Q}}\mathbf{Q}^T = \mathbf{Q}\mathbf{W}\mathbf{Q}^T + \dot{\mathbf{Q}}\mathbf{Q}^T \tag{5.75}$$

This shows that the rate of deformation $\mathbf{D}$ is objective, but the continuum spin $\mathbf{W}$ is not objective.

We will now discuss the transformation laws for stress measures and their material derivatives. Let $\boldsymbol{\sigma}$ be the Cauchy stress tensor and consider the stress vector $\mathbf{t} = \boldsymbol{\sigma}\mathbf{n}$ acting on a surface with normal $\mathbf{n}$. Under some rotation $\mathbf{Q}$ the stress vector $\mathbf{t}$ is transformed to $\mathbf{t}^*$ acting on a plane with normal $\mathbf{n}^*$ such that if $\mathbf{t} = \boldsymbol{\sigma}\mathbf{n}$ before the rotation, then after rotation it becomes $\mathbf{t}^* = \boldsymbol{\sigma}^*\mathbf{n}^*$. On the other hand vectors $\mathbf{t}$ and $\mathbf{n}$ transform according to (5.65) which gives

$$\mathbf{t}^* = \mathbf{Q}\boldsymbol{\sigma}\mathbf{n} \text{ and } \mathbf{n} = \mathbf{Q}^T\mathbf{n}^*$$

thus

$$\mathbf{t}^* = \boldsymbol{\sigma}^*\mathbf{n}^* = \mathbf{Q}\boldsymbol{\sigma}\mathbf{Q}^T\mathbf{n}^*$$

so that

$$\boldsymbol{\sigma}^* = \mathbf{Q}\boldsymbol{\sigma}\mathbf{Q}^T \tag{5.76}$$

The above proves that the Cauchy stress tensor is objective. From equation (4.54) the nominal stress in x^* becomes

$$\boldsymbol{\Pi}^* = \det\left(\mathbf{F}^*\right)\mathbf{F}^{*-1}\boldsymbol{\sigma}^* = \det\left(\mathbf{F}\right)\mathbf{F}^{-1}\boldsymbol{\sigma}\mathbf{Q}^T = \boldsymbol{\Pi}\mathbf{Q}^T \tag{5.77}$$

where we used $\det\left(\mathbf{F}^*\right) = \det\left(\mathbf{Q}\mathbf{F}\right) = \det\left(\mathbf{Q}\right)\det\left(\mathbf{F}\right) = \det\left(\mathbf{F}\right)$. Similarly for the second Piola-Kirchhoff stress $\mathbf{S}$ the transformation law is

$$\mathbf{S}^* = \det\left(\mathbf{F}^*\right)\mathbf{F}^{*-1}\boldsymbol{\sigma}^*\mathbf{F}^* = \det\left(\mathbf{F}\right)\mathbf{F}^{-1}\boldsymbol{\sigma}\mathbf{F} = \mathbf{S} \tag{5.78}$$

Therefore $\boldsymbol{\Pi}$ and $\mathbf{S}$ are not frame indifferent.

In plasticity theory the constitutive equations are usually written in an incremental form, since the stress is dependent on history of the plastic deformation. Thus the material derivative of the stress tensor, rather than stress tensor itself, is used in formulating the constitutive equations (Khan & Huang, 1995a). Differentiating the transformation of Cauchy stress tensor (5.76) with respect to time we obtain

$$\dot{\boldsymbol{\sigma}}^* = \dot{\mathbf{Q}}\boldsymbol{\sigma}\mathbf{Q}^T + \mathbf{Q}\dot{\boldsymbol{\sigma}}\mathbf{Q}^T + \mathbf{Q}\boldsymbol{\sigma}\dot{\mathbf{Q}}^T \tag{5.79}$$

As we can see the rate of stress is not objective, it does not obey the transformation law given by equation (5.66). Therefore it is inappropriate to use it in formulating constitutive equations in plasticity theory. To solve this problem a

corotational stress rate was introduced by Jaumann, which can be derived by substituting $\dot{\mathbf{Q}}$ and $\dot{\mathbf{Q}}^T$ from (5.75) into (5.79) to get

$$\dot{\boldsymbol{\sigma}}^* = \mathbf{Q}\dot{\boldsymbol{\sigma}}\mathbf{Q}^T + \mathbf{W}^*\mathbf{Q}\boldsymbol{\sigma}\mathbf{Q}^T - \mathbf{Q}\mathbf{W}\boldsymbol{\sigma}\mathbf{Q}^T - \mathbf{Q}\boldsymbol{\sigma}\mathbf{Q}^T\mathbf{W}^* + \mathbf{Q}\boldsymbol{\sigma}\mathbf{W}\mathbf{Q}^T\mathbf{W}\mathbf{Q}^T$$
$$= \mathbf{Q}\left(\dot{\boldsymbol{\sigma}} - \mathbf{W}\boldsymbol{\sigma} + \boldsymbol{\sigma}\mathbf{W}\right)\mathbf{Q}^T + \mathbf{W}^*\boldsymbol{\sigma}^* - \boldsymbol{\sigma}^*\mathbf{W}^*$$

after reordering we obtain

$$\dot{\boldsymbol{\sigma}}^* - \mathbf{W}^*\boldsymbol{\sigma}^* + \boldsymbol{\sigma}^*\mathbf{W}^* = \mathbf{Q}\left(\dot{\boldsymbol{\sigma}} - \mathbf{W}\boldsymbol{\sigma} + \boldsymbol{\sigma}\mathbf{W}\right)\mathbf{Q}^T \qquad (5.80)$$

From equation (5.80) we can see that the quantity $\dot{\boldsymbol{\sigma}} - \mathbf{W}\boldsymbol{\sigma} + \boldsymbol{\sigma}\mathbf{W}$ is objective under change of frame of reference and it is called the Jaumann corotational stress rate, denoted by $\overset{\nabla}{\boldsymbol{\sigma}}$. It is corotational in that it represents a rate relative to a rotating frame of reference with the rate of rotation given by the spin tensor $\mathbf{W}$. The Jaumann stress rate is given by

$$\overset{\nabla}{\boldsymbol{\sigma}} = \dot{\boldsymbol{\sigma}} - \mathbf{W}\boldsymbol{\sigma} + \boldsymbol{\sigma}\mathbf{W} = \dot{\boldsymbol{\sigma}} - \mathbf{W}\boldsymbol{\sigma} - \boldsymbol{\sigma}\mathbf{W}^T \qquad (5.81)$$

Since Jaumann stress rate is objective it is suitable for use in constitutive equations. The hypoelastic constitutive equation relates the elastic rate of deformation to the Jaumann stress rate. It is given by

$$\overset{\nabla}{\boldsymbol{\sigma}} = 2G\mathbf{D}^e + \lambda\mathrm{Tr}\left(\mathbf{D}^e\right)\mathbf{I} \qquad (5.82)$$

where G and λ are conventional Lame elastic constants. The Jaumann stress tensor is not the only stress rate that is objective. For an overview of other objective stress rates the reader is referred to the literature, e.g. (Khan & Huang, 1995a).

5.4 Implementation of plasticity into Ls-Dyna

This section gives a description of the main concepts behind the commercial finite-element code called LS-DYNA. The description given here is mainly based on the theory manual for LS-DYNA (Hallquist, 2006a). LS-DYNA is a general purpose finite element code for analysing the large deformation static and dynamic response of structures. The main solution methodology is based on explicit time integration. The code allows difficult contact problems to be modeled with use of a built-in contact-impact algorithm. Spatial discretisation can be achieved by the use of a number of different elements among which are 8-node hexahedral elements used in this work.

The subsequent sections describe some of the features and procedures of LS-DYNA that are used in the current model. A three dimensional description of the sheet is considered here. First a description of the equilibrium equation and 8-node hexahedron solid elements is given, which is followed by the update of the Jaumann stress rate, time step control and finally the time integration procedure.

5.4.1 The equilibrium equation

Let V be the deformed region of a body with boundary $\partial b_1 \cup \partial b_2 \cup \partial b_3$ where ∂b_1 is where we have a traction boundary condition, ∂b_2 where we have a displacement boundary condition and ∂b_3 where we have a contact discontinuity condition. We seek to solve the equation of motion given by (4.58) satisfying the traction boundary condition on boundary ∂b_1

$$\sigma_{ij} n_i = t_i(t),\tag{5.83}$$

the displacement boundary condition on boundary ∂b_2

$$x_i(X_\alpha, t) = D_i(t)\tag{5.84}$$

and the contact discontinuity

$$\left(\sigma_{ij}^+ - \sigma_{ij}^-\right) n_i = 0\tag{5.85}$$

along the interior boundary ∂b_3 when $x_i^+ = x_i^-$. Thus, we can write the following

$$\int_v \left(\rho \ddot{x}_i - \sigma_{ij,j} - \rho b_i\right) \delta x_i dv + \int_{\partial b_1} \left(\sigma_{ij} n_j - t_i\right) \delta x_i ds + \int_{\partial b_3} \left(\sigma_{ij}^+ - \sigma_{ij}^-\right) n_j \delta x_i ds = 0\tag{5.86}$$

where δx_i satisfies all boundary conditions on δb_2, and the integrations are over the current geometry. Applying the divergence theorem we obtain

$$\int_v \left(\sigma_{ij} \delta x_i\right)_{,j} dv = \int_{\partial b_1} \sigma_{ij} n_j \delta x_i ds + \int_{\partial b_3} \left(\sigma_{ij}^+ - \sigma_{ij}^-\right) n_j \delta x_i ds\tag{5.87}$$

and noting that

$$\left(\sigma_{ij} \delta x_i\right)_{,j} - \sigma_{ij,j} \delta x_i = \sigma_{ij} \delta x_{i,j}\tag{5.88}$$

leads to the weak form of the equilibrium equations

$$\delta \pi = \int_v \rho \ddot{x}_i \delta x_i dv + \int_v \sigma_{ij} \delta x_{i,j} dv - \int_v \rho b_i \delta x_i dv - \int_{\partial b_1} t_i \delta x_i ds = 0\tag{5.89}$$

which corresponds to a statement of the principle of virtual work.

5.4.2 The 8-node hexahedron solid elements

As already mentioned the space is discretised with 8-node hexahedron elements interconnected at nodal points. The discretisation in this case is given by (Hallquist, 2006b)

$$x_i\left(X_\alpha,t\right)=x_i\left(X_\alpha\left(\xi,\eta,\zeta\right),t\right)=\sum_{j=1}^{8}\phi_j\left(\xi,\eta,\zeta\right)x_i^j\left(t\right) \tag{5.90}$$

The shape function ϕ_j is defined for the 8-node hexahedron as

$$\phi_j=\frac{1}{8}\left(1+\xi\xi_j\right)\left(1+\eta\eta_j\right)\left(1+\zeta\zeta_j\right) \tag{5.91}$$

where ξ_j,η_j,ζ_j take on their nodal values of (±1, $\pm1,\pm1$) and x_i^j is the nodal coordinate of the jth node in the ith direction, see

Figure 5.9.

Summing over the *ne* elements we may approximate the equation (5.89) with (Hallquist, 2006b)()

$$\delta\pi=\sum_{m=1}^{ne}\delta\pi_m=0 \tag{5.92}$$

and we write

$$\sum_{m=1}^{ne}\left\{\int_{v_m}\rho\ddot{x}_i\Phi_i^m dv+\int_{v_m}\sigma_{ij}^m\Phi_{i,j}^m dv-\int_{v_m}\rho b_i\Phi_i^m dv-\int_{\partial b_1}t_i\Phi_i^m ds\right\}=0 \tag{5.93}$$

where Φ_i^m corresponds to the appropriate shape function in each case. In matrix notation the computations for m-th element involve determining

$$\int_{v_m}\rho\mathbf{N}^T\mathbf{Na}dv+\int_{v_m}\mathbf{B}^T\boldsymbol{\sigma}dv-\int_{v_m}\rho\mathbf{N}^T\mathbf{b}dv-\int_{\partial b_1}\mathbf{N}^T\mathbf{t}ds=0 \tag{5.94}$$

where for a solid element, N is the 3 x 24 rectangular interpolation matrix given by

$$\mathbf{N}\left(\xi,\eta,\zeta\right)=\begin{bmatrix}\phi_1 & 0 & 0 & \phi_2 & 0 & \cdots & 0 & 0\\ 0 & \phi_1 & 0 & 0 & \phi_2 & \cdots & \phi_8 & 0\\ 0 & 0 & \phi_1 & 0 & 0 & \cdots & 0 & \phi_8\end{bmatrix} \tag{5.95}$$

$\boldsymbol{\sigma}$ is a stress vector

$$\boldsymbol{\sigma}^T = \left(\sigma_{xx}, \sigma_{yy}, \sigma_{zz}, \sigma_{xy}, \sigma_{yz}, \sigma_{zx} \right) \tag{5.96}$$

B is the 6 x 24 strain-displacement matrix

$$\mathbf{B} = \begin{bmatrix} \dfrac{\partial}{\partial x} & 0 & 0 \\[2mm] 0 & \dfrac{\partial}{\partial y} & 0 \\[2mm] 0 & 0 & \dfrac{\partial}{\partial z} \\[2mm] \dfrac{\partial}{\partial y} & \dfrac{\partial}{\partial x} & 0 \\[2mm] 0 & \dfrac{\partial}{\partial z} & \dfrac{\partial}{\partial y} \\[2mm] \dfrac{\partial}{\partial z} & 0 & \dfrac{\partial}{\partial x} \end{bmatrix} \mathbf{N} \tag{5.97}$$

a is a nodal acceleration vector, as that the acceleration is given by

$$\begin{bmatrix} \ddot{x}_1 \\ \ddot{x}_2 \\ \ddot{x}_3 \end{bmatrix} = \mathbf{N} \begin{bmatrix} a_{x_1} \\ a_{y_1} \\ \vdots \\ a_{y_k} \\ a_{z_k} \end{bmatrix} = \mathbf{Na} \tag{5.98}$$

b is the body load vector, and **t** are applied traction loads

$$\mathbf{b} = \begin{bmatrix} b_x \\ b_y \\ b_z \end{bmatrix}, \quad \mathbf{t} = \begin{bmatrix} t_x \\ t_y \\ t_z \end{bmatrix} \tag{5.99}$$

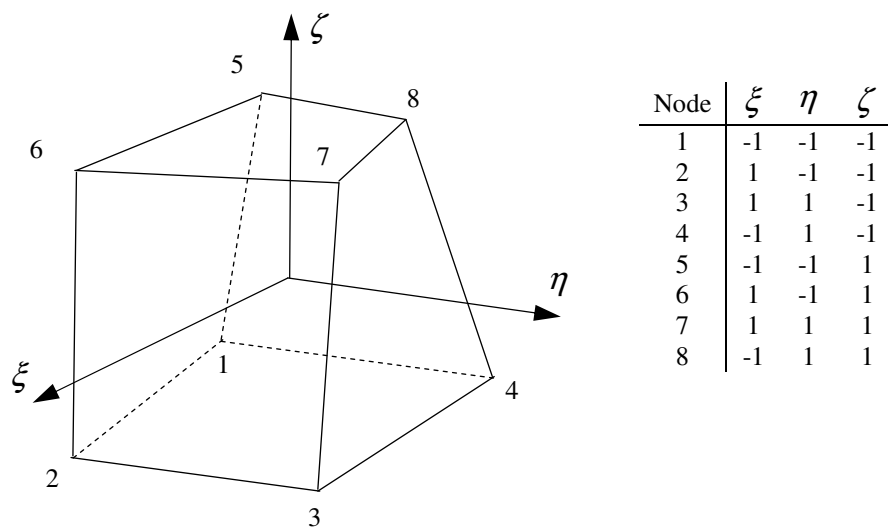| Node	ξ	η	ζ
1	-1	-1	-1
2	1	-1	-1
3	1	1	-1
4	-1	1	-1
5	-1	-1	1
6	1	-1	1
7	1	1	1
8	-1	1	1

Figure 5.9. Eight-node solid hexahedron element.

The element quantities for $m = 1, 2, ..., ne$ are assembled appropriately to generate the equations that are solved.

In order to obtain a diagonal mass matrix the entries on each row are summed giving the kth diagonal term as

$$m_{kk} = \int_v \rho \phi_k \sum_{i=1}^{8} \phi_i \, dv = \int_v \rho \phi_k \, dv \qquad (5.100)$$

The terms in the strain-displacement matrix are readily calculated using the chain rule, as follows

$$\frac{\partial \phi_i}{\partial \xi} = \frac{\partial \phi_i}{\partial x} \frac{\partial x}{\partial \xi} + \frac{\partial \phi_i}{\partial y} \frac{\partial y}{\partial \xi} + \frac{\partial \phi_i}{\partial z} \frac{\partial z}{\partial \xi}$$

$$\frac{\partial \phi_i}{\partial \eta} = \frac{\partial \phi_i}{\partial x} \frac{\partial x}{\partial \eta} + \frac{\partial \phi_i}{\partial y} \frac{\partial y}{\partial \eta} + \frac{\partial \phi_i}{\partial z} \frac{\partial z}{\partial \eta} \qquad (5.101)$$

$$\frac{\partial \phi_i}{\partial \zeta} = \frac{\partial \phi_i}{\partial x} \frac{\partial x}{\partial \zeta} + \frac{\partial \phi_i}{\partial y} \frac{\partial y}{\partial \zeta} + \frac{\partial \phi_i}{\partial z} \frac{\partial z}{\partial \zeta}$$

which can be written in matrix form as

$$\begin{bmatrix} \dfrac{\partial \phi_i}{\partial \xi} \\[2mm] \dfrac{\partial \phi_i}{\partial \eta} \\[2mm] \dfrac{\partial \phi_i}{\partial \zeta} \end{bmatrix} = \begin{bmatrix} \dfrac{\partial x}{\partial \xi} & \dfrac{\partial y}{\partial \xi} & \dfrac{\partial z}{\partial \xi} \\[2mm] \dfrac{\partial x}{\partial \eta} & \dfrac{\partial y}{\partial \eta} & \dfrac{\partial z}{\partial \eta} \\[2mm] \dfrac{\partial x}{\partial \zeta} & \dfrac{\partial y}{\partial \zeta} & \dfrac{\partial z}{\partial \zeta} \end{bmatrix} \begin{bmatrix} \dfrac{\partial \phi_i}{\partial x} \\[2mm] \dfrac{\partial \phi_i}{\partial y} \\[2mm] \dfrac{\partial \phi_i}{\partial z} \end{bmatrix} = \mathbf{J} \begin{bmatrix} \dfrac{\partial \phi_i}{\partial x} \\[2mm] \dfrac{\partial \phi_i}{\partial y} \\[2mm] \dfrac{\partial \phi_i}{\partial z} \end{bmatrix} \qquad (5.102)$$

Inverting the Jacobian matrix, $\mathbf{J}$, we can solve for the desired terms

$$\begin{bmatrix} \dfrac{\partial \phi_i}{\partial x} \\[2mm] \dfrac{\partial \phi_i}{\partial y} \\[2mm] \dfrac{\partial \phi_i}{\partial z} \end{bmatrix} = \mathbf{J}^{-1} \begin{bmatrix} \dfrac{\partial \phi_i}{\partial \xi} \\[2mm] \dfrac{\partial \phi_i}{\partial \eta} \\[2mm] \dfrac{\partial \phi_i}{\partial \zeta} \end{bmatrix} \qquad (5.103)$$

Volume integration

Volume integration is carried out with Gaussian quadrature. If g is some function defined over the volume, and n is the number of integration points in one direction, then

$$\int_v g dv = \int_{-1}^{1}\int_{-1}^{1}\int_{-1}^{1} g \left| J \right| d\xi d\eta d\zeta \tag{5.104}$$

is approximated by

$$\sum_{j=1}^{n}\sum_{k=1}^{n}\sum_{l=1}^{n} g_{jkl} \left| J_{jkl} \right| w_j w_k w_l \tag{5.105}$$

where w_j, w_k, w_l are the weighting factors,

$$g_{jkl} = g\left(\xi_j, \eta_k, \zeta_l\right) \tag{5.106}$$

5.4.3 Update of the Jaumann stress rate

Stresses for a material which exhibits elasto-plastic behaviour are integrated incrementally in time (Hallquist, 2006c):

$$\sigma_{ij}\left(t + dt\right) = \sigma_{ij}\left(t\right) + \dot{\sigma}_{ij} dt \tag{5.107}$$

In equation (5.107) the dot denotes the material time derivative given by

$$\dot{\sigma}_{ij} = \overset{\nabla}{\sigma}_{ij} - \sigma_{ik} w_{kj} - \sigma_{jk} w_{ki} \tag{5.108}$$

in which

$$w_{ij} = \frac{1}{2}\left(\frac{\partial \dot{x}_i}{\partial x_j} - \frac{\partial \dot{x}_j}{\partial x_i}\right) \tag{5.109}$$

is the spin tensor and

$$\overset{\nabla}{\sigma}_{ij} = C_{ijkl}\dot{\varepsilon}_{kl} \tag{5.110}$$

is the Jaumann stress rate as defined in (5.81).

In the implementation of equation (5.107) we first perform the stress rotation, equation (5.108), and then call a constitutive subroutine to add the incremental stress components $\overset{\nabla}{\sigma}_{ij}$. The procedure to get the stress σ_{ij}^{n+1} at time t_{n+1} given that we have the stress σ_{ij}^{n} at time t_n may be written as (Hallquist, 2006c)

$$\sigma_{ij}^{n+1} = \sigma_{ij}^{n} + r_{ij}^{n} + \overset{\nabla}{\sigma}_{ij}^{\,n+\frac{1}{2}} \Delta t^{n+\frac{1}{2}} \tag{5.111}$$

where

$$\overset{\nabla}{\sigma}_{ij}^{\,n+\frac{1}{2}} \Delta t^{n+\frac{1}{2}} = C_{ijkl}\Delta\varepsilon_{kl}^{n+\frac{1}{2}}$$

$$\Delta\varepsilon_{kl}^{n+\frac{1}{2}} = \dot{\varepsilon}_{kl}^{n+\frac{1}{2}}\Delta t^{n+\frac{1}{2}} \tag{5.112}$$

and r_{ij}^n gives the rotation of the stress at time t^n to the configuration at t^{n+1}

$$r_{ij}^n = \left(\sigma_{ip}^n w_{pj}^{n+\frac{1}{2}} + \sigma_{jp}^n w_{pi}^{n+\frac{1}{2}}\right)\Delta t^{n+\frac{1}{2}} \tag{5.113}$$

5.4.4 Time step control and time integration procedure

During the calculations, the LS-DYNA explicit solver loops through the elements to update the stress and the right hand side force vector. It also estimates the magnitude of an acceptable time step element by element and if these are denoted by $\Delta t_1,...,\Delta t_{ne}$ then we define (Hallquist, 2006d)

$$\Delta t^{n+1} = a \cdot \min\left\{\Delta t_1, \Delta t_2, \Delta t_3,..., \Delta t_{ne}\right\} \tag{5.114}$$

where ne is the number of elements. For stability reasons the scale factor a is typically set to a value of 0.9 or some smaller value.

As explained in the LS-DYNA manual, for solid elements a critical time step size Δt_e is computed from

$$\Delta t_e = \frac{L_e}{\left\{\left[Q + \left(Q^2 + c^2\right)^{1/2}\right]\right\}} \tag{5.115}$$

where L_e is a characteristic length, which for 8-node solid elements is given by

$$L_e = \frac{v_e}{A_{e\max}} \tag{5.116}$$

v_e is element volume, $A_{e\max}$ is the area of the largest side. Q is a function of the bulk viscosity coefficients C_0 and C_1:

$$Q = \begin{cases} C_1 c + C_0 L_e \left|\dot{\varepsilon}_{kk}\right| & \text{for } \dot{\varepsilon}_{kk} < 0 \\ 0 & \text{for } \dot{\varepsilon}_{kk} \geq 0 \end{cases} \tag{5.117}$$

Description of the bulk viscosity and its use in LS-DYNA can be found in (Hallquist, 2006e). By default C_0 and C_1 have the values of 1.5 and 0.06, respectively. c in equation (5.115) and (5.117) is the adiabatic sound speed, which for materials with constant bulk modulus is given by

$$c = \sqrt{\frac{E(1-\nu)}{(1+\nu)(1-2\nu)\rho}} \tag{5.118}$$

where E is Young's modulus and ν is Poisson's ratio.

LS-DYNA uses the central difference scheme to integrate the equations of motion. The semi-discrete equations of motion at time t_n are:

$$Ma^n = P^n - F^n + H^n \tag{5.119}$$

where M is the diagonal mass matrix, P^n accounts for external body and force loads, F^n is the stress divergence vector, and H^n is the hourglass resistance. To advance to time t^{n+1} we use central difference time integration (Hallquist, 2006f):

$$a^n = M^{-1}\left(P^n - F^n + H^n\right) \tag{5.120}$$

$$v^{n+\frac{1}{2}} = v^{n-\frac{1}{2}} + a^n \Delta t^n \tag{5.121}$$

$$u^{n+1} = u^n + v^{n+\frac{1}{2}} \Delta t^{n+\frac{1}{2}} \tag{5.122}$$

where

$$\Delta t^{n+\frac{1}{2}} = \frac{\left(\Delta t^n + \Delta t^{n+1}\right)}{2} \tag{5.123}$$

and v and u are the global nodal velocity and displacement vectors, respectively. We update the geometry by adding the displacement increments to the initial geometry:

$$x^{n+1} = x^0 + u^{n+1} \tag{5.124}$$

5.5 Description of the model

Thermoforming simulation with the elasto-plastic material model for Plantic® R1 was performed using ANSYS LS-DYNA software. The model was built using 8-node fully integrated solid elements: SOLID164 with Lagrangian formulation. To reduce the time of computations only quarter of the geometry was meshed and symmetric boundary condition was set on the edges. This greatly reduced the number of elements and by this the time of computations. The sheet consisted of 1200 SOLID 164 elements with 1 element through the thickness, see Figure 5.10, and the mould of 3434 SOLID 164 elements, see Figure 5.11. The element density on the circumference of the mould is 20% higher than on circumference of the sheet. Higher discretisation of the mould was found to improve contact convergence. Furthermore, due to convergence difficulties the mould had to be approximated such that the top corner was eliminated completely and the corner at the bottom hollow part was

smoothed, this is shown schematically in Figure 5.12. These modifications to the mould are thought to have little effect on accuracy of the resultant thickness distribution.
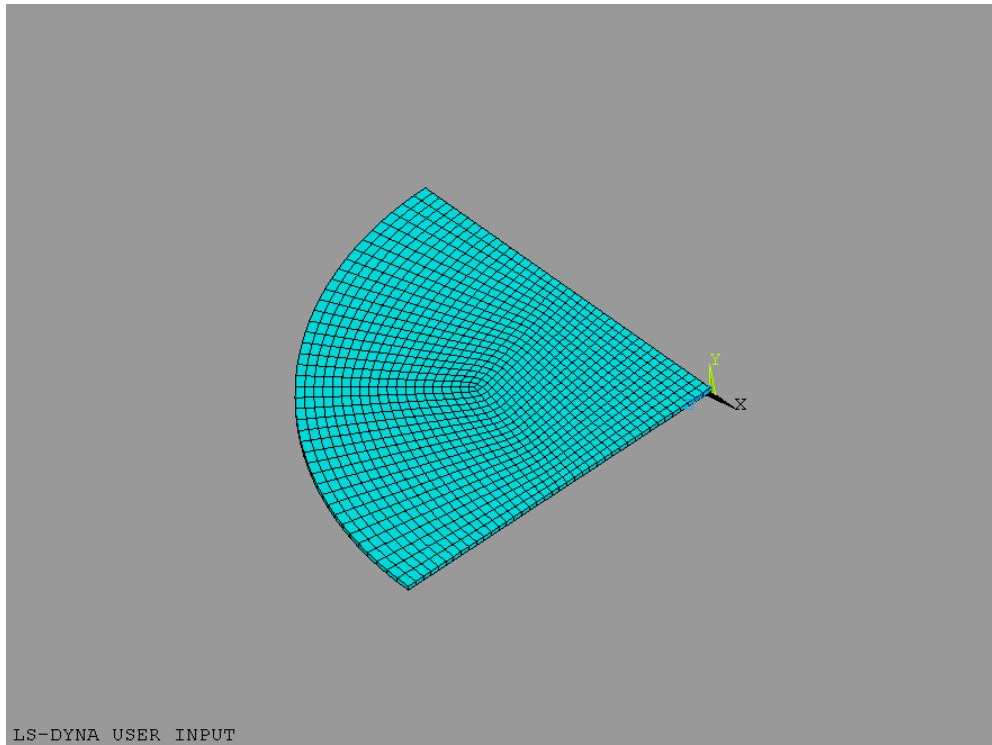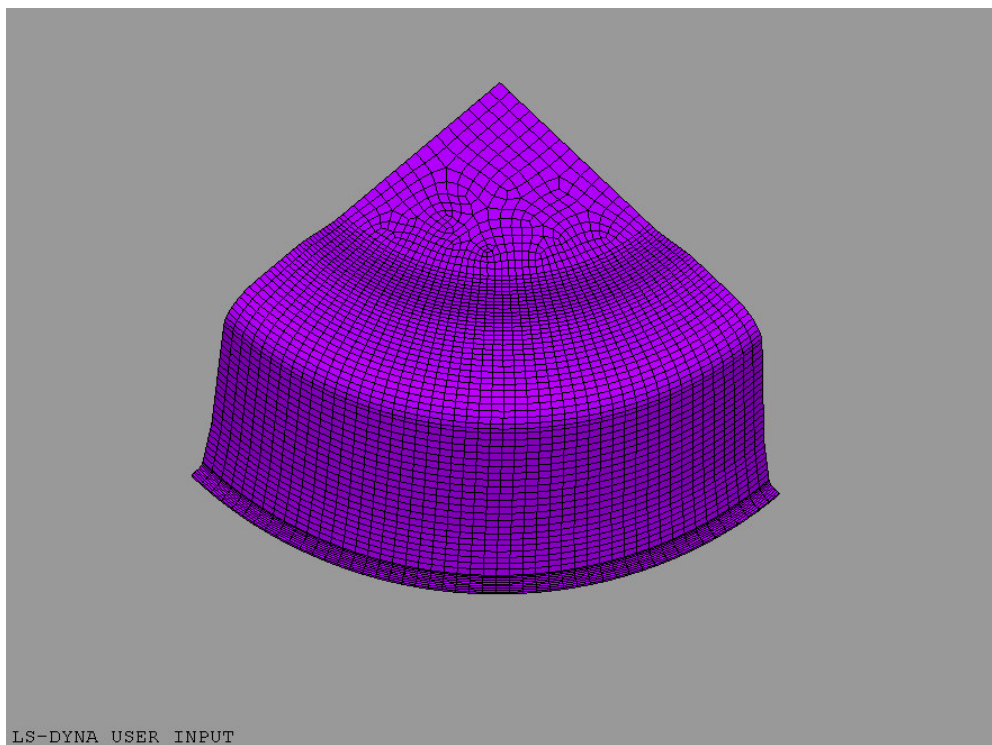

Figure 5.10. The sheet mesh.
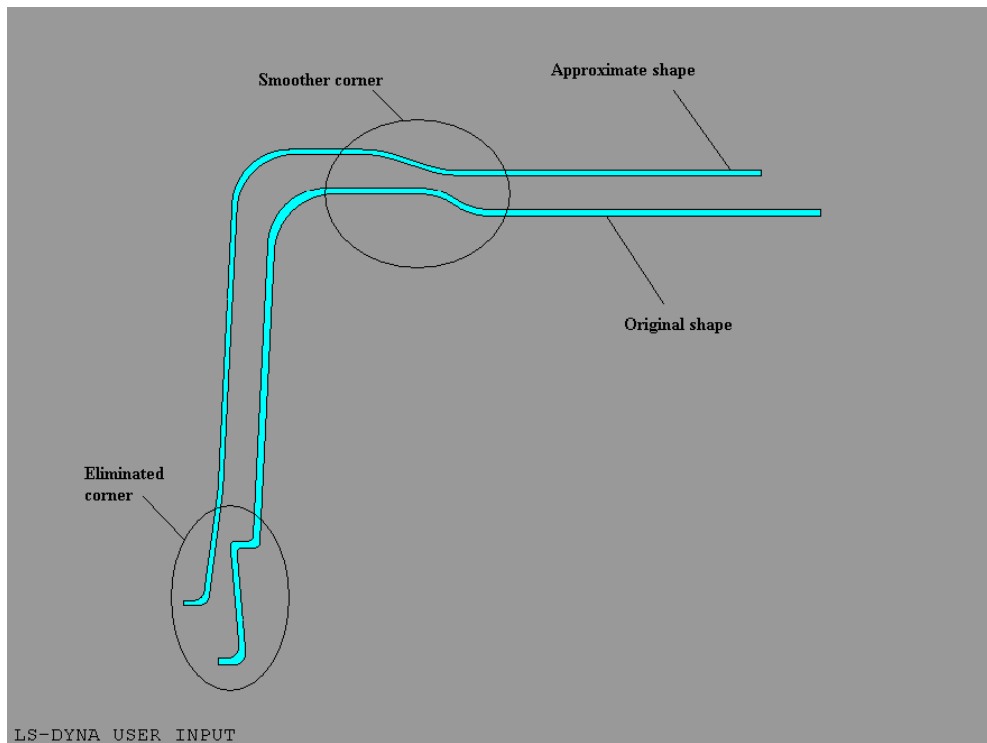

Figure 5.11. The mould mesh.

Figure 5.12. Approximation of the mould cross-section.

A bilinear elasto-plastic model with isotropic hardening was chosen for the material of the sheet. The isotropic model was chosen because any anisotropic properties of the material are omitted and the deformation considered here does not involve unloading. The parameters of the model were obtained by curve fitting to experimental data. Two simulations were considered, one where the tensile test at the highest crosshead speed, which is characterised with the lowest moisture loss, was chosen for the curve fitting. Another, where the tensile test at the lowest crosshead speed, which is characterised with the highest moisture loss, was chosen for the curve fitting. The experimental curve obtained at crosshead speed of 500 mm/min with initial moisture content of 11.91% is shown in Figure 5.13. Also on the figure is shown the bilinear elasto-plastic fit, denoted by the green dashed line.
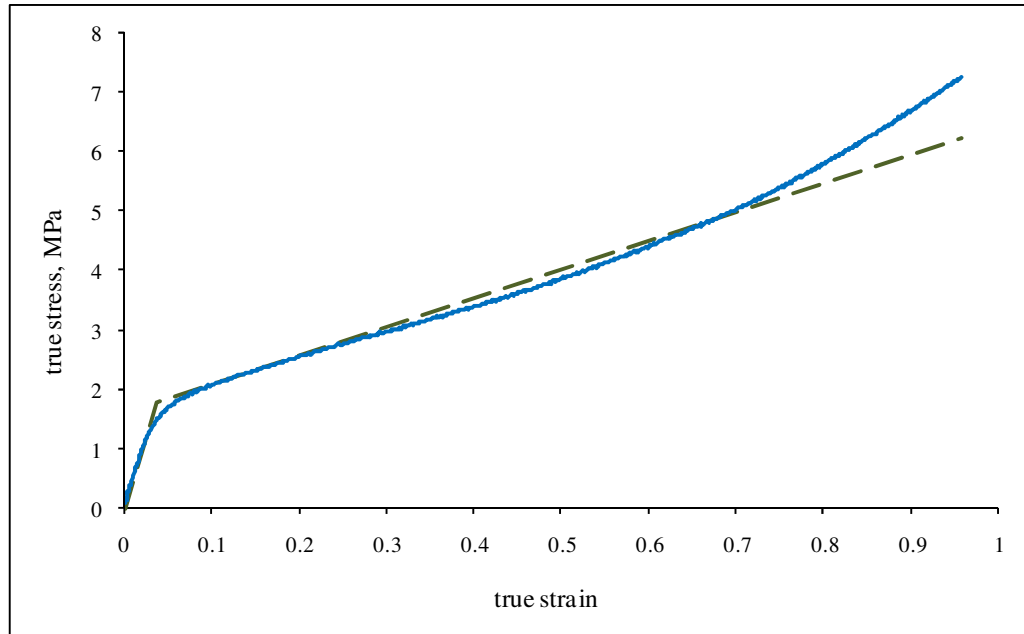
Figure 5.13. Tensile test results at crosshead speed of 500 mm/min for the Plantic® R1 material equilibrated at initial 11.91% moisture content (blue solid line) and bilinear elasto-plastic fit (dashed green line).

The material parameters for the sheet are as follows:

$$E = 4.9667 \times 10^7$$
$$\sigma_y = 1.788 \times 10^6$$
$$E_{\tan} = 4.827 \times 10^6$$
$$\nu = 0.3$$
$$\rho = 1400$$

where E is the elastic modulus, σ_y is the yield stress, $E_{\tan}$ is the tangent modulus, ν is the Poisson's ratio and ρ is the density.

The mould was modeled as a rigid body with elastic material properties. The material parameters for the mould are as follows

$$E = 1 \times 10^{10}$$
$$\nu = 0.3$$
$$\rho = 7850$$

From tensile test results, Figure 3.3 and Figure 3.5, it can be observed that the elastic modulus, tangent modulus and the yield strength increase with decrease in moisture content (or moisture loss). It can be seen also that materials with constant initial moisture content, which are being stretched at high temperature with different strain rates the initial elastic modulus and yield strength are the same but the tangent

modulus is increasing with decrease in strain rate. This is due to higher moisture loses for lower strain rates, as already discussed in previous chapters. In order to investigate the effect of moisture loss the bilinear elasto-plastic model was fitted to experimental curve obtained at lower cross-head speed of 100 mm/min, but similar initial moisture content of 11.91%. The experimental curve and the fit are shown in Figure 5.14. The elastic modulus and yield strength were retained from the previous fit. From the fitting the tangent modulus $E_{\tan} = 10.53 \times 10^6$ Pa was obtained.
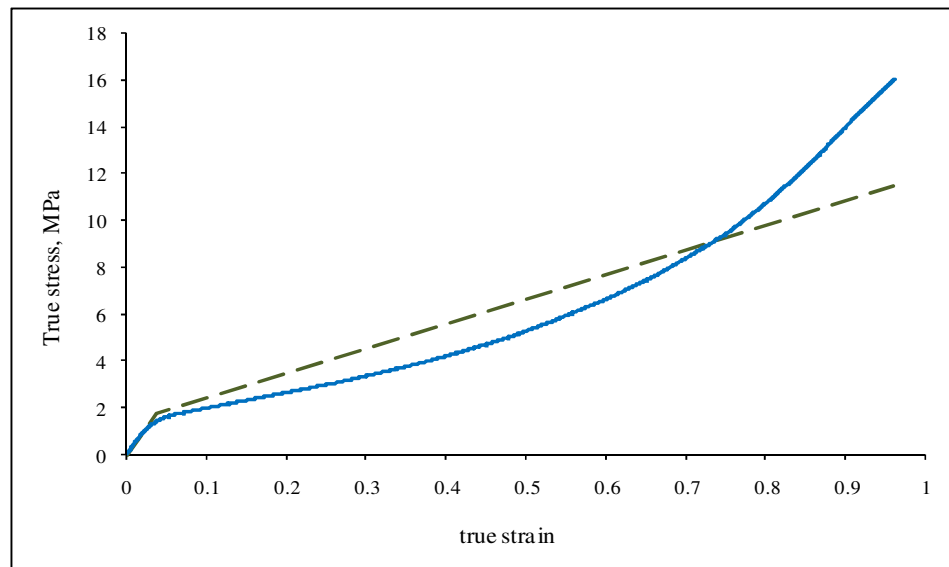

Figure 5.14. Tensile test results at crosshead speed of 100 mm/min for the Plantic$^{®}$ R1 material equilibrated at initial 11.91% moisture content (blue solid line) and bilinear elasto-plastic fit (dashed green line).

The contact option in LS-DYNA was chosen to be "General Surface To Surface" with static and dynamic friction coefficients both set to 1, 0.5 and 0.1. The actual friction coefficient is calculated from (Hallquist, 2006g)

$$\mu c = FD + (FS - FD)e^{-DC(v_{rel})} \tag{5.125}$$

where FD is dynamic friction coefficient, FS static friction coefficient, DC is the exponential decay coefficient, which is by default set to 0, and v_{rel} is the relative velocity. For FD and FS = 1 we have that $\mu c = 1$. Such a high value of friction coefficient allows simulating sticking contact, which was assumed previously. In order to investigate the effect of friction coefficient computations with contact friction coefficient of 0.5 and 0.1 were also performed.

Deformation time was assumed to be 3 sec and time increment was scaled to 1×10^{-6} sec. The pressure loading was assumed to increase linearly with time from 0 to 0.3 MPa at 3 sec.
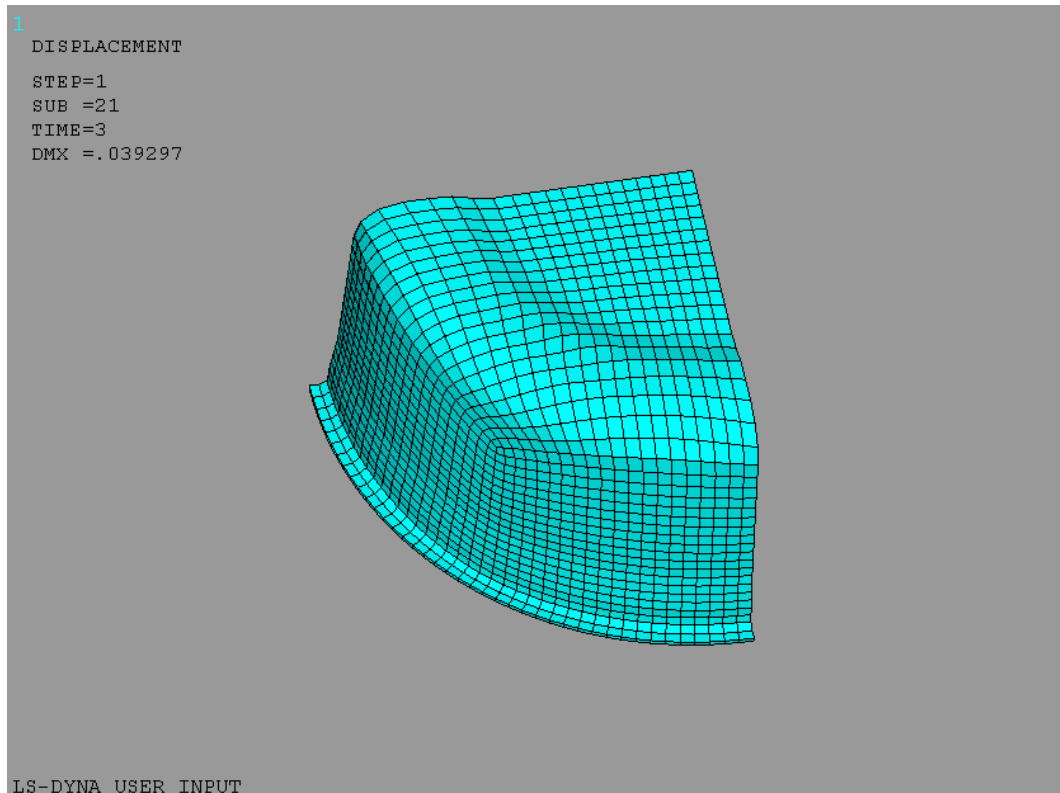
Figure 5.15. The deformed shape.

5.6 Comparison of thickness and discussion

This section presents results of computations with an elasto-plastic material model described in the previous sections. We also present a comparison of these results with experimental measurements and with computations with the hyperelastic material model from Chapter 4.

The deformed shape is shown in Figure 5.15 and the distribution of the 3rd principal strain in Figure 5.16. The data for the thickness distribution were taken along a path cutting the sheet into two equal pieces, as shown on the Figure 5.16. This particular path was chosen due to higher concentration of nodes in its vicinity, thus higher accuracy. Figure 5.17 presents thickness distribution obtained from

calculations with friction coefficient of 1. The results of computations with different values of friction coefficient are shown in Figure 5.18. We can see that lowering the values of friction coefficient results in flattening of thickness distribution, thus we have slightly lower thickness at the centre and slightly higher at the hollow corner part. But the thickness distribution for the highest friction coefficient is closer to the experimental result. This supports that the assumption of sticking contact is appropriately chosen for this application.
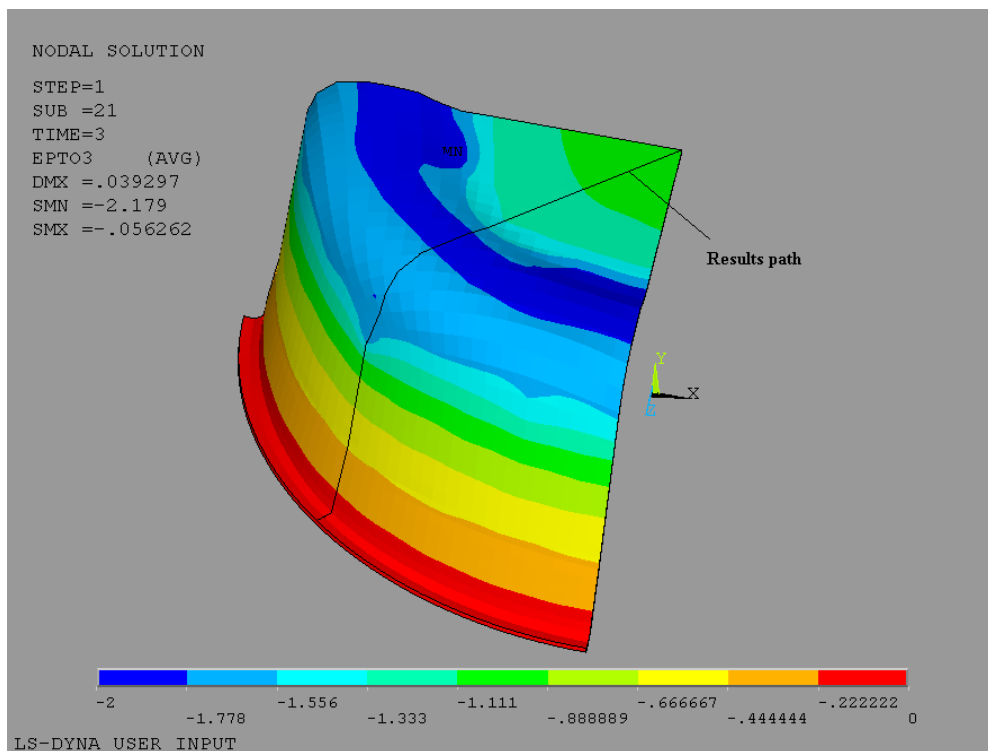
Figure 5.16. Distribution of 3rd principal strain and results path.
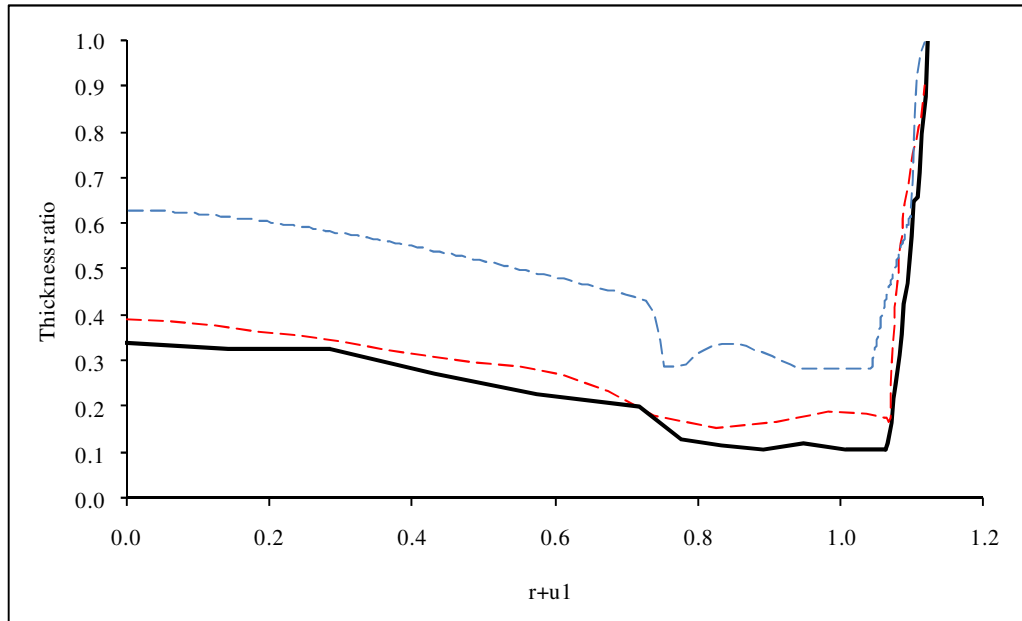
Figure 5.17. Comparison between thickness distribution for elasto-plastic (red dashed line) and hyperelastic models (blue dashed line), and experimental results (black solid line).
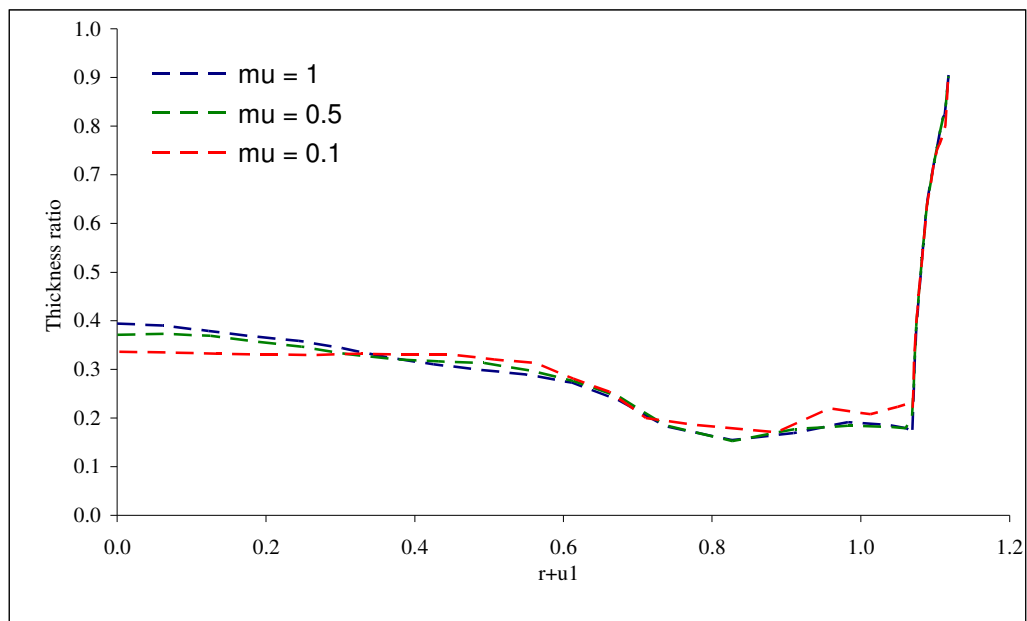
Figure 5.18. Thickness distribution for different values of friction coefficient.

The thickness distribution obtained from computations with an elasto-plastic fit for the experimental curve at a crosshead speed of 100 mm/min is shown in Figure 5.19 and is denoted by the green dashed line. The red solid line in Figure 5.19 denotes thickness distribution for computations with an elasto-plastic fit for the

highest crosshead speed of 500 mm/min. As we can see the thickness distribution is affected by the higher tangent modulus and the sheet is thicker at the bottom part and thinner on the walls. This leads to a conclusion that moisture loss affects the deformation. We also have to remember that moisture loss results in material shrinkage and this will affect the resultant shape or thickness distribution even more. We also need to bear in mind that material with different initial moisture content will produce a different stress-strain curve in tensile test, thus the elastic modulus, yield strength and tangent modulus will be different. This will affect the deformed shape and will result in a different thickness distribution.

Figure 5.19. Comparison of thickness distribution for different tangent moduli. The green dashed line denotes results for tangent modulus obtained from curve fitting to tensile test at 100 mm/min and violet solid line to 500 mm/min.
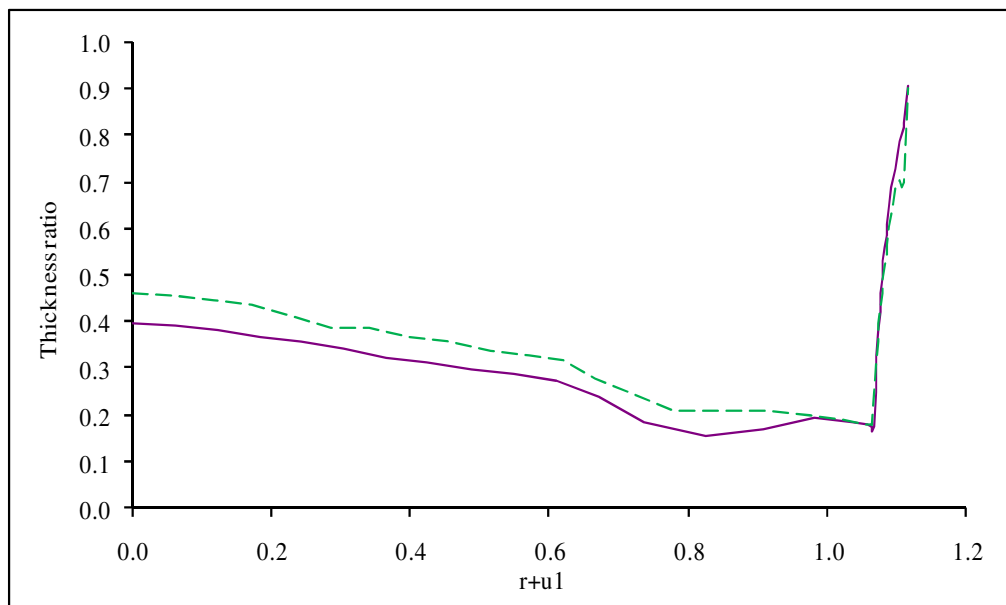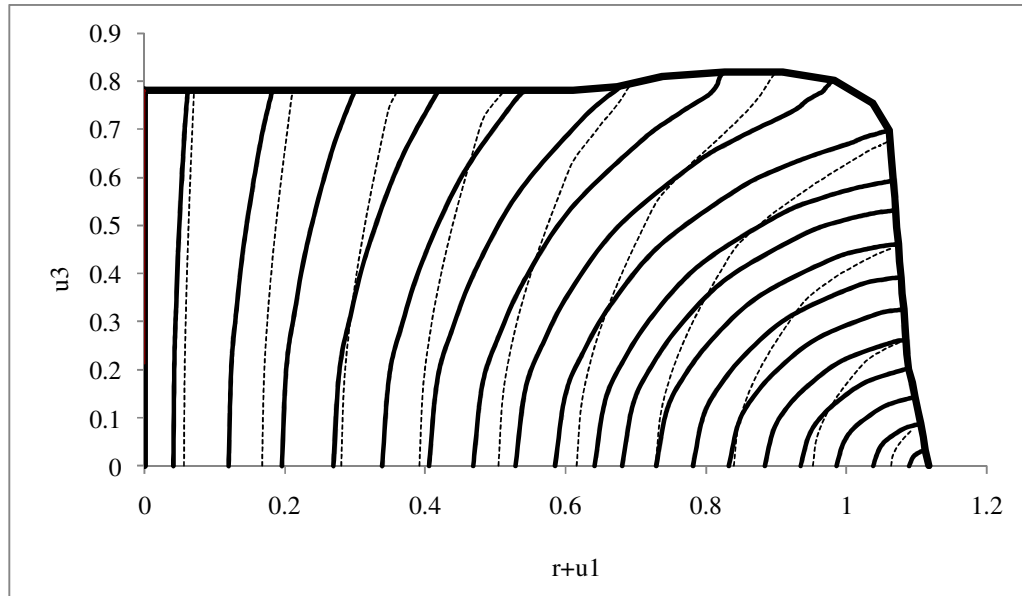
Figure 5.20. Comparison of the material particle paths for elasto-plastic (solid lines) and hyperelastic model (dashed lines).

5.7 Summary

This chapter shows results of computations with a bi-linear elasto-plastic material model with isotropic hardening, which was applied to simulate the thermoforming process of the starch-based bioplastic sheet of the Plantic® R1. The effect of moisture loss and shrinkage was not investigated here. Though, a simulation with high tangent modulus, which is related to a higher moisture loss in the material, was performed. As can be seen from Figure 5.19, the effect of higher tangent modulus is small and thus the effect of moisture loss is small. But, as already mentioned, we should bear in mind that the materials with different initial moisture content will have different initial elastic moduli, yield strengths and tangent moduli, and by this a slightly different thickness distributions may be obtained. The resultant thickness distribution was compared with experimental measurements and thickness distribution obtained from simulation with hyperelastic material model. This is shown in Figure 5.17. As we can see application of elasto-plastic material model with isotropic hardening produces much better results in comparison with the hyperelastic model. More accurate thickness distribution is achieved thanks to the application of the plastic flow rule. In the current case the sheet is starting to yield at

the centre part first, where the yield strength is exceeded and the plastic deformation occurs and this leads to a better prediction of the thickness distribution with this constitutive model compared to what is obtained with hyperelastic models described in chapter 4.

Chapter 6. Conclusions and future work

The main issues addressed in this work on experimental investigation and numerical modeling of thermoforming process of thermoplastic starch is of two folds. Firstly, materials characterisations were carried out in order to understand the material behaviour during thermoforming and the influencing factors. Secondly, constitutive equations were established in order to capture the key feature of the material behaviour and to simulate the thermoforming process in sufficient accuracy. Comparisons were made between the models and with experimental measurements.

In terms of materials behaviour investigated experimentally, the thermoplastic starch is characterised by the following features:

- Stress-strain behaviours of the material are highly dependent on the moisture content within the material in addition to the processing temperature. Loss of moisture results in significant increase in flow stress level, a drop of material ductility or elongation at break and a transition of flow behaviour from elasto-plastic to elastic mode. This feature is expected to have significant impact during each stage of thermoforming including preheating as moisture is lost by evaporation.

- Moisture loss of the material during thermoforming process leads to considerable shrinkage and change in material density. Linear shrinkage in all 3 directions (along and transverse to the extrusion direction and along the sheet thickness) was found to be similar suggesting that the effect of molecular orientation during extrusion and anisotropic shrinkage due to molecular relaxation can be neglected. This allows an isotropic material model to be used in the subsequent modeling work.

- Flow stress of the material was insensitive to strain rate in the range achievable in this work and thus viscous flow can be neglected and this further simplifies the model in the subsequent work on modeling.

In a first attempt to model thermoforming of the material, a hyperelastic membrane model was used to approximate the material as a non-linear elastic material. This simplification was chosen so that the effect of moisture loss can be incorporated by a coefficient function into the constitutive equations. Computations with this material model showed that:

- Moisture variation has a strong influence on the processing pressure required to push the sheet into the mould. The lower the moisture content left in the material the higher the pressure that is needed. Accordingly, long exposure to high preheating temperature would result in high moisture loss and a need for a higher pressure; additional pressure would be needed to push the material into the difficult-to-form corners where forming is completed last and the sheet is relatively thinner leading to higher moisture loss; cracks may also initiate from these positions as a result of loss in material ductility.

- The comparison between the predicted thickness distribution from the modeling and the experimental measurements showed that although the modeled results agree with the general trend of the measured results, there was a considerable discrepancy, particularly in the central region of the tray. The initial moisture content was found to have little effect on this discrepancy. Further computations to take account of the effect of material shrinkage due to moisture variation showed that although the shrinkage did have some effect on the thickness distribution, the discrepancy could not be markedly improved by taking account of the shrinkage alone. This led to further investigations into the improvement in the accuracy of the material model using an elasto-plastic model.

The experimental tests of the material indicated that although elastiticity may dominate at low moisture contents, it possesses elasto-plastic type of behaviour when the material is conditioned at a typical 50% relative humidity at room temperature and tested at the intended thermoforming temperature of 85 °C. Due to the complexity and limitation of time, no attempt was made to establish the moisture content function in the elasto-plastic constitutive equations. Instead, two specific

cases where moisture loss effects were incorporated implicitly in test data were studied for comparison purpose: 1) thermoforming of the material was conducted using the material parameters were obtained from tests under the above mentioned conditions and at the fastest cross-head speed so as to neglect the effect of moisture content and 2) Computations were also conducted using materials parameters obtained at a much lower cross-head speed where moisture loss cannot be neglected. The results showed that:

- Application of elasto-plastic material model produced much better agreement between the prediction of the thickness distribution and the experimental measurements without accounting for moisture loss or shrinkage. This represents processing conditions close to that in the thermoforming trials.

- Computations with parameters obtained from fitting to experimental results at a lower cross-head speed, where moisture loss was accounted for, also predicted a thickness distribution much better than the hyperelastic model and in good agreement with the measurements. In addition, it proved that the moisture loss does affect the thickness distribution which was little revealed from the hyperelastic model.

- Overall, the elasto-plastic model with isotropic hardening is a more appropriate model for the thermoplastic starch in comparison with the hyperelastic model. In the elasto-plastic model the sheet is starting to yield at the centre part first, where the yield strength is exceeded and the plastic deformation occurs, and this leads to a better prediction of the thickness distribution with the elasto-plastic model.

The work presented in this thesis gives some insight on the behaviour of the thermoplastic starch materials during thermoforming process and tensile tests. This work can be extended and improved in the future in the following aspects:

- Use of an environmental chamber enabling independent control of temperature and humidity during material testing would allow separation of influences on stress-strain behaviour from temperature and moisture content.

This would significantly improve accuracy of experimental results and enable more accurate moisture dependent constitutive equation to be established.

- Incorporation of moisture content dependent function in the elasto-plastic constitutive equation, as well as inclusion of shrinkage could enable simulation of thermoforming process of materials with different initial moisture content providing more accurate prediction of thickness distribution.

- Change in material ductility and breaking stress with loss of moisture content could be established experimentally and built into failure criteria so as to predict local failure of the sheet or predict local embrittlement – a common problem observed in thermoforming of thermoplastic starch.

Bibliography

AKIN, J.E., 1994. Finite Elements for Analysis and Design. London: Academic Press.

ARVANITOYANNIS, I. and BILIADERIS, C., 1998. Physical properties of polyol-plasticized edible films made from sodium caseinate and soluble starch blends. *Food Chemistry,* **62**(3), pp. 333-342.

ATKIN, R.J. and FOX, N., 1980a. An introduction to the theory of Elasticity. London: Longman.

ATKIN, R.J. and FOX, N., 1980b. Principles of linear and angular momentum. The stress tensor. *An introduction to the theory of Elasticity.* London: Longman, pp. 41.

AV´EROUS, L., FRINGANT, C. and MORO, L., 2001. Starch-based biodegradable materials suitable for thermoforming packaging. *Starch-Starke,* **53**(8), pp. 368-371.

BATHE, K.J., 1996. Finite element procedures. second edition edn. Englewood Cliffs, N.J.: Prentice Hall.

BAUMBERGER, S., LAPIERRE, C., MONTIES, B., LOURDIN, D. and COLONNA, P., 1997. Preparation and properties of thermally moulded and cast lignosulfonates starch blends. *Industrial Crops and Products,* **6**(3), pp. 253-258.

CAROTENUTO, A. and DELL'LSOLA, M., 1996. An Experimental Verification of Saturated Salt Solution-Based Humidity Fixed Points. *lnternational Journal of Thermophysics,* **17**(6), pp. 1423-1439.

CHANG, Y.P., CHEAH, P.B. and SEOW, C.C., 2000. Plasticizing-Antiplasticizing Effects of Water on Physical Properties of Tapioca Starch Film in the Glassy State. *Journal of food science,* **65**(3), pp. 445.

CHINACHOTI, P. and VODOVOTZ, Y., 2000. Glass Transition Behavior. *Bread Staling.* New York: CRC Press, pp. 66.

CHIOU, B., YEE, E., GLENN, G.M. and ORTS, W.J., 2005. Rheology of starch–clay nanocomposites. *Carbohydrate Polymers,* **59**(4), pp. 467.

CRANK, J., 1975a. The Diffusion Equations. *The Mathematics of Diffusion.* Second edn. Oxford: Oxford University Press, pp. 4.

CRANK, J., 1975b. Diffusion In a Plane Sheet. *The Mathematics of Diffusion.* Second edn. Oxford: Oxford University Press, pp. 48.

DAVIES, G.B.H., 2006. *Environmental Packaging*, PhD thesis, Brunel University.

DELORENZI, H.G. and NIED, H.F., 1999. Finite element simulation of thermoforming and blow moulding. *Modeling of Polymer Processing,* , pp. 117-171.

DELORENZI, H.G. and NIED, H.F., 1987. Blow moulding and thermoforming of plastics; finite element modeling. *Computers and Structures,* **26**, pp. 197-206.

DELORENZI, H.G., NIED, H.F. and TAYLOR, C.A., 1991. A numerical/experimental approach to software development for thermoforming simulations. *Journal of pressure vessel technology,* **113**(1), pp. 102-114.

DROZDOV, A.D., 1996. Finite Elasticity and Viscoelasticity. Singapore; London: World Scientific.

DUNNE, F. and PETRINIC, N., 2005a. Introduction to computational plasticity. Oxford University Press.

DUNNE, F. and PETRINIC, N., 2005b. Strain decomposition. *Introduction to computational plasticity.* Oxford; New York: Oxford University Press, pp. 11.

DUNNE, F. and PETRINIC, N., 2005c. Yield criterion. *Introduction to computational plasticity.* Oxford; New York: Oxford University Press, pp. 17.

DUNNE, F. and PETRINIC, N., 2005d. Isotropic hardening. *Introduction to computational plasticity.* Oxford; New York: Oxford University Press, pp. 23-24.

DUNNE, F. and PETRINIC, N., 2005e. Linear isotropic hardening. *Introduction to computational plasticity.* Oxford; New York: Oxford University Press, pp. 25.

DUNNE, F. and PETRINIC, N., 2005f. Elasto-plastic coupling. *Introduction to computational plasticity.* Oxford; New York: Oxford University Press, pp. 66-69.

DUNNE, F. and PETRINIC, N., 2005g. Objective stress rates. *Introduction to computational plasticity.* Oxford; New York: Oxford University Press, pp. 69-82.

GALLIARD, T., 1987. Morphology and Composition of Starch. *Starch: Properties and Potential.* Chichester: John Wiley & Sons Inc.

GREEN, A.E. and ADKINS, J.E., eds, 1970. *Large elastic deformations.* 2 edn. Oxford: Clarendon Press.

HALLQUIST, J.O., 2006a. LS-DYNA Theory Manual. Livermore: Livermore Software Technology Corporation.

HALLQUIST, J.O., 2006b. Solid Elements. *LS-DYNA Theory Manual.* Livermore: Livermore Software Technology Corporation, pp. 37-39.

HALLQUIST, J.O., 2006c. Jaumann Stress Rate. *LS-DYNA Theory Manual.* Livermore: Livermore Software Technology Corporation, pp. 243-244.

HALLQUIST, J.O., 2006d. Time Step Control. *LS-DYNA Theory Manual.* Livermore: Livermore Software Technology Corporation, pp. 489-490.

HALLQUIST, J.O., 2006e. Bulk Viscosity. *LS-DYNA Theory Manual.* Livermore: Livermore Software Technology Corporation, pp. 486-489.

HALLQUIST, J.O., 2006f. The Central Difference Method. *LS-DYNA Theory Manual.* Livermore: Livermore Software Technology Corporation, pp. 501-502.

HALLQUIST, J.O., 2006g. Friction. *LS-DYNA Theory Manual.* Livermore: Livermore Software Technology Corporation, pp. 541-542.

HILL, R., 1998. The Mathematical Theory of Plasticity. Oxford: Oxford University Press.

JIANG, W.G., WARBY, M.K., WHITEMAN, J.R., ABBOTT, S., SHORTER, W., WARWICK, P., WRIGHT, T., MUNRO, A. and MUNRO, B., 2003. Finite element modelling of high air pressure forming processes for polymer sheets. *Computational Mechanics,* **31**(1-2), pp. 163-172.

KARAMANOU, M., 2004. *A Study of Finite Element Modelling of Large Viscoelastic Deformation*, PhD Thesis, Department of Mathematical Sciences, Brunel University.

KARAMANOU, M., SHAW, S., WARBY, M.K. and WHITEMAN, J.R., 2005. Model, algorithms and error estimation for computational viscoelasticity. *Computer Methods in Applied Mechanics and Engineering,* **194**(2), pp. 245-265.

KHAN, A.S. and HUANG, S., 1995a. Continuum theory of plasticity. New York; Chichester: Wiley-IEEE.

KHAN, A.S. and HUANG, S., 1995b. Kinematics of Finite Plastic Deformation. *Continuum theory of plasticity.* New York; Chichester: Wiley-IEEE, pp. 245-250.

KLINGBEIL, M., 2002. *Global Packaging Market. Technical report.* Brussels: European Commission.

LEE, E., 1969. Elastic-plastic deformation at finite strains. *Journal of Applied Mechanics,* **36**(1), pp. 1-6.

MATZINOS, P., TSERKI, V., KONTOYIANNIS, A. and PANAYIOTOU, C., 2002. Processing and characterisation of starch/polycaprolactone products. *Polymer Degradation and Stability,* **77**(1), pp. 17-24.

NIED, H.F., TAYLOR, C.A. and DELORENZI, H.G., 1990. Three dimensional finite element simulation of thermoforming. *Polymer Engineering and Science,* **30**(20), pp. 1314-1322.

NOLAN-ITU, 2002. *Biodegradable Plastics - Developments and Environmental Impacts.* Melbourne: Environment Australia.

NORTHWOOD, T. and OAKLEY-HILL, D., 1999. *Wastebook. Technical report.* Luton Friends of the Earth, Environment Agency and the Building Research Establishment.

OGDEN, R.W., 1997a. Non-linear Elastic Deformations. Mineola, New York: Courier Dover Publications.

OGDEN, R.W., 1997b. The deformation gradient. *Non-linear Elastic Deformations.* Mineola, New York: Courier Dover Publications, pp. 83-87.

OWEN, D.R.J. and HINTON, E., 1980a. Finite Elements in Plasticity. Swansea: Pineridge Press Limited.

OWEN, D.R.J. and HINTON, E., 1980b. Elasto-plastic problems in one dimension. *Finite Elements in Plasticity.* Swansea: Pineridge Press Limited, pp. 27.

PARK, H.M., LEE, W.K., PARK, C.Y., CHO, W.J. and HA, C.S., 2003. Environmentally friendly polymer hybrids Part I *Mechanical, thermal, and barrier properties of thermoplastic starch/clay nanocomposites. Journal of Materials Science,* **38**(5), pp. 909.

PARKER, R. and RING, G.S., 1995. Diffusion in maltose-water mixtures at temperatures close to the glass transition. *Carbohydrate Research,* **273**(2), pp. 147-155.

PARKER, R. and RING, S.G., 2001. Aspects of the Physical Chemistry of Starch. *Journal of Cereal Science,* **34**(1), pp. 1.

PETERSEN, K., NIELSEN, P. and OLSEN, M.B., 2001. Physical and mechanical properties of bio-based materials – starch polylactate and polyhydroxybutyrate. *Starch-Starke,* **53**(8), pp. 356-361.

RATTO, J., STENHOUSE, P., AUERBACH, M., MITCHELL, J. and FARRELL, E., 1999. Processing, performance and biodegradability of a thermoplastic aliphatic polyester/starch system. *Polymer,* **40**(24), pp. 6777-6788.

REDDY, J.N., 1984. An introduction to the finite element method. New York; London: McGraw-Hill Book Company.

RUSSO, M.A.L., STROUNINA, K., WARET, M., NICHOLSON, T., TRUSS, R. and HALLEY, P.J., 2007. A study of water diffusion into a high-amylose starch blend: the effect of moisture content and temperature. *Biomacromolecules,* **8**(1), pp. 296-301.

SALA, G., DI LANDRO, L. and CASSAGO, D., 2002. A numerical and experimental approach to optimise sheet stamping technologies: polymers thermoforming. *Materials and Design,* **23**(1), pp. 21-39.

SCHANZER, C., FREI, W., YOUSFI, M. and BEST, J., 2005. SUKANO News. *SUKANO NewsLetter.*

SCHENKEL, G. and GLYDE, B.S., 1966a. General features of single- and twin-screw extruders. *Plastics extrusion technology and theory: The design and operation of screw extruders for plastics.* Second edn. London: Iliffe, pp. 53-55.

SCHENKEL, G. and GLYDE, B.S., 1966b. The feeding zone. *Plastics extrusion technology and theory: The design and operation of screw extruders for plastics.* Second edn. London: Iliffe, pp. 83.

SCHENKEL, G. and GLYDE, B.S., 1966c. The single screw extruder in theory and practice. *Plastics extrusion technology and theory: The design and operation of screw extruders for plastics.* Second edn. London: Iliffe, pp. 68.

SCHENKEL, G. and GLYDE, B.S., 1966d. Sheet extrusion equipment. *Plastics extrusion technology and theory: The design and operation of screw extruders for plastics.* Second edn. London: Iliffe, pp. 364-376.

SEIDENSTUCKER, T. and FRITZ, H., 1998. Innovative biodegradable materials based upon starch and thermoplastic poly(ester-urethane) (tpu). *Polymer Degradation and Stability,* **59**(1), pp. 279-285.

SPENCER, A.J.M., 1980a. Continuum Mechanics. London: Longman Mathematical Texts.

SPENCER, A.J.M., 1980b. Equations of equilibrium. *Continuum Mechanics.* London: Longman Mathematical Texts, pp. 51-52.

STEVENS, E.S., 2003. Environmentally Degradable Plastics. *Encyclopedia Of Polymer Science and Technology,* **6**, pp. 135-158.

STRANG, G. and FIX, G.J., 1973. An Analysis of the Finite Element Method. New Jersey: Prentice-Hall.

SUZALEC, A., 2004. The Plastic Flow Rule. *Theory of Metal Forming Plasticity.* Berlin: Springer, pp. 69-73.

TAYLOR, C.A., DELORENZI, H.G. and KAZMER, D.O., 1992. Experimental and numerical investigations of the vacuum-forming process. *Polymer Engineering and Science,* **32**(16), pp. 1163-1173.

THRONE, J.L., 1996. Thermoforming - Definitions, History, Methods and Equipment. *Technology of Thermoforming.* Munich; Cincinnati: Hanser/Gardner Publications, Inc., pp. 1-52.

TROMP, R.H., PARKER, R. and RING, G.S., 1997. Water diffusion in glasses of carbohydrates. *Carbohydrate Research,* **303**(2), pp. 199-205.

WARBY, M.K. and WHITEMAN, J.R., 1988. Finite element model of viscoelastic membrane deformation. *Computer Methods in Applied Mechanics and Engineering,* **68**(1), pp. 33-54.

WARBY, M.K., WHITEMAN, J.R., JIANG, W.G., WARWICK, P. and WRIGHT, T., 2003. Finite element simulation of thermoforming processes for polymer sheets. *Mathematics and Computers in Simulation,* **61**(3), pp. 209-218.

WIDDECKE, H., OTTEN, A., MAREK, A. and APELT, S., 2007/2008. Bioplastics. Processing parameters and technical characterestics. A global review. CTC Clean Tech Consulting GmbH & Fachhochschule Braunschweig/Wolfenbuttel.

Web references

WEB1, http://www.lotfi.net/recycle/plastic.

WEB2, http://www.biopolymer.net.

WEB3, http://www.greenlightint.co.uk.

WEB4, http://www.materbi.com.

WEB5, http://www.plastiroll.fi.

WEB6, http://www.biotec.de.

WEB7, http://www.cargilldow.com.

WEB8, http://www.european-bioplastics.org.

WEB9, http://www.en.wikipedia.org/wiki/Polylactic_acid.

WEB10, http://www.plantic.co.uk.

WEB11, http://www.potatopak.org/products.html.

WEB12, http://www.psmna.com/home.html.

WEB13, http://www.bioplast.org.uk.

WEB14, http://www.pslc.ws/macrog/mpm/composit/nano/index.htm.

WEB15, http://www.natureworksllc.com.

WEB16, http://www.toyota.co.jp/en/index.html.

WEB17, http://www.hycail.com.

WEB18, http://www.lactic.com.